Synchronous Response Modelling and Control of an Annular Momentum Control Device

Richard Hockney, Bruce G. Johnson, and Kathleen Misovec

(NASA-CR-4166) SYNCHRONOUS RESPONSE
MODELLING AND CONTROL OF AN ANNULAR MOMENTUM
CONTROL DEVICE Final Report (SatCon
Technology Corp.) 146 p   CSCL 131

N88-29555

Unclas
0161751

NASA

NASA Contractor Report 4166

Synchronous Response Modelling and Control of an Annular Momentum Control Device

Richard Hockney, Bruce G. Johnson,
and Kathleen Misovec
SatCon Technology Corporation
Cambridge, Massachusetts

NASA

National Aeronautics
and Space Administration

Scientific and Technical
Information Division

1988

SYNCHRONOUS RESPONSE MODELLING AND CONTROL OF AN ANNULAR MOMENTUM CONTROL DEVICE

ABSTRACT

This report documents research into the synchronous response modelling and control of an advanced Annular Momentum Control Device (AMCD) used to control the attitude of spacecraft. Under this contract, SatCon Technology Corporation developed dynamic models of the synchronous response caused by mass unbalances and developed control algorithms that minimize the synchronous bearing forces. These synchronous forces produced by the magnetic bearing lead to undesirable vibrations.

For the flexible rotor AMCD, two sources of synchronous vibrations were identified. One source, which corresponds to the mass unbalance problem of rigid rotors suspended in conventional bearings, is caused by measurement errors of the rotor center of mass position. The other source of synchronous vibrations is misalignments between the hub and flywheel masses of the AMCD.

Four different control algorithms were examined. These were lead-lag compensators that mimic conventional bearing dynamics, tracking notch filters used in the feedback loop, tracking differential- notch filters, and model based compensators. The first two approaches, lead-lag and tracking notch filters, are the conventional approaches for magnetic bearing applications. They suffer from a number of disadvantages, however, including either poor synchronous performance or poor stability. The third approach, tracking differential-notch filters, was developed under this program. These controllers combine the best features of both the lead-lag and tracking notch filters. The fourth approach investigated the use of model based compensators, as developed under a previous NASA contract.

The tracking differential-notch filters developed under this contract were shown to have a number of advantages over more conventional approaches for both rigid-body rotor applications and flexible rotor applications such as the AMCD. Hardware implementation schemes for the tracking differential-notch filter were investigated. A simple design was developed that can be implemented with analog multipliers and low-bandwidth, digital hardware.

iii

ACKNOWLEDGMENT

PRECEDING PAGE BLANK NOT FILMED

v

PAGE ɪⱽ INTENTIONALLY BLANK

TABLE OF CONTENTS

PRECEDING PAGE BLANK NOT FILMED

LIST OF ILLUSTRATIONS

1 INTRODUCTION

This document reports research into the modelling and control of an advanced Annular Momentum Control Device (AMCD), used to control the attitude of spacecraft. These systems consist of an angular momentum storage flywheel supported in magnetic bearings. This research was performed by SatCon Technology Corporation under contract to NASA Langley Research Center (NASA contract NAS1-18322) in support of a specific AMCD concept, the AMCD Combined Control Energy Storage System (ACCESS). Under this contract, SatCon Technology Corporation was tasked to develop dynamic models of the synchronous response (mass unbalances) and develop control algorithms that minimize the synchronous bearing forces, which are forces that occur at the rotational (synchronous) speed. These synchronous forces produced by the magnetic bearing lead to undesirable synchronous vibrations.

This synchronous response research is an extension of an earlier NASA sponsored SatCon research program (NASA contract NAS9-17560) that developed stabilizing controllers for the ACCESS. The focus of this earlier research was to control the non-synchronous instabilities caused by the high rotational speeds and flexible rotor of the ACCESS.

The first chapter of this report provides background and introductory material. The next section, Section 1.1, provides background material for the combined energy storage and attitude control systems and the angular momentum control device (AMCD).

1

Section 1.2 introduces the specific system analyzed in this report, the AMCD Combined Control Energy Storage (ACCESS) System. Section 1.3 discusses the background in synchronous rotor control that is applicable to the ACCESS system. Section 1.4 then discusses the specific problems that are addressed in this research.

Chapter 2 develops a synchronous response model for the ACCESS system. This model is capable of predicting the response to mass unbalances of the rigid-body modes and mass unbalances of the flexible rotor modes. The major emphasis of this modelling effort is to develop synchronous response attributes that are unique to magnetically suspended rotors, such as the effects of rotor position measurement errors.

Chapter 3 reviews existing approaches to the active control of synchronous response and presents the new approaches and algorithms developed during this research program. The existing approaches include simple lead-lag compensation, which mimics spring-damper conventional bearings, and the inclusion of a tracking notch filter at the synchronous frequency. Advanced synchronous filter techniques, developed under this contract, are next presented. These advanced algorithms have many advantages, in particular better stability properties, compared to simple tracking notch filters. The fourth approach presented is model-based compensators (MBCs), which combine full-state-feedback, linear-quadratic regulators with state estimators. These MBCs were developed during the previous NASA sponsored research that

2

investigated stabilizing control algorithms for ACCESS.

Chapter 3 develops these control algorithms and applies them to rigid-body rotors. In Chapter 4, these control algorithms are applied to the flexible rotor of ACCESS. Chapter 5 presents a summary of the results and conclusions.

1.1 Background

The use of flywheels as attitude control actuators for orbiting spacecraft began in the early days of the space program [Roberson 1958] and has steadily progressed to a state of relative maturity [Weinberg 1982; Wertz 1978]. Reaction wheels, momentum wheels, and control moment gyros are the current approaches by which torques are applied to satellites. All of these devices effect attitude control by exchanging angular momentum between a flywheel and the spacecraft. Reaction and momentum wheels contain variable-speed flywheel rotors with a fixed orientation relative to the spacecraft. Reaction wheels are designed to spin in either direction and are nominally non-spinning. Momentum wheels spin in only one direction about a nominal bias speed. A control moment gyro (CMG) contains a constant-speed flywheel with either a single- or a two-degree-of-freedom gimbal system. Angular momentum is exchanged between a CMG and a spacecraft through the variation of the relative orientation of the flywheel [Kennel 1970; Wertz 1978].

The primary cause of torque jitter in these devices is the mechanical bearings that are unable to precisely maintain the

3

orientation of the angular momentum of the flywheel with respect to the satellite. This problem is typically solved by demanding extremely close manufacturing tolerances in the mechanical bearings [Wienberg 1982].

A magnetic bearing allows the angular momentum of a flywheel and its related dynamics to be controlled in a spacecraft environment. The earliest attempt at utilizing a magnetically suspended flywheel as an attitude control actuator was made at NASA/LaRC with the construction of an AMCD that consists of a magnetically suspended graphite/epoxy hoop designed to be used as a momentum wheel [Anderson 1975; Groom 1978]. There has also been a great deal of research performed by Sperry Flight Systems [Sabnis 1975; 1976; Stocking 1984], the European Space Agency [Robinson 1984], and the Japanese National Aerospace Laboratory [Murakami 1982] aimed at developing magnetically suspended angular momentum exchange effectors.

The first study of a combined attitude control and energy storage system using flywheels was performed by Rockwell International for NASA in 1974 [Notti 1974]. This system, called an Integrated Power and Attitude Control System (IPACS), contained high-speed ball bearings and a permanent-magnet motor/generator supporting and driving a titanium rotor. The study identified magnetic suspensions, composite rotors, and high-efficiency motor/generators as subsystems important for improved performance [Anderson 1973; Keckler 1974; Notti 1974].

These combined energy storage and attitude control systems

have been investigated at the Charles Stark Draper Laboratory (CSDL) since 1981 [Eisenhaure 1984a; 1984b], growing out of earlier work in magnetic bearings for terrestrial energy storage flywheels begun in 1975 [Eisenhaure 1977]. The first concept consisted of a pair of magnetically suspended counter-rotating flywheels mounted along the roll axis of a small satellite. This system can provide adequate control torques when the energy and angular momentum wheels are gimballed through only small angles (< 0.7 degrees) [Eisenhaure 1984a].

1.2 AMCD Combined Control Energy Storage System (ACCESS)

An advanced ACCESS effector evolved out of a study that considered the ACCESS concept for use in Space Station. This joint CSDL and Rockwell International study resulted in the design of an Attitude Control and Energy Storage System (ACESS) based on an advanced ACCESS effector [Oglevie 1985]. A unique feature of this advanced ACCESS design is the large-angle magnetic suspension (LAMS). This suspension allows limited gimballing freedom of approximately five degrees. This magnetic gimballing eliminates the need for mechanical gimbals.

A scale model of the advanced ACCESS module is being developed at CSDL to prove concept viability. This laboratory module is an approximately 1/20th scale model of an Space Station ACCESS module. The size of a full-scale module and scaling decisions can be found in O'Dea [1985]. The laboratory module shown in Figure 1 consists of a central electromechanical hub connected to the flywheel by a spoke structure. The

5
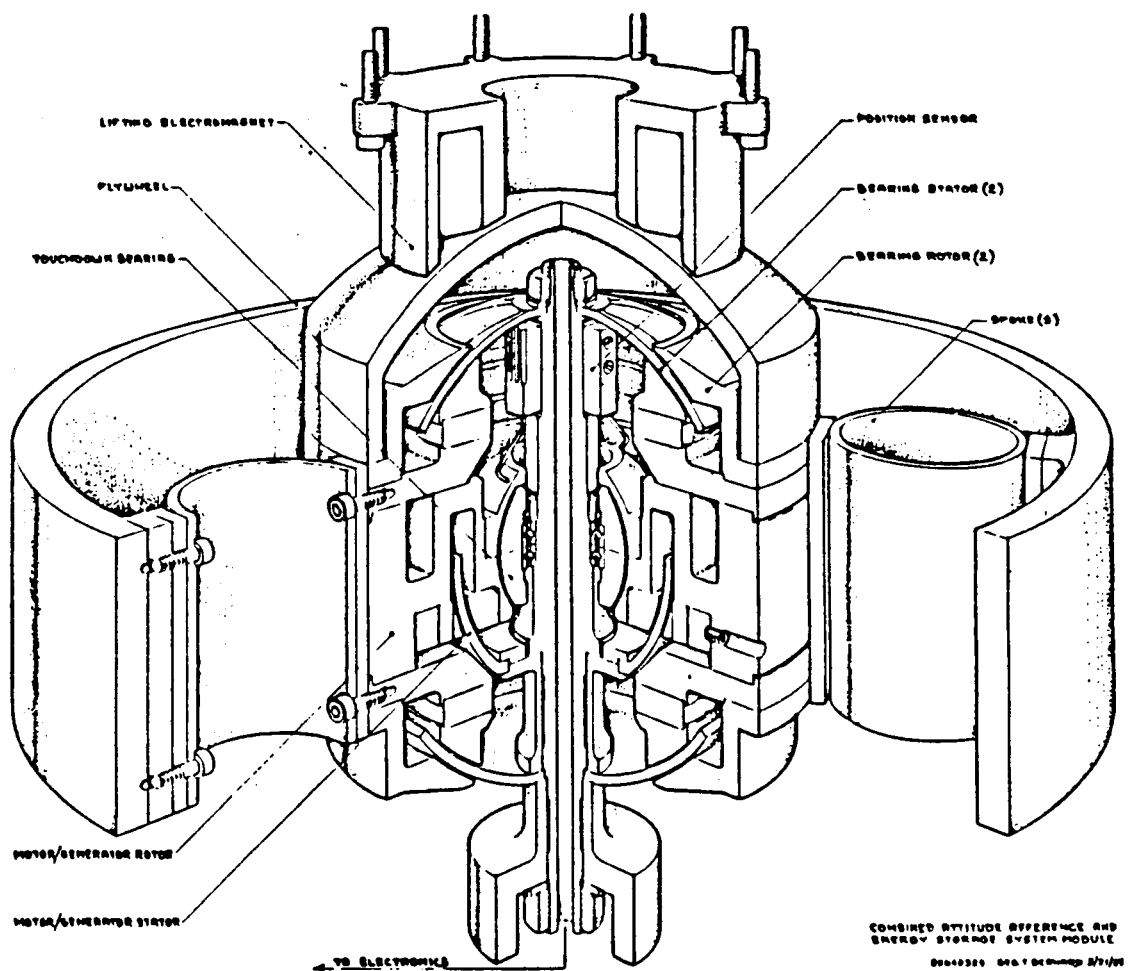
Figure 1.   Laboratory-model AMCD Combined Control Energy
             Storage System (ACCESS)

6

electromechanical hub contains the large-angle magnetic suspension, motor/generator, and sensors. The electromechanical hub also contains touchdown bearings in case of magnetic bearing failure. An auxiliary lifting electromagnet is shown at the top of the figure. This magnet is needed to unload the weight of the suspended flywheel system from the large-angle magnetic suspension, which is not designed for earth gravity environment.

The following paragraphs provide a brief description of the important ACCESS subsystems. The design size and capabilities of the laboratory module are given in Table I. The paper by O'Dea [1985] provides a more detailed overview of the system. More detailed descriptions of the subsystem designs are found in Chapter 2 of the previous NASA report [Johnson 1987b].

Table I Characteristics of the Laboratory ACCESS Module

Flywheel Mass (kg)	18
Flywheel Angular Momentum (kN-m-s)	2.2
Maximum Gimbal Angle (degrees)	± 5
Power (kW)	1
Maximum Control Torque (N-m)	5
Maximum Rotational Speed (rad/sec)	1690

The large-angle magnetic suspension chosen for the laboratory ACCESS module is a Lorentz-force, spherical air-gap bearing. The bearing uses Series 2-17 rare-earth-cobalt permanent magnets with a 22MGoe maximum energy product to produce a spherically radial magnetic field in the spherical air gap.

The spherical configuration allows limited gimballing freedom in the bearing. The eight stator coils mounted in the spherical air-gap are capable of providing translational and axial forces and radial torques by appropriate excitation of the coils. This type of Lorentz-force bearing has the advantages of linearity, high bandwidth, and negligible coupling between bearing force and motion.

The motor/generator transfers power bidirectionally between the flywheel and electrical power bus. The motor/generator must have high efficiency in both motor and generator modes. Other requirements include low side loading on the magnetic suspension and gimballing capability. A variety of machine types were investigated from which a permanent magnet, ironless stator/rotating backiron machine was chosen. This design gives high efficiency and low side loads. The machine also features a spherical air-gap to allow limited gimballing.

The ACESS study concluded that a thin-wall annular flywheel made of Boron/epoxy was the most suitable for the advanced ACCESS module. For a composite flywheel, the method of torque transfer and support between the flywheel and hub is a critical area of design. This spoke system must accommodate the high radial growth that will be seen with a composite flywheel. Because of time and cost constraints, the laboratory ACCESS flywheel is constructed of AISI 4340 steel rather than Boron/epoxy. The spoke system, however, was designed to meet the flexibility requirements imposed by a composite flywheel.

Before beginning a more detailed discussion of the synchronous modelling of the ACCESS system in Chapter 2, the next section briefly reviews previous research into active control of magnetic bearing systems, with particular emphasis on synchronous response control.

1.3 Synchronous Response Control: State-of-the-Art

Magnetic bearings are a technology still undergoing rapid development. Products that include magnetic bearings are now available, however, and some types of magnetic bearings have become relatively common. Mature magnetic bearing technology is exemplified by systems comprised of biased ferromagnetic, attractive bearings with inductive position sensors feeding single-loop designed controllers. The bearings may be permanent-magnet biased or electromagnet biased. The controllers are usually implemented with analog electronics. The rotating structure is modelled as a rigid body, and the magnetic bearings are made to behave dynamically as conventional spring/damper bearings by the use of "local" feedback.

During the last ten years a handful of researchers have begun investigating the use of magnetic bearings to support and control flexible rotors (rotors running at rotational speeds higher than their lowest frequency of free vibration). Schweitzer was the first to publish research about the active control of flexible rotors [Schweitzer 1974]. The system he investigated consisted of three rotor masses connected by well damped, flexible segments. The multi-mass rotor was supported by

conventional bearings with an actively controlled magnetic bearing added for use as an active damper. This early work used state-space methods to place closed loop system poles. Another thrust of their research was optimal placement of the sensors and active damper using generalized stabilizability and observability criteria over the modes for which active control is desired. Using the active damper, Schweitzer, et. al. were able to approximately double the range of stable operation, where the destabilizing mechanism was the rotor internal damping. They also showed improved synchronous response to mass unbalance with the active damper.

In later work they found that non-colocation of the sensors and actuator as placed by optimal stabilizability and observability criteria can lead to spillover effects, including instability [Salm 1984]. They designed reduced order controllers to provide robust, stable control when combined with collocated sensor/actuators. The design of these integrated sensor/actuator sub-systems is discussed in Ulbrich [1984]. The development of integrated sensor/actuators has led to interest in localized control of the actuator based only on information available from the integrated (collocated) sensor. This decentralized control problem is addressed by Bleuler [1984] for rigid-body rotors. His thesis also reports the use of a scheduled gain controller with two gains schedules, one used at low speeds and the other at high speeds. These scheduled gain controllers are needed because of the variation in plant dynamics caused by the gyroscopic effects

that vary with rotational speed.

Linear-quadratic design methods were used in a study by Hubbard [1980] and McDonald [1985]. They considered a pendulously supported flywheel system where the magnetic bearing was assumed to apply both forces and torques. Their model included the effect of quill-shaft flexibility, but neglected shaft damping.

The works mentioned above used numerical techniques to design specific controllers while Johnson [1985a; 1985b] examined the range of behavior that is possible given a specific controller structure. His work analytically examined the lateral dynamics of a flexible rotor supported by active bearings. The rotor system consisted of a single mass rotor with mass unbalance mounted on a symmetrical shaft (Jeffcott rotor) with internal damping. The active bearings were assumed to be ideal actuators driven by fixed-gain or variable-gain linear controllers. Measurements of the position and velocity of the shaft-rotor at the rotor and at the shaft ends (bearings) were the controller inputs. The goal was a qualitative and quantitative understanding of the differences between rotor and bearing feedback.

An interesting flexible rotor, which utilizes the unique capabilities of magnetic bearings, is the Annular Momentum Control Device (AMCD) [Anderson 1979]. This device consists of a rotating annular rim suspended by noncontacting magnetic bearings mounted along its periphery. The magnetic bearings interact with

11

a low-loss ferrite material, embedded in the graphite-epoxy rim, producing radial and axial suspension forces. The five-degree-of-freedom control problem associated with this system was found to be challenging [Groom 1981, p.130]. The early approaches used single-input, single-output (SISO) control theory, which was found to be inadequate. Later approaches considered the system as a multi-input, multi-output flexible system and used digital control with table look-up linearization of the magnetic bearing force laws [Groom 1984, p.297; Groom 1981].

A number of authors have investigated the use of magnetic bearings in conjunction with conventional oil-film bearings to control instabilities in flexible shaft systems. The dominant instability mechanism in these cases is not shaft internal damping, but oil-film bearing instabilities. The use of magnetic bearings to add damping to a conventionally supported flexible marine power transmission shaft was investigated by Holms and co-workers [Nikolajsen 1979]. They found that increased stable operating speeds were possible with the use of the active dampers and that synchronous vibration was also reduced. They included magnetic flux feedback to reduce the destabilizing force-gap interaction of their actuators. In related work, they determined the optimum force versus frequency of an actuator used to stabilize these oil-film supported shafts [Kaya 1984].

Eigenstructure assignment was used in a study by Stanway [1984] and O'Reilly. They considered a system consisting of a

flexible multi-mass rotor supported in conventional, flexibly mounted, oil-film bearings. The housings of the oil-film bearings were assumed to be controlled by active forces, supplied in addition to the forces generated by the flexible mounting structure. Damping in the rotor shaft and bearing support structure was neglected. They showed that this system can be controlled through forces applied to the bearing housing and that rotor position and velocity feedback gains are small compared to bearing position and velocity feedback gains.

In summary, the last decade has seen substantial advancement of the state-of-the-art in actively controlled flexible rotors. This research field, which started during the late 1960's and early 1970's, now draws the attention of a handful of researchers. Early research viewed the magnetic bearings as a source of additional external damping applied to conventionally supported flexible rotors. The emphasis in this early work was the placement of the actuators (magnetic bearings) and sensors. Also, during this early period state space models of the flexible rotor systems that included shaft damping were developed. The development of these state space models allowed the tools of modern state-space based control techniques to be applied to controller design, which is particularly important because of the multi-input, multi-output characteristic of magnetic bearing/rotor systems. Examples of state-space based controller designs include eigenvalue and eigenstructure assignment and linear-quadratic optimal regulators.

The control of the synchronous response caused by mass unbalances, along with system stability, has been a central concern of much of this research. During this time, notch filtering of the feedback path at the synchronous frequency has been used to reduce the effect of mass unbalances. These synchronous tracking notch filters have been built and tested [Weise 1987]; however, a number of problems remain [Beatty 1988]. These include limited ranges of stable operating speeds for both rigid and flexible rotors.

1.4 Research Focus

The research reported in this document can be divided into two areas: synchronous modelling and advanced synchronous controller design. The modelling effort consists of modelling the separate subcomponents of the ACCESS system and combining these component models into a system model useful for controller design. These subcomponent models for the large angle magnetic suspension, flywheel and attachment, and motor/generator are contained in Chapter 2 of Johnson [1987b]. The synchronous system model based on these subcomponent model is presented in Chapter 3.

The emphasis in the development of the system model is to model, in a form suitable for controller analysis and design, the unique features of <u>actively controlled</u> rotor systems. The most important of these features is that the measurements of rotor position and orientation need not be colocated with actuation. Restated, the bearings (actuators) and measurement system

14

(sensors) are not necessarily interacting with the same part of the rotor. In conventionally supported rotors, in contrast, the force produced at each bearing is a function of the time history of the position of the rotor at that bearing.

The controller design emphasis is placed on developing new algorithms for synchronous response control, especially the problem of rigid body "mass unbalance". These new algorithms overcome the serious limitations of existing approaches such as notch filtering. Four classes of controllers are examined. The first is the use of lead-lag controllers, which are dynamically similar to conventional spring/damper models of bearings. The second class of controllers add tracking notch filters at the synchronous frequency. These filters eliminate the synchronous response to mass unbalance but their usefulness is severely limited by stability constraints. The third class of controllers are the tracking differential-notch filters (TDNF) developed under this contract. These compensators retain the good synchronous performance characteristics of notch filters but with greatly expanded ranges of stable operating speeds. These tracking differential-notch filters can also be used to form the basis of a simple adaptive controller. The fourth class of controllers are the model based compensators (MBC) that combine full-state feedback, linear-quadratic regulators with Kalman filter state estimators, giving "optimal" output feedback compensators. This class of controllers were extensively investigated under the previous NASA contract (NAS9-17560), which

15

examined their stability properties.

The synchronous performance of these four classes of controllers are compared for the ACCESS, treated both as a rigid-body rotor and as a flexible rotor. This report, combined with the earlier research into system stability described in Johnson [1987b], provides an analytical basis for comparing controller performance for flexible rotor systems such as ACCESS.

2. SYNCHRONOUS RESPONSE DYNAMIC MODELLING

This chapter develops a dynamic model of the ACCESS capable of predicting its synchronous response to "mass unbalances". This derivation relies on subcomponent models, such as the hub model, bearing model, and flywheel model, that are presented in Johnson [1987b]. Based on these subcomponent models, a model of the system dynamics is developed.

A general block-diagram of the system is shown in Figure 2. The rotor is controlled by forces and torques provided by the actuator, the Lorentz-force, large angle magnetic bearing modelled under the previous contract [Johnson 1987b]. The translational positions and tilt angles of the hub and flywheel
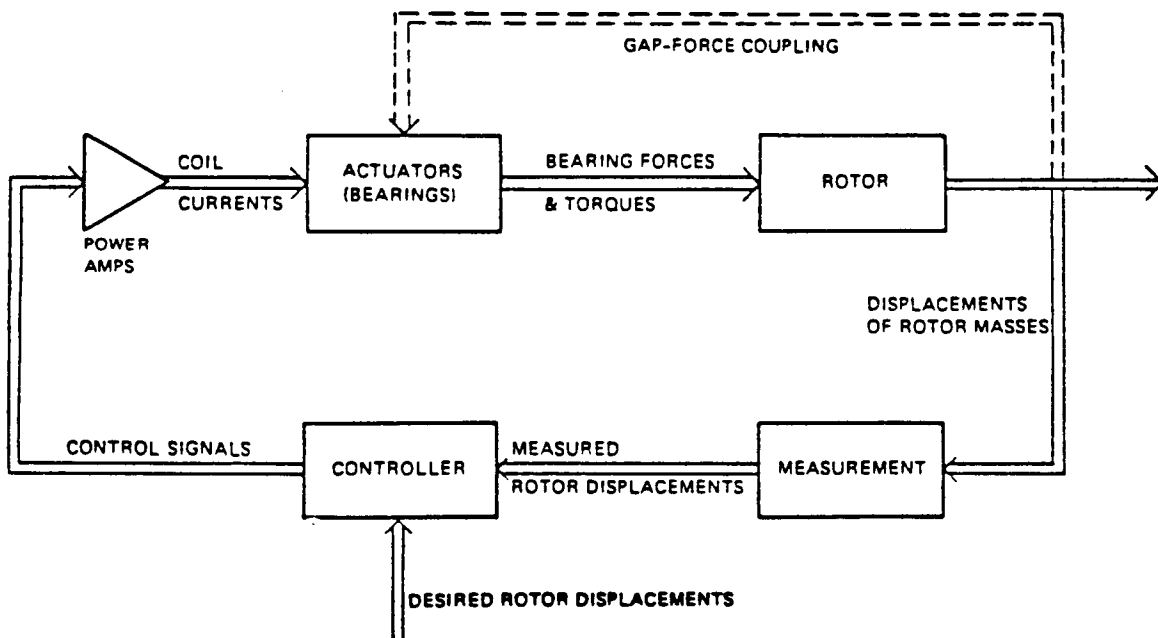
Figure 2. Block Diagram of a Magnetic Bearing System

are measured and used as inputs to the controller. The outputs
of the controller are signals controlling the power amplifiers
that drive the magnetic bearing. For conventional magnetic
bearings, the bearing forces and torques would also be a function
of the displacements of the hub as well as input currents, as
shown by the dashed lines. For the Lorentz-force bearing such as
used in ACCESS, however, there is no force-displacement coupling
to first order.

The ACCESS hardware is modelled as two rigid body masses,
the hub and the flywheel, connected by a damped, elastic
structure, the spoke system. The magnetic suspension forces and
torques act on the hub, as shown in Figure 3. Each of the
rigid-body masses in Figure 3 has three translational and three

TOROIDAL ROTOR MASSES

BEARING FORCES
AND TORQUES

FLEXIBLE
CONNECTING
STRUCTURE
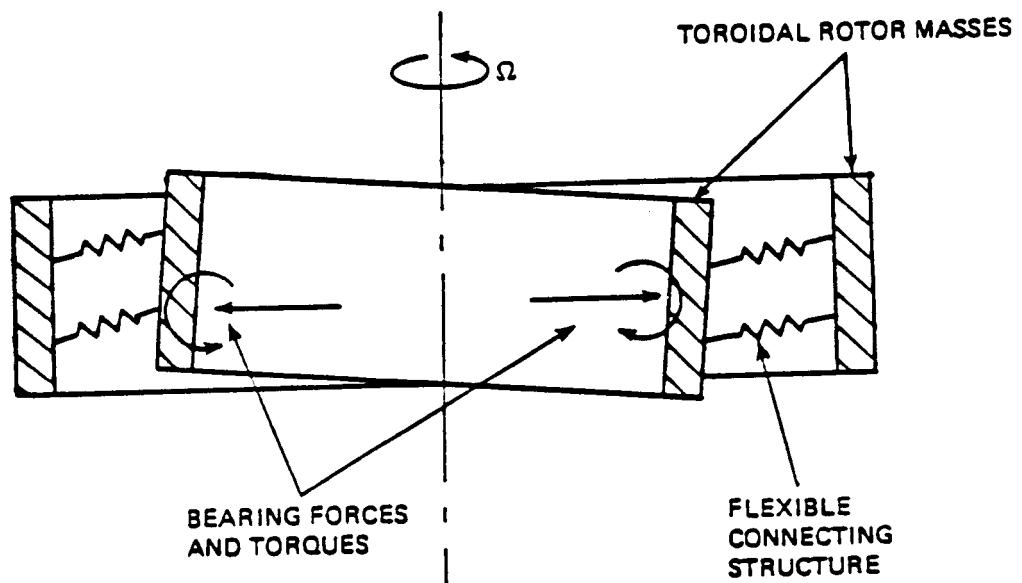
Figure 3. Cut-away of a Toroidal, Multi-body,
Flexible Rotor System

18

angular degrees of freedom. This research did not address the dynamics of two of these degrees of freedom, the translational degree of freedom along the axial direction or the angular degree of freedom associated with the spin axis. The axial, translational degree of freedom is neglected because to first order its dynamics are not a function of rotational speed and do not couple with the dynamics of the other degrees of freedom. Control of these axial dynamics is the subject of work by Downer [1980] for an all-active magnetic bearing system. Displacement control of the spin axis angular degree of freedom is not usually desired, only angular velocity control. Also, these torsional dynamics are not usually controllable by the magnetic bearing system. They may have, however, important effects on the motor controller dynamics. This problem is not addressed in this report.

The following derivation of the synchronous response model makes extensive reference to the non-synchronous model developed under NASA contract NAS9-17560 and presented in Johnson [1987b]. These derivations may also be found in a recent thesis [Johnson 1987a].

2.1 Translational Forces and Measurements

Consider first the translational forces produced by the spoke structure. The pertinent geometry is shown in Figure 4. Shown are the projections of the centers of mass and centers of force onto the radial (X,Y) inertial plane. The centers of mass, which are the origins of the principal inertial axes systems, are

Figure 4. Translational Model Geometry
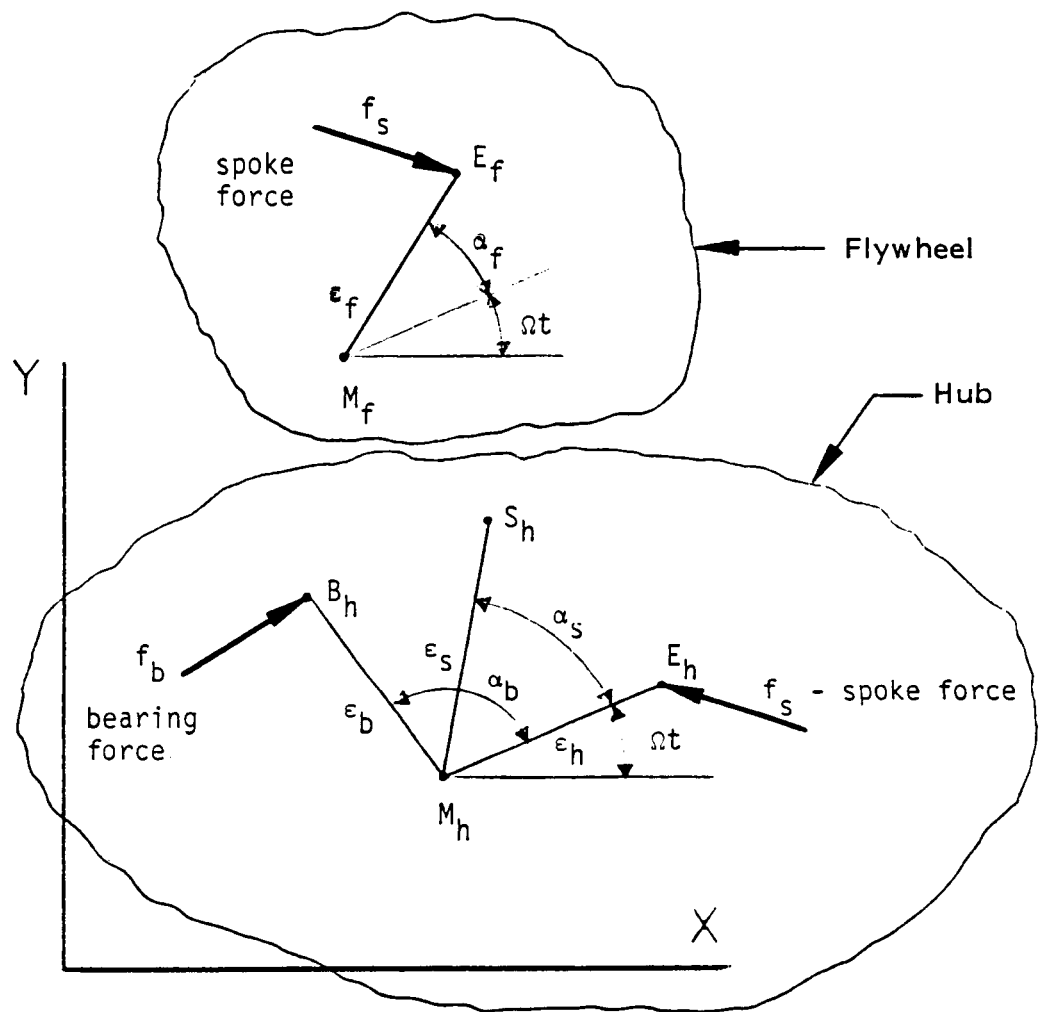
M_h – Hub center of mass

B_h – Center of bearing force

S_h – Measurement center

E_h – Hub elastic center

M_f – Flywheel center of mass

E_f – Flywheel elastic center

fixed in each rigid body and are given by M_h for the hub mass and M_f for the flywheel mass. The spoke force $\underline{f}_s$ is shown acting on the rigid body masses at position E_h on the hub and E_f on the flywheel. These centers of force are the origins of the elastic axes systems of each rigid-body mass and are fixed in each rigid body. The bearing force $\underline{f}_b$ is shown acting on the hub mass at position B_h, not generally fixed in either rotor or stator reference frames. The measurement system is assumed to measure the position of the point S_h on the hub.

The distances of the centers of force and measurement away from the centers of mass are given by ϵ_h, ϵ_b, ϵ_s, and ϵ_f. With the exception of the bearing center of force B_h, the line segments connecting these centers are fixed in the rigid bodies, and therefore spin with the rigid body. Seen from the inertial coordinate system, these line segments all have an angular velocity of Ω, to first order. Note that the time t has been chosen such that the line segment M_hE_h connecting the hub center of mass with the hub center of spoke force lies along the X-axis at time t = 0. The angles of the line segments are given by Ωt, $\alpha_s + \Omega t$, and $\alpha_f + \Omega t$. The relative angles within one rigid body mass are constants fixed by geometry, as are the distances ϵ_h, ϵ_s, and ϵ_f. The relative spin angle between the two rigid bodies is given by the angle α_f, which in general can be a function of time. When the system is experiencing steady-state rotation the angular velocity $\dot{\alpha}_f$ must be zero for the assumption of rigid body rotation at a constant speed Ω to hold. Therefore, for

21

steady-state rotation, the angle α_f must also be a constant.

The translational force produced by the spoke acts through the elastic centers E_f and E_h in the flywheel and hub respectively. The elastic force is assumed to be a linear function of the distance between these centers. The translational force generated by the spoke structure that acts on the flywheel is given as before [Johnson 1987b, Equation A.1.5] by

$$\mathbf{F_s} = -k_r \Delta \mathbf{r} - c_r \frac{d}{dt}(\Delta \mathbf{r}) + c_r \Omega \times \Delta \mathbf{r} \tag{1}$$

where now the pertinent relative displacement $\Delta \mathbf{r}$ is given by the relative displacement of the elastic centers

$$\Delta \mathbf{r} = E_f - E_h = [x_f - x_h + \epsilon_f \cos(\Omega t + \alpha_f) - \epsilon_h \cos(\Omega t)]\mathbf{i}$$
$$+ [y_f - y_h + \epsilon_f \sin(\Omega t + \alpha_f) - \epsilon_h \sin(\Omega t)]\mathbf{i}$$

and where k_r is the spoke spring constant and

$$c_r \text{ is the spoke damping} \tag{2}$$

The spoke force acting on the flywheel is then

$$\mathbf{F_s} = -[k_r(x_f - x_h) + c_r\Omega(y_f - y_h) + cr(\dot{x}_f - \dot{x}_h)]\mathbf{i}$$
$$- [k_r(y_f - y_h) + c_r\Omega(x_f - x_h) - cr(\dot{y}_f - \dot{y}_h)]\mathbf{i}$$
$$- k_r[\epsilon_f \cos(\Omega t + \alpha_f) - \epsilon_h \cos(\Omega t)]\mathbf{i}$$
$$- k_r[\epsilon_f \sin(\Omega t + \alpha_f) - \epsilon_h \sin(\Omega t)]\mathbf{i}$$

$$\tag{3}$$

22

The first two lines of Equation 3 are the same as developed for the non-synchronous model [Johnson 1987b, Equation A.1.9]. The effects of the misalignment of elastic and inertial centers ("mass unbalance") are seen in the last two lines of Equation 3. These additional forces caused by the misalignment may be considered as disturbance forces acting on the system. Note that these disturbance forces are sinusoidal functions of time with a frequency of Ω, the rotational speed of the system, called the synchronous frequency.

Using complex notation, these disturbance forces can be elegantly given as

$$F = k_r(\epsilon_f e^{(j\alpha_f)} - \epsilon_h)e^{j\Omega t} \qquad (4)$$

where the x and y direction disturbance forces are the real and imaginary parts of this equation.

The spoke force given by Equation 3 acts on the flywheel. An equal and opposite force generated by the spoke structure acts on the hub. Because these forces are equal and opposite, there is no net effect on the rigid body motion of the combined hub-flywheel system. Therefore, the misalignment between elastic and mass centers acts as a disturbance force exciting only the flexible modes of the system.

Another possible source of disturbances is the radial misalignment between the center of force of the bearing and the hub center of mass. This misalignment produces only axial torque disturbances in the system and, therefore, to first order causes

23

no disturbances in the translational dynamics.

A third source of disturbances is the measurement system. The controller is assumed to have access to measurements of hub position made by the measurement system. The position sensors nominally produce a measurement of the hub center of mass position M_h. The position sensors actually measure the distance to a machined surface, which may be imperfect, giving a corrupted measurement of hub position. An exaggerated view of this is shown in Figure 5. In general, the measurement system will produce an output that consists of the center of mass position and components at harmonics of the rotational speed Ω. For machined surfaces, the dominant error mechanism is the misalignment between the geometrical center of the machined surface being measured (S_h) and the hub center of mass (M_h).

The position of the measurement center is given by

$$S_h = x_h \underline{i} + y_h \underline{j}$$
$$= (x_h + \epsilon_s \cos(\Omega t + \alpha_s)) \underline{i} + (y_h + \epsilon_s \sin(\Omega t + \alpha_s)) \underline{j}$$

$$(5)$$

using complex notation this becomes

$$S_h = z_h = x_h + j y_h = z_h + \epsilon_s e^{j(\Omega t + \alpha_s)} \qquad (6)$$

where x_h and y_h are the x and y positions of the measurement center, which are the estimates of the hub center of mass made by the measurement system. The effect of the measurement surface misalignment, therefore, is to add a sinusoidally varying disturbance signal to the measurement of the hub center of mass

24
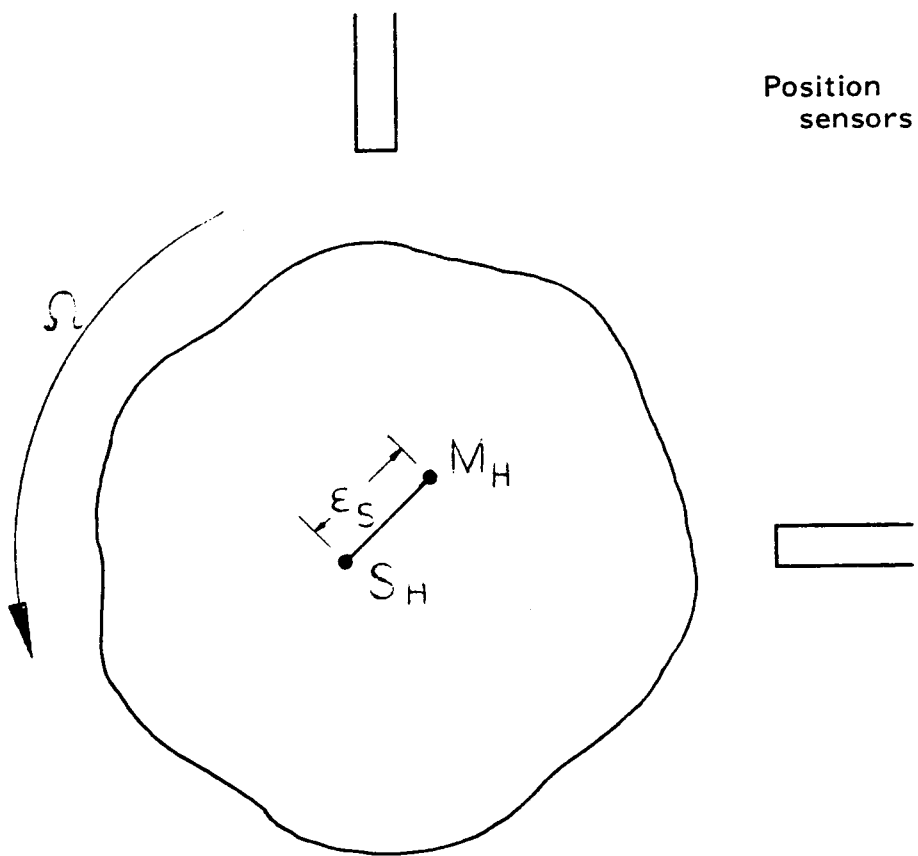
Position
sensors

M_h – Hub center of mass

S_h – Center of measurement

Figure 5. Translational Measurement Geometry

position. This corrupted measurement will be used as a feedback signal for the magnetic bearing. This misalignment will produce a disturbance that will excite both rigid body and flexible modes of the hub/flywheel system.

2.2 ACCESS Translational Model

The disturbances, plant equations, and bearing characteristics can now be combined together to produce a input/output model of the ACCESS translational dynamics. This model can be put into standard state-space form with input and output disturbances as shown in Figure 6. With the state space form shown in Figure 6, the variables and matrices are all real.

The input to the translational model shown in Figure 6 is the current vector $\underline{i}$ containing the two Lorentz bearing translational currents as

$$\underline{i} = [i_x, \ i_y]^T. \tag{7}$$

These currents are combined with the input disturbances $\underline{d}_i$, forming the inputs to the translational plant. These input disturbances are caused by the misalignment of the rigid body mass and elastic centers, as discussed above. The input disturbance vector $\underline{d}_i$ is a function of geometrical parameters, time, and rotational speed as
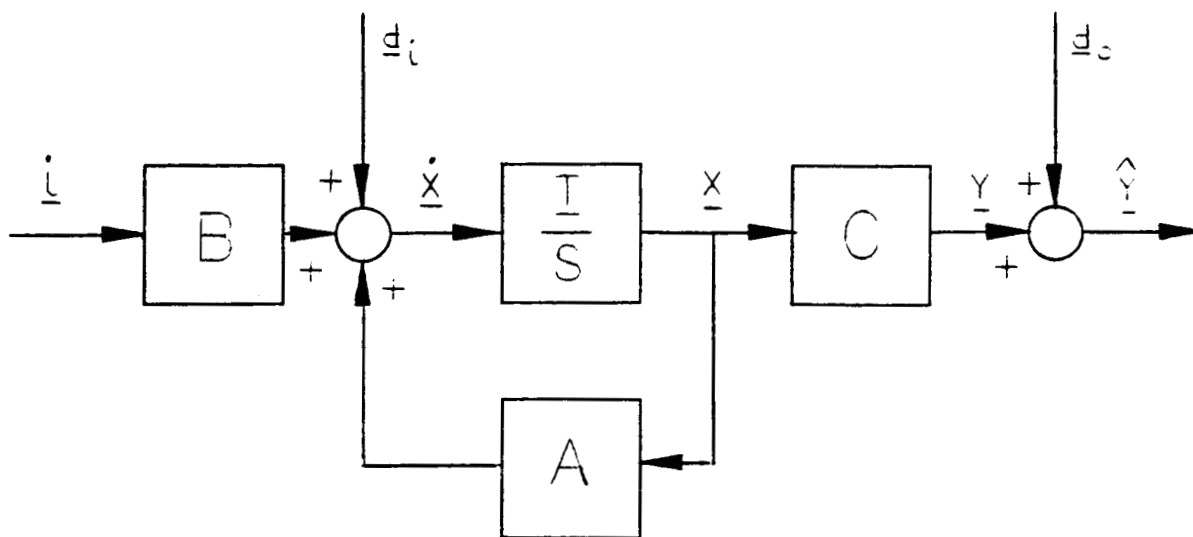
EQUATIONS OF MOTION

$$\dot{\underline{x}}(t) = A\underline{x}(t) + B\underline{i}(t)$$

$$\hat{\underline{y}}(t) = C(sI - A)^{-1}B\underline{i}(t) + C(sI - A)^{-1}\underline{d_i}(t) + \underline{d_o}(t)$$

$\underline{i}(t)$ = Bearing control currents

$\underline{d_i}(t)$ = Force disturbance caused by spoke misalignment

$\underline{x}(t)$ = System state vector

$\underline{y}(t)$ = System output, the hub center of mass position

$\hat{\underline{y}}(t)$ = Measured hub position

$\underline{d_o}(t)$ = Measurement disturbance

Figure 6.   Translational Model: Standard State Space Form

27

$$
\underline{d}_i \;=\;
\begin{bmatrix}
0 \\[4pt]
0 \\[4pt]
-\dfrac{k_r}{k_{1t}}\,(\epsilon_f \cos(\Omega t + \alpha_f) \;-\; \epsilon_h \cos(\Omega t)) \\[10pt]
\dfrac{k_r}{k_{1t}}\,(\epsilon_f \cos(\Omega t + \alpha_f) \;-\; \epsilon_h \cos(\Omega t)) \\[10pt]
0 \\[4pt]
0 \\[4pt]
-\dfrac{k_r}{k_{1t}}\,(\epsilon_f \sin(\Omega t + \alpha_f) \;-\; \epsilon_h \sin(\Omega t)) \\[10pt]
\dfrac{k_r}{k_{1t}}\,(\epsilon_f \sin(\Omega t + \alpha_f) \;-\; \epsilon_h \sin(\Omega t))
\end{bmatrix}
\tag{8}
$$

where

k_{1t} = Lorentz bearing translational force/input current proportionality constant [Johnson 1987b]

The state vector $\underline{x}$ of the translational plant is given by

$$
\underline{x} \;=\; [x_f,\; x_h,\; \dot{x}_f,\; \dot{x}_h,\; y_f,\; y_h,\; \dot{y}_f,\; \dot{y}_h]^T,
\tag{9}
$$

the x and y positions and velocities of the flywheel and hub centers of mass. The output of the plant $\underline{y}$ is assumed to consist of the hub center of mass x and y positions x_h and y_h as

$$
\underline{y} \;=\; [x_h,\; y_h]^T
\tag{10}
$$

The plant matrices **A**, **B**, and **C** are given by

$$
A = \begin{bmatrix}
0 & 0 & I & 0 & 0 & 0 & 0 & 0 \\
0 & 0 & 0 & I & 0 & 0 & 0 & 0 \\
\dfrac{-k_r}{m_f} & \dfrac{k_r}{m_f} & \dfrac{-c_r}{m_f} & \dfrac{c_r}{m_f} & \dfrac{-\Omega c_r}{m_f} & \dfrac{\Omega c_r}{m_f} & 0 & 0 \\
\dfrac{k_r}{m_h} & \dfrac{-k_r}{m_h} & \dfrac{c_r}{m_h} & \dfrac{-c_r}{m_h} & \dfrac{\Omega c_r}{m_h} & \dfrac{-\Omega c_r}{m_h} & 0 & 0 \\
0 & 0 & 0 & 0 & 0 & 0 & I & 0 \\
0 & 0 & 0 & 0 & 0 & 0 & 0 & I \\
\dfrac{\Omega c_r}{m_f} & \dfrac{-\Omega c_r}{m_f} & 0 & 0 & \dfrac{-k_r}{m_f} & \dfrac{k_r}{m_f} & \dfrac{-c_r}{m_f} & \dfrac{c_r}{m_f} \\
\dfrac{-\Omega c_r}{m_h} & \dfrac{\Omega c_r}{m_h} & 0 & 0 & \dfrac{k_r}{m_h} & \dfrac{-k_r}{m_h} & \dfrac{c_r}{m_h} & \dfrac{-c_r}{m_h}
\end{bmatrix}
\tag{11}
$$

$$
B = \begin{bmatrix}
0 & 0 \\
0 & 0 \\
0 & 0 \\
\dfrac{k_{lt}}{m_h} & 0 \\
0 & 0 \\
0 & 0 \\
0 & 0 \\
0 & \dfrac{k_{lt}}{m_h}
\end{bmatrix}
\tag{12}
$$

$$
C = \begin{bmatrix}
0 & 1 & 0 & 0 & 0 & 0 & 0 & 0 \\
0 & 0 & 0 & 0 & 0 & 1 & 0 & 0
\end{bmatrix}
\tag{13}
$$

29

The measurement of the hub center of mass position is corrupted by misalignment between the center of measurement and the hub center of mass, as discussed above. This misalignment can be expressed as an output disturbance $\underline{d}_o$, as shown in Figure 6, where

$$\underline{d}_o = [\epsilon_s \cos(\Omega t + \alpha_s), \ \epsilon_s \sin(\Omega t + \alpha_s)]^T \tag{14}$$

The measurement of hub position available to the controller $\underline{y}$ is the combination of the actual hub center of mass position $\underline{y}$ and the disturbance $\underline{d}_o$, as shown in Figure 6.

The state-space equations shown in Figure 6 provide a model of the translational dynamics using a real, time domain formulation. The frequency domain block diagram of the model is shown in Figure 7. The plant transfer function relating the input currents $\underline{i}$ to the hub center of mass position $\underline{y}$ is

$$G(s) = C(sI - A)^{-1}B \tag{15}$$

The input disturbances are related to the hub center of mass position by the same transfer function. The measurement of hub position available to the controller is

$$\underline{Y}(s) = \underline{Y}(s) + \underline{D}_o(s) = G(s)\underline{I}(s) + C(sI - A)^{-1}\underline{D}_i(s) + \underline{D}_o(s) \tag{16}$$

where the various Laplace transforms are defined in Figure 7.

Complex notation can be used to express the translational dynamics, giving a more compact notation. The complex, time domain block diagram is shown in Figure 8. The input is the

30
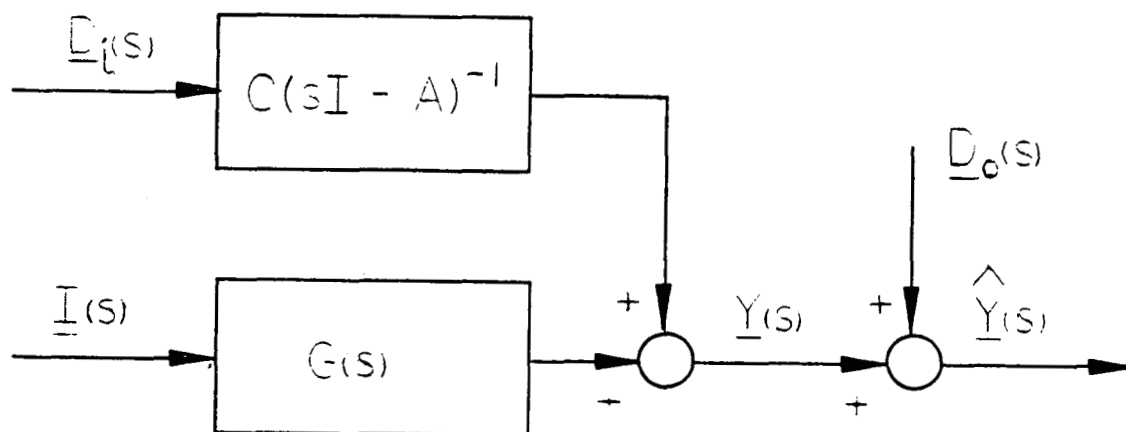
$\hat{\underline{Y}}(s)$ = Laplace transform of measured hub position $\underline{y}(t)$

$\underline{Y}(s)$ = Laplace transform of the hub center of mass position $\underline{y}(t)$

$\underline{D}_i(s)$ = Laplace transform of force (spoke misalignment)

disturbance $\underline{d}_i(t)$

$\underline{I}(s)$ = Laplace transform of input (Lorentz bearing) currents $\underline{i}(t)$

$\underline{D}_o(s)$ = Laplace transform of output (measurement) disturbance $\underline{d}_o(t)$

Figure 7.   Translational Model: Standard Transfer Function Form

31
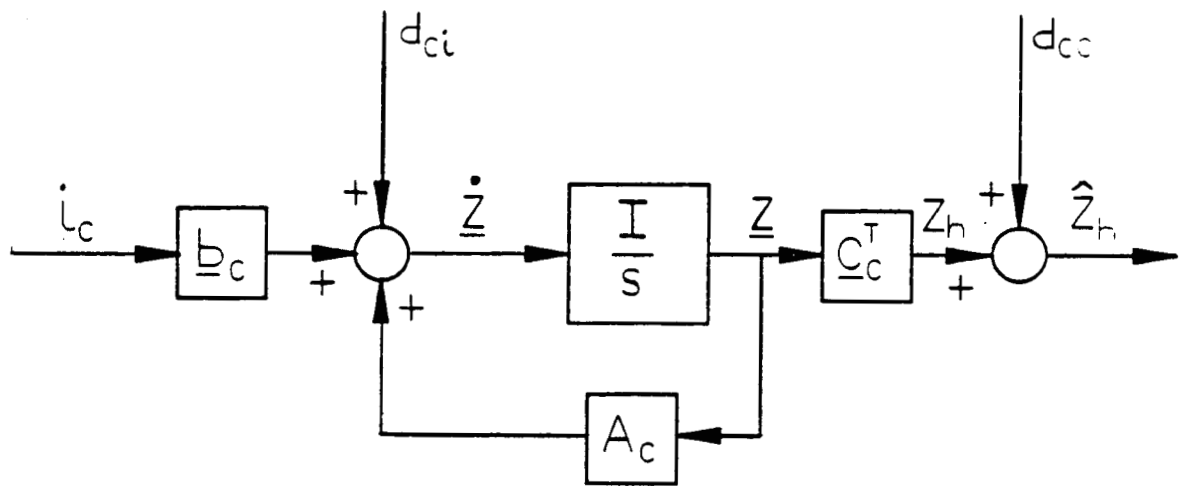
EQUATIONS OF MOTION

$$\dot{\underline{z}}(t) = A_c\underline{z}(t) + \underline{b}_c i_c(t)$$

$$\hat{\underline{z}}_h(t) = \underline{c}_c^T(sI - A)^{-1}\underline{b}_c i_c(t) + \underline{c}_c^T(sI - A)^{-1}\underline{d}_{ci}(t) + d_{co}(t)$$

$i_c(t)$ = Complex bearing control current

$\underline{d}_{ci}(t)$ = Complex force disturbance vector, caused by spoke
misalignment

$\underline{z}(t)$ = Complex system state

$z_h(t)$ = System output, complex postion of the hub center of mass

$d_{co}(t)$ = Complex measurement disturbance

$\hat{z}_h(t)$ = Measured hub position

Figure 8. Translational Model: Complex State Space Form

complex Lorentz bearing current i_c containing the two Lorentz translational currents as

$$i_c = i_x + j i_y. \tag{17}$$

This scalar, complex current is combined with the complex input disturbances d_{ci} to form the complex input to the translational plant. The complex input disturbance is given as

$$d_{ci} = \begin{bmatrix} 0 \\ 0 \\ -\dfrac{k_r}{k_{lt}} (\epsilon_f e^{(j\alpha_f)} - \epsilon_h) e^{j\Omega t} \\ \dfrac{k_r}{k_{lt}} (\epsilon_f e^{(j\alpha_f)} - \epsilon_h) e^{j\Omega t} \end{bmatrix} \tag{18}$$

The complex state vector $\underline{z}$ of the translational plant is given by

$$\underline{z} = [z_f, z_h, \dot{z}_f, \dot{z}_h]^T \tag{19}$$

where z_f and z_h are the complex scalars describing the position of the flywheel and hub centers of mass. The output of the plant, consisting of the hub center of mass x and y positions x_h and y_h is expressed as a complex scalar

$$y_c = x_h + j y_h. \tag{20}$$

The plant is now described by complex coefficient matrices $\underline{A}_c$, $\underline{b}_c$, and $\underline{c}_c$ that are given by

$$
A_c = \begin{bmatrix}
0 & 0 & 1 & 0 \\
0 & 0 & 0 & 1 \\
\dfrac{-k_r + j\Omega c_r}{m_f} & \dfrac{k_r - j\Omega c_r}{m_f} & \dfrac{-c_r}{m_f} & \dfrac{c_r}{m_f} \\
\dfrac{k_r - j\Omega c_r}{m_h} & \dfrac{-k_r + j\Omega c_r}{m_h} & \dfrac{c_r}{m_h} & \dfrac{-c_r}{m_h}
\end{bmatrix}
$$
(21)

$$
\underline{b}_c^T = \begin{bmatrix} 0 & 0 & 0 & \dfrac{k_{1t}}{m_h} \end{bmatrix}
$$
(22)

$$
\underline{c}_c = \begin{bmatrix} 0 & 1 & 0 & 0 \end{bmatrix}
$$
(23)

The output disturbance d_{co} is now a complex scalar given by

$$
d_{co} = \epsilon_s e^{j(\Omega t + \alpha_s)}.
$$
(24)

The measurement of hub position available to the controller is now a complex scalar y_c that is the sum of the complex scalar disturbance d_{co} and the actual hub center of mass position, given by the complex scalar y_c.

This complex, time domain representation of Figure 8 is similar to the real formulation given in Figure 6, but the size of all vectors have been halved. In particular, the two-vectors of the real formulation describing current $\underline{i}$, output disturbance $\underline{d}_o$, hub position $\underline{y}$, and measured hub position $\underline{y}$ have all become complex scalars when the complex representation is used.

34

This complex time domain representation has a frequency counterpart, shown in Figure 9. The special properties of these complex coefficient transfer functions are presented in detail in Chapter 4 of Johnson [1987a].

These real and complex equations of motion for the translational dynamics of the ACCESS system provide models capable of predicting both the non-synchronous and synchronous response. With the input and output disturbances neglected, the above models are appropriate for the analysis of the synchronous response of the ACCESS translational dynamics, including the important consideration of stability. With the addition of the disturbances, these models are capable of predicting the forced, synchronous response caused by misalignments between the inertial, measurement, and elastic components, which are the mass unbalances of conventional rotor dynamics.

2.3 Radial Torques and Angular Measurements

In the same manner as for the translational dynamics, the forced, synchronous model for the angular dynamics is found by incorporating the potential misalignments between the centers of force of the spoke structure, centers of mass of the rigid bodies, and center of force of the Lorentz bearings into the model. In this angular case, however, the differences in orientation of the elastic axes of the rigid bodies, the principal inertial axes of the rigid-body masses, and the reference axes of the measurement system must also be considered. Since the rigid bodies and spoke structure are
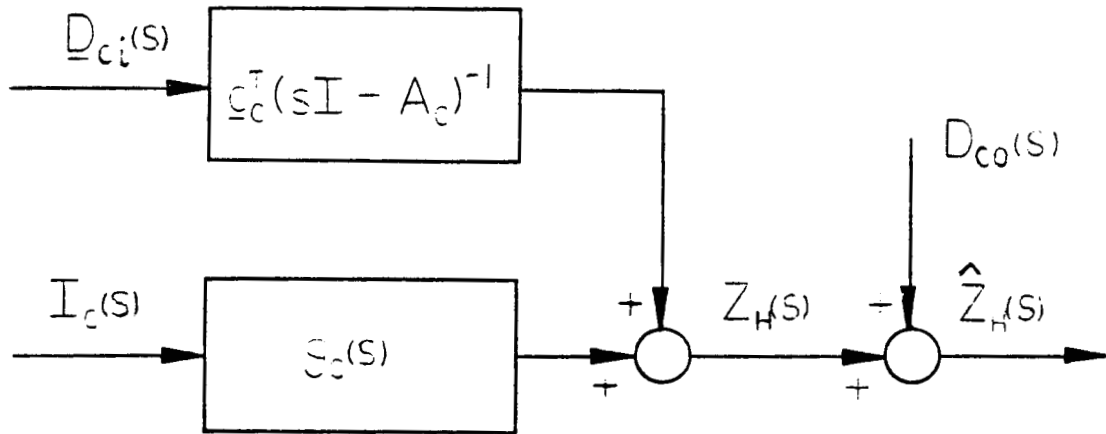
$I_c(s)$ = scalar Laplace transform of the complex input current $i_c(t)$

$\underline{D}_{ci}(s)$ = vector Laplace transform of the complex force disturbance $\underline{d}_{ci}(t)$

$Z_h(s)$ = scalar Laplace transform of the complex scalar $z_h(t)$ describing the hub center of mass position

$D_{co}(s)$ = scalar Laplace transform of the complex output disturbance $d_{co}(t)$

$\hat{Z}_h(s)$ = scalar Laplace transform of the measured hub position $\hat{z}_h(t)$

$g_c(s)$ = $\underline{c}_c^T(sI - A_c)^{-1}\underline{b}_c$, the scalar (SISO) complex coefficient, translational transfer function.

Figure 9.   Translational Model: Complex Coefficient Transfer Function Form

assumed axisymmetric, only the axial elastic or inertial axes are uniquely defined. Therefore, only the orientations of the axial axes, both inertial and elastic, need be specified for each rigid body.

For each rigid-body mass, an elastic axes set has been defined such that when the elastic axes set of each rigid body has the same orientation, no elastic torques are produced by the spoke structure. In other words, if these two sets of elastic axes have the same orientation over any period of time, the spoke structure produces no elastic or damping torques over that time period. As noted above, the orientation of these elastic axes is determined by specifying the orientation of only the axial elastic axis.

For small differences in orientation, the orientation of the axes can be described by Bryant angles ϕ and θ considered as vector quantities, as developed in Johnson [1987b]. For example, the orientation of the axial, elastic axis and axial inertial axis of a single rigid body is shown in Figure 10. The orientation of these axes is shown relative to the fixed reference frame given by the X-Y-S axes. The axial inertial axis is shown intersecting the radial (X-Y) plane at center of mass M_h and the axial elastic axis intersecting the radial plane at the center of elastic force E_h. These points, of course, are the origins of the principal axes of inertia and the elastic axes. The orientations of the two axial axes, I_{zz} and E_{zz}, are given by the two sets of Bryant angles, ϕ_i and θ_i for the axial inertial

axis and ϕ_e and θ_e for the axial elastic axis. The plane containing these two axial axes is fixed in the rigid body. Also, importantly, the orientation of these two axes is fixed relative to one another.

The relative orientation of the two axes can be more readily seen if the two axes are plotted with a common origin as shown in Figure 11. Also shown in Figure 11 are projections onto the radial (X-Y) plane of unit magnitude vectors aligned with the axial elastic axis and the axial inertial axis. These projections are given by the line segment OP_i for the inertial axis and OP_e for the elastic axis. Note that these line segments, as well as the line segment P_iP_e are fixed in the rigid body and, to first order, spin about the S-axis with rotational speed Ω and fixed orientation relative to one another.
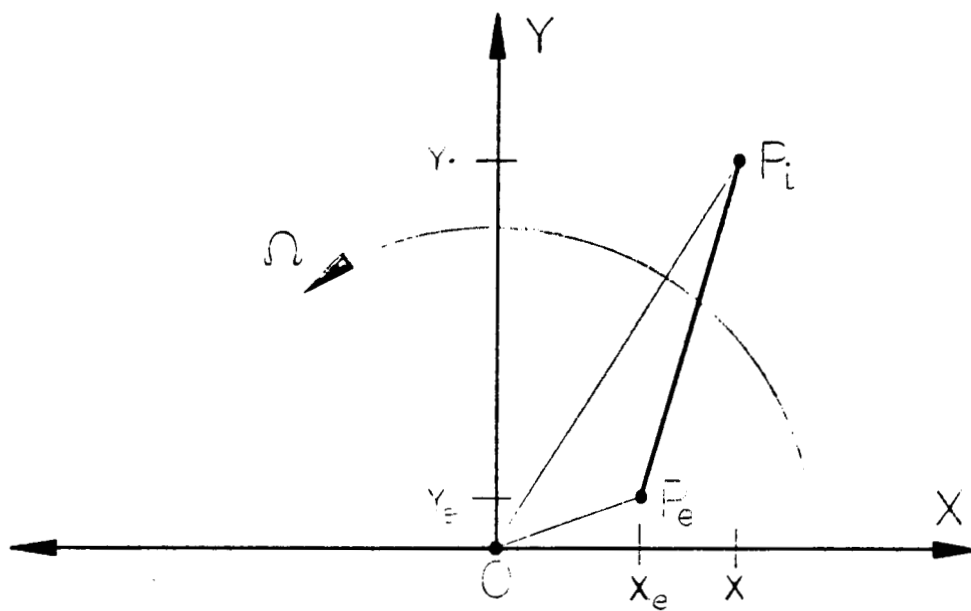
The relative orientation of the axial elastic and inertial axes has been shown to be fixed in the rigid body and spinning with the rigid body angular velocity Ω. These results were obtained by considering the projection of these axial elastic and inertial axes into the radial (X-Y) axes. These results can be expressed in the (ϕ-θ) coordinates as shown in Figure 12(a) and 12(b). Figure 12(a) is the radial (X-Y) plane of Figure 11. Shown are the body fixed line segments OP_i and OP_e that describe the orientation of the axial inertial axis and the axial elastic axis, as discussed above. In the ϕ-θ coordinate system the orientations are given by points labelled ψ for the inertial and χ for the elastic axes. The line segment $X\psi$ in Figure 12(b) is

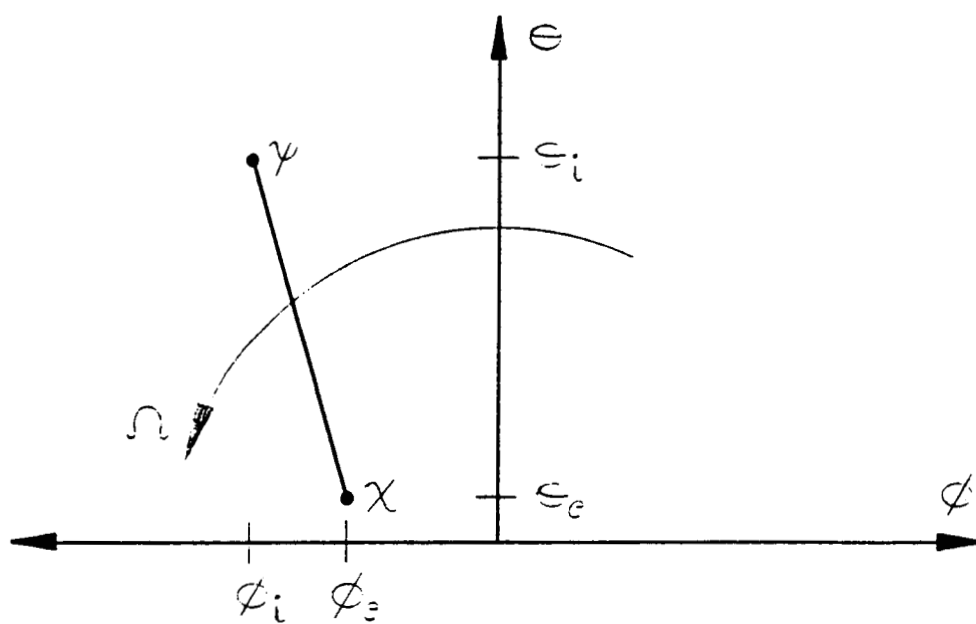Figure 10. Angular Orientation of a Single Rigid Body
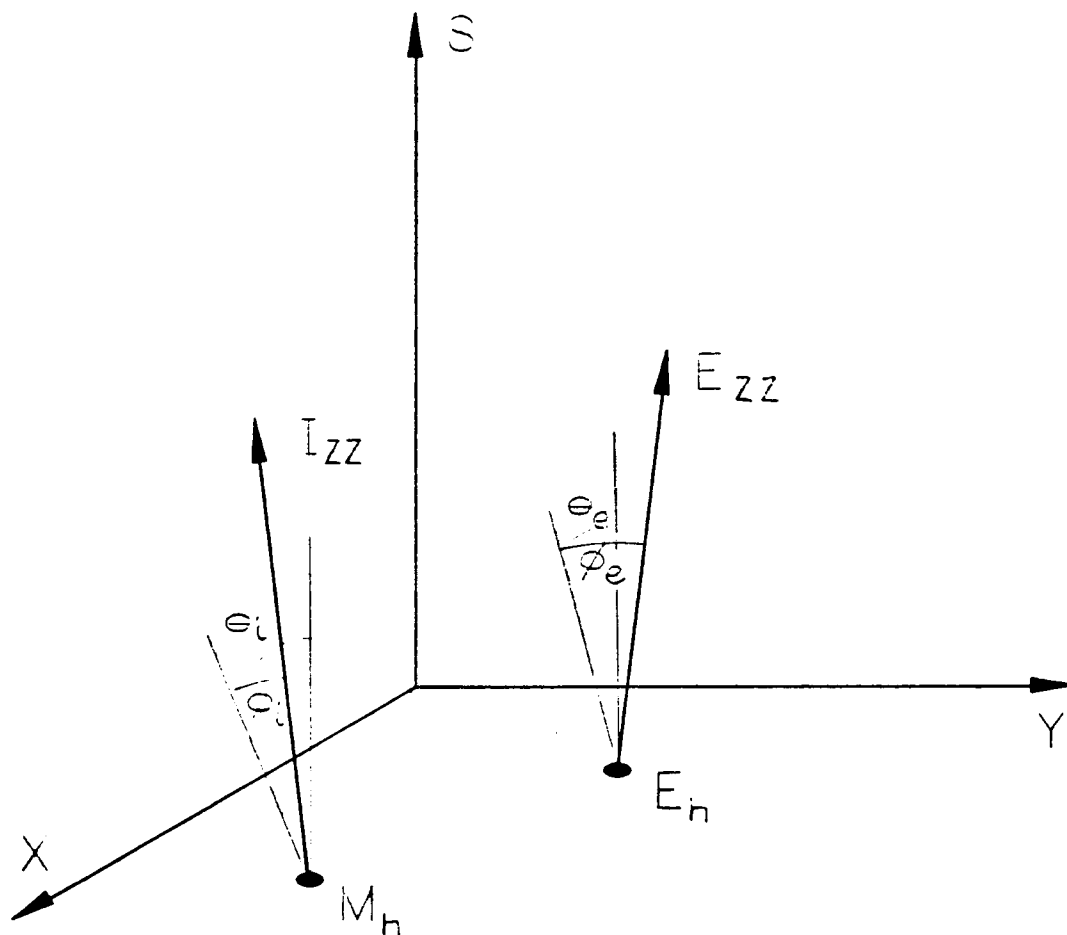
M_h — Hub center of mass

E_h — Hub elastic center

I_{zz} — Axial principal axis of inertia

I_{zz} — Elastic axial principal axis

Figure 11.   Relative Orientation of Inertial and Elastic Axes

a) Radial Plane

b) Bryant Angles

Figure 12.   Projection of the Relative Orientation of
            Inertial and Elastic Axes

analogous to the line segment P_eP_i in Figure 12(a). The line segment P_eP_i was shown to rotate relative to the inertial X-Y axes with angular velocity Ω. Similarly, the line segment rotates with angular velocity Ω in the ϕ-θ plane with the direction of rotation shown in Figure 12(b). This, then, is the desired result: the ϕ-θ coordinate pairs that describe the orientation of the axial inertial and elastic axes are fixed relative to one another in the ϕ-θ plane and rotate with angular velocity Ω.

The angular orientation of both rigid bodies, the elastic structure, and the measurement axes can be expressed in the ϕ-θ plane as shown in Figure 13. The axial inertial axis of the hub rigid body has angular orientation given by ψ_h. The axial elastic axis of the hub has angular orientation given by X_h. The measurement system is assumed to measure the orientation of a third axis fixed in the hub rigid body given by Φ_h. These three axes are fixed in the hub rigid body, and in lieu of the above developments, the line segments ψ_hX_h and $X_h\Phi_h$ rotate in the ϕ-θ plane with angular velocity Ω in the direction shown. Their relative orientations are fixed, as discussed above, and given by angular vector magnitudes ξ_h and ξ_s with relative angles β_h and β_s as shown in Figure 13. For the flywheel, the orientation of the axial inertial axis is given by ψ_f and the orientation of the axial elastic axis is given by X_f. These axes are fixed in the flywheel rigid body and the coordinates that denote their orientation rotate with angular velocity Ω when seen in the ϕ-θ

42
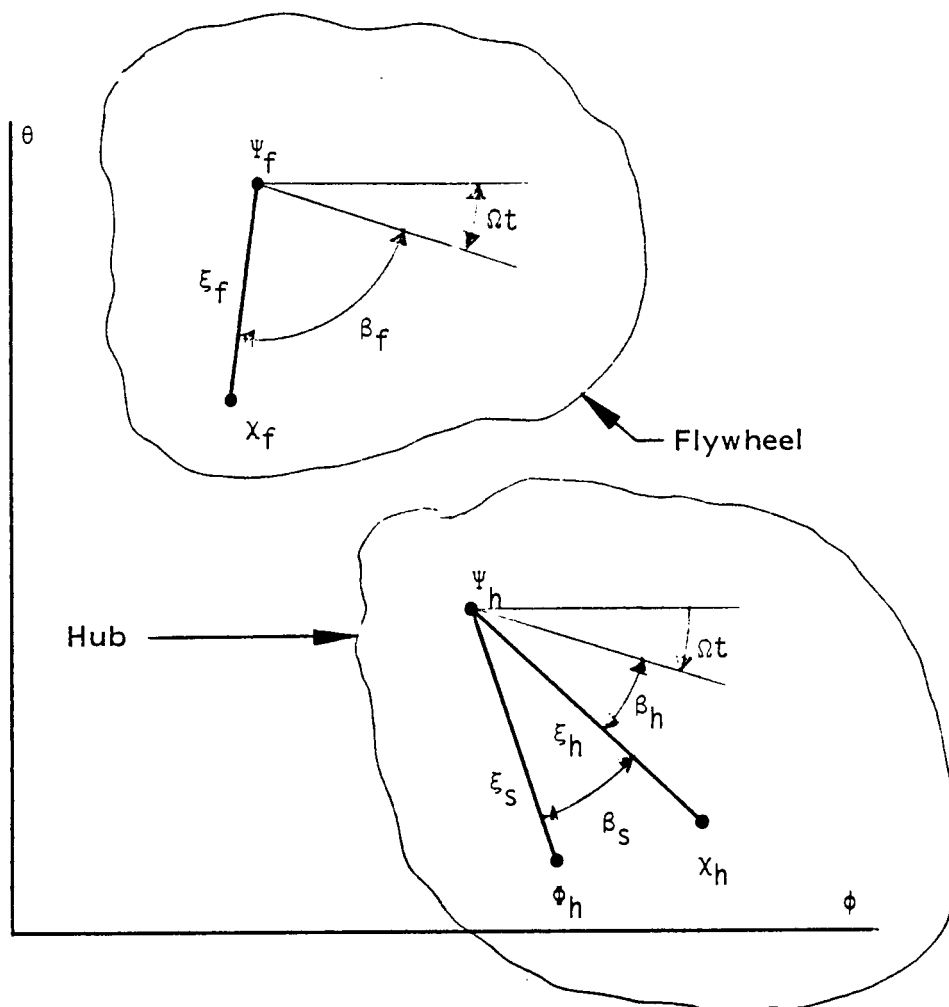
Ψ_h — Orientation of hub axial principal axis of inertia

X_h — Orientation of the hub elastic axial principal axis

Φ_h — Orientation of the measurement axis

Ψ_f — Orientation of the flywheel axial principal axis of inertia

X_f — Orientation of the flywheel elastic axial principal axis

Figure 13. Angular Model Geometry

43

plane. Their relative orientation is given by the magnitude ξ_f and the angle β_f, similar to the hub notation. In general, the relative orientation of the hub and flywheel are functions of nominal spin speed Ω and time. If the system is spinning in steady state, however, the relative orientations between all the elastic and inertial axes are fixed and ξ_h, ξ_s, ξ_f, β_h, β_s, and β_f are all constants.

The framework is now in place to analyze the torque produced by the spoke structure. The torque produced by the spoke structure is given, as developed in Johnson [1987b] (Equation A.1.8), by

$$\underline{M}_s = -k_a \Delta \underline{X} - c_a \frac{d}{dt}(\Delta \underline{X}) + c_a \Omega \underline{X} \qquad (25)$$

where now the relative angular orientation $\Delta \underline{X}$ is given by the relative orientation of the elastic axes

$$\begin{aligned}
\Delta \underline{X} = \underline{X}_f - \underline{X}_h &= [\phi_f - \phi_h + \xi_f \cos(\Omega t + \beta_f) - \xi_h \cos(\Omega t + \beta_h)]\underline{i} \\
&+ [\theta_f - \theta_h + \xi_f \sin(\Omega t + \beta_f) - \xi_h \sin(\Omega t + \beta_h)]\underline{i}.
\end{aligned}$$

$$(26)$$

and where

   k_a is the spoke angular spring constant and

   c_a is the spoke angular damping constant

The torque produced by the spoke structure and acting about the elastic center of the hub is now

$$
\begin{aligned}
\underline{M}_s =\ & -[k_a(\phi_f - \phi_h) + c_a\Omega(\theta_f - \theta_h) + c_a(\phi_f - \dot{\phi}_h)]\underline{i} \\
& - [k_a(\theta_f - \theta_h) + c_a\Omega(\phi_f - \phi_h) - c_r(\dot{\theta}_f - \theta_h)]\underline{j} \\
& - k_a[\xi_f\cos(\Omega t + \beta_f) - \xi_h\cos(\Omega t + \beta_h)]\underline{i} \\
& - k_a[\xi_h\sin(\Omega t + \beta_f) - \xi_h\sin(\Omega t + \beta_h)]\underline{j}
\end{aligned}
$$

(27)

The first two lines of Equation 27 are the same as developed for the non-synchronous model [Johnson 1987b]. The effects of the misalignment of elastic and inertial axes are seen in the last two lines of Equation 27. These additional torques caused by the misalignment may be considered as disturbance torques acting on the system. Note that these disturbance torques are sinusoidal functions of time with a frequency of Ω, the rotational speed of the system.

The disturbance torque given by Equation 27 acts about the elastic center of the hub rigid body. An equal and opposite torque acts about the elastic center of the flywheel. Because these torques are equal and opposite, they produce no net torque acting to disturb the rigid body motion of the combined hub-flywheel system. Therefore, the misalignment of the inertial and elastic axes of the hub and flywheel produces a disturbance torque that excites only the flexible modes of the angular dynamics. These results are similar to the results derived earlier for the disturbance force caused by misalignment of the elastic and inertial centers of the hub and flywheel.

The disturbance torque derived above acts about the elastic centers of the hub and flywheel. In addition to this disturbance

torque, there is another torque, a coupling torque, that acts about the centers of mass of the hub and flywheel. This coupling torque is caused by the translational forces produced by the spoke structure or bearing. The translational force produced by the spoke structure acts through the elastic centers of the hub and flywheel, as discussed above. The bearing force acts through a point not generally fixed in either stator or rotor coordinates. These forces can produce radial coupling torques about the hub and flywheel centers of mass if the elastic, mass, and bearing force centers are not aligned in the axial direction.

If the hub and flywheel centers of mass are displaced in the axial direction from the their respective elastic centers or the hub center of mass is displaced axially from the bearing center of force, there will be a disturbance torque that couples the translational dynamics, through the magnitude of the force, and the axial dynamics, through the relative axial displacements of the various mass, elastic, and bearing centers, to the angular (tilt) dynamics. Although these axial misalignments provide a mechanism to couple the angular and translational dynamics, they are small effects since they depend on small scale geometric imperfections. In the interest of model simplicity, they were neglected in this investigation.

Another source of disturbance is possible misalignment of the angular sensors. The controller is assumed to have access to a measurement of the orientation of the axial direction of the hub. These angular sensors nominally produce a measurement of

the orientation of the axial inertial axis of the hub. These
sensors, however, actually measure the orientation of some
machined surfaces on the hub. The output of the measurement
system is the orientation of a "measurement" axis, which is
defined by the sensed surfaces on the hub. This measurement axis
is assumed fixed in the hub rigid body but will not in general
coincide with either the axial inertial or elastic axes.

The orientation of the measurement axis was shown in Figure
13. The orientation of the measurement axis relative to the
axial principal inertial axis is defined by the magnitude ξ_s and
the angle α_s in the $\phi-\theta$ plane. The output of the measurement
system, which is the orientation of the measurement axis, is
therefore a corrupted measurement of the orientation of the axial
inertial axis of the hub as

$$\phi_s \underline{i} + \theta_s \underline{j} = (\phi_h + \xi_s \cos(\Omega t + \beta_s))\underline{i} + (\theta_h - \xi_s \sin(\Omega t + \beta_s))\underline{j}$$

(28)

Using complex notation the orientation of the measurement axis is
given as

$$\phi_s = \psi_h + \xi_s e^{j(\Omega t + \beta_s)}.$$

(29)

The effect of the measurement error, therefore, is to add a
sinusoidally varying signal to the measurement of the axial
principal inertial axis of the hub. This corrupted measurement
signal will be used as a feedback signal for the magnetic
bearing. This measurement error will produce a disturbance that
will excite both rigid-body and flexible modes of the hub/

47
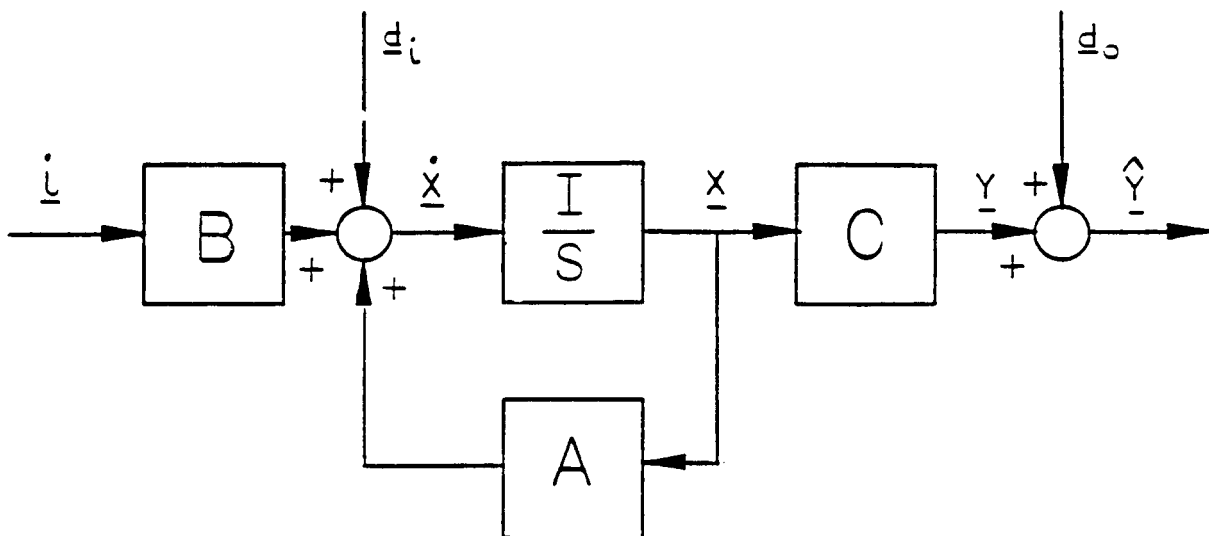
EQUATIONS OF MOTION

$$\dot{\underline{x}}(t) = A\underline{x}(t) + B\underline{i}(t)$$

$$\underline{y}(t) = C(sI - A)^{-1}B\underline{i}(t) + C(sI - A)^{-1}\underline{d}_i(t) + \underline{d}_o(t)$$

$\underline{i}(t)$ = Bearing control currents

$\underline{d}_i(t)$ = Torque disturbance vector caused by spoke misalignment

$\underline{x}(t)$ = System state

$\underline{y}(t)$ = System output, orientation of the hub axial principal axis of inertia

$\underline{d}_o(t)$ = Measurement error

$\hat{\underline{y}}(t)$ = Measured hub orientation

Figure 14. Angular Model: Standard State Space Form

flywheel system. In conventional rotor dynamics, these disturbances are expressed as products of inertia of the rigid bodies relative to the elastic axes.

2.4 ACCESS Angular Dynamics Model

The disturbances, plant equations, and bearing characteristics can now be combined together to produce a input/output model of the ACCESS angular dynamics. In standard state space form, where all variables and matrices are real, the model is given by Figure 14. Note that this model has the same form as the translational dynamics model.

The input to the angular model is the current vector $\underline{i}$ containing the two Lorentz bearing angular currents as

$$\underline{i} = [i_\phi, \quad i_\theta]^T. \tag{30}$$

These currents are combined with the input disturbances $\underline{d}_i$ to form the inputs to the translational plant. These disturbances are caused by the misalignment of the inertial and elastic axes, as discussed above. The input disturbance vector $\underline{d}_i$ is a function of geometrical parameters, time, and rotational speed as

49

$$\underline{d_i} = \begin{bmatrix} 0 \\[1em] 0 \\[1em] -\dfrac{k_a}{k_{la}}(\xi_f\cos(\Omega t + \beta_f) - \xi_h\cos(\Omega t + \beta_h)) \\[1em] \dfrac{k_a}{k_{la}}(\xi_f\cos(\Omega t + \beta_f) - \xi_h\cos(\Omega t + \beta_h)) \\[1em] 0 \\[1em] 0 \\[1em] -\dfrac{k_a}{k_{la}}(\xi_f\sin(\Omega t + \beta_f) - \xi_h\sin(\Omega t + \beta_h)) \\[1em] \dfrac{k_a}{k_{la}}(\xi_f\sin(\Omega t + \beta_f) - \xi_h\sin(\Omega t + \beta_h)) \end{bmatrix} \qquad (31)$$

The state vector $\underline{x}$ of the angular plant is given by

$$\underline{x} = [\phi_f, \phi_h, \dot{\phi}_f, \dot{\phi}_h, \theta_f, \theta_h, \dot{\theta}_f, \dot{\theta}_h]^T \qquad (32)$$

the rotations and angular velocities about the X and Y axes that describe the orientation of the axial inertial axes of the hub and flywheel. The rotations about the X-axis are given by the ϕ's and the rotations about the Y-axis are given by the θ's.

The output of the plant $\underline{y}$ is assumed to consist of the orientation of the axial principal axis of the hub given by the ϕ and θ angles as

$$\underline{y} = [\phi_h, \theta_h]^T. \qquad (33)$$

The plant matrices **A**, **B**, and **C** are given by

$$A = \begin{bmatrix}
0 & 0 & I & 0 & 0 & 0 & 0 & 0 \\
0 & 0 & 0 & I & 0 & 0 & 0 & 0 \\
\dfrac{-k_a}{I_{fr}} & \dfrac{k_a}{I_{fr}} & \dfrac{-c_a}{I_{fr}} & \dfrac{c_a}{I_{fr}} & \dfrac{-\Omega c_a}{I_{fr}} & \dfrac{\Omega c_a}{I_{fr}} & \dfrac{-\Omega I_{fz}}{I_{fr}} & 0 \\
\dfrac{k_a}{I_{hr}} & \dfrac{-k_a}{I_{hr}} & \dfrac{c_a}{I_{hr}} & \dfrac{-c_a}{I_{hr}} & \dfrac{\Omega c_a}{I_{hr}} & \dfrac{-\Omega c_a}{I_{hr}} & 0 & \dfrac{-\Omega I_{hz}}{I_{hr}} \\
0 & 0 & 0 & 0 & 0 & 0 & I & 0 \\
0 & 0 & 0 & 0 & 0 & 0 & 0 & I \\
\dfrac{\Omega c_a}{I_{fr}} & \dfrac{-\Omega c_a}{I_{fr}} & \dfrac{\Omega I_{fz}}{I_{fr}} & 0 & \dfrac{-k_a}{I_{fr}} & \dfrac{k_a}{I_{fr}} & \dfrac{-c_a}{I_{fr}} & \dfrac{c_a}{I_{fr}} \\
\dfrac{-\Omega c_a}{I_{hr}} & \dfrac{\Omega c_a}{I_{hr}} & 0 & \dfrac{\Omega I_{hz}}{I_{hr}} & \dfrac{k_a}{I_{hr}} & \dfrac{-k_a}{I_{hr}} & \dfrac{c_a}{I_{hr}} & \dfrac{-c_a}{I_{hr}}
\end{bmatrix}$$

(34)

$$B = \begin{bmatrix}
0 & 0 \\
0 & 0 \\
0 & 0 \\
\dfrac{k_{la}}{I_{hr}} & 0 \\
0 & 0 \\
0 & 0 \\
0 & 0 \\
0 & \dfrac{k_{lt}}{I_{hr}}
\end{bmatrix}$$

(35)

$$C = \begin{bmatrix}
0 & 1 & 0 & 0 & 0 & 0 & 0 & 0 \\
0 & 0 & 0 & 0 & 0 & 1 & 0 & 0
\end{bmatrix}$$

(36)

The measurement of the hub center of mass position is corrupted by misalignment between the axial inertial axis of the hub and the "measurement" axis, as discussed above. This misalignment can be expressed as an output disturbance $\underline{d}_o$, as shown in Figure 14, where

$$\underline{d}_o = [\xi_s\cos(\Omega t + \beta_s), \ \xi_s\sin(\Omega t + \beta_s)]^T \tag{37}$$

The measurement of hub orientation $\underline{y}$ available to the controller is the combination of the orientation of the axial principal inertial axis of the hub $\underline{y}$ and the disturbance $\underline{d}_o$, as shown in Figure 14.

The state-space equations shown in Figure 14 provide a model of the translational dynamics using a real, time domain formulation. The frequency domain block diagram of the model is shown in Figure 15. The plant transfer function matrix relating the input currents $\underline{i}$ to the hub orientation $\underline{y}$ is

$$G(s) = C(sI - A)^{-1}B \tag{38}$$

The input disturbances are related to the hub center of mass position by the same transfer function. The measurement of hub orientation available to the controller is

$$\underline{Y}(s) = \underline{Y}(s) + \underline{D}_o(s) = G(s)\underline{I}(s) + C(sI - A)^{-1}\underline{D}_i(s) + \underline{D}_o(s) \tag{39}$$

where the various Laplace transforms are defined in Figure 15.

Complex notation can be used to express the translational dynamics giving a more compact notation. The complex, time
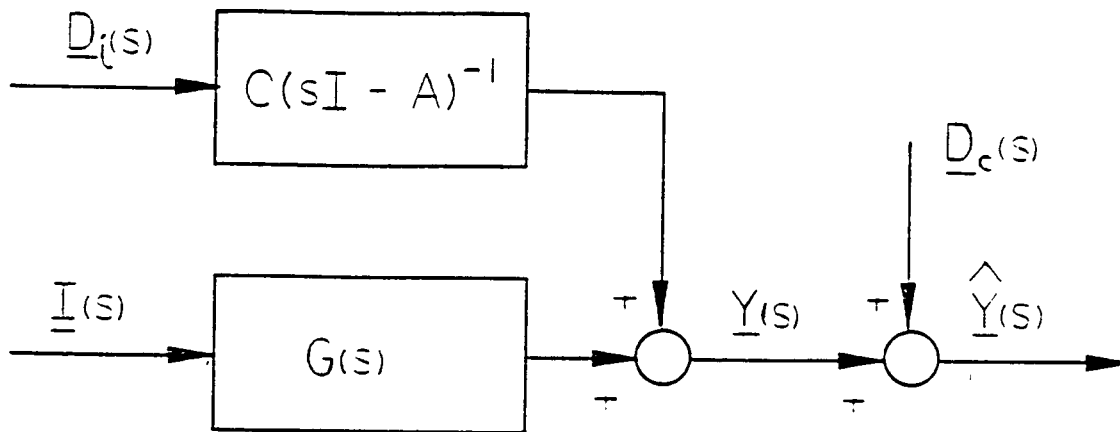
$$\hat{Y}(s) \quad = \quad \text{Laplace transform of measured hub orientation } \hat{y}(t)$$

$$Y(s) \quad = \quad \text{Laplace transform of the actual hub orientation}$$
$$\text{(orientation of axial inertial axis of the hub) } y(t)$$

$$D_i(s) \quad = \quad \text{Laplace transform of torque disturbance } d_i(t)$$

$$I(s) \quad = \quad \text{Laplace transform of input (Lorentz bearing) currents } i(t)$$

$$D_o(s) \quad = \quad \text{Laplace transform of output (measurement) disturbance}$$
$$d_o(t)$$

Figure 15. Angular Model: Standard Transfer Function Form

53

domain block diagram is shown in Figure 16. The input is the complex Lorentz bearing current i_c containing the two Lorentz translational currents as

$$i_c = i_\phi + ji_\theta \tag{40}$$

This scalar, complex current is combined with the complex input disturbances $\underline{d}_{ci}$ to form the complex input to the translational plant. The complex input disturbance is given as

$$\underline{d}_{ci} = \begin{bmatrix} 0 \\ 0 \\ -\dfrac{k_a}{k_{la}}(\xi_f e^{j\beta_f} - \xi_h e^{j\beta_h})e^{j\Omega t} \\ \dfrac{k_a}{k_{la}}(\xi_f e^{j\beta_f} - \xi_h e^{j\beta_h})e^{j\Omega t} \end{bmatrix} \tag{41}$$

The complex state vector $\underline{z}$ of the translational plant is given by

$$\underline{z} = [\psi_f, \psi_h, \dot{\psi}_f, \dot{\psi}_h]^T, \tag{42}$$

where ψ_f and ψ_h are the complex scalars describing the orientation of the flywheel and hub principal axes of inertia. The output of the plant, consisting of the orientation of the hub principal axis of inertia given by the ϕ and θ angles ϕ_h and θ_h is expressed as a complex scalar

$$y_c = \phi_h + j\theta_h = h \tag{43}$$

The plant is now described by complex coefficient matrices A_c, $\underline{b}_c$, and $\underline{c}_c$ that are given by

54
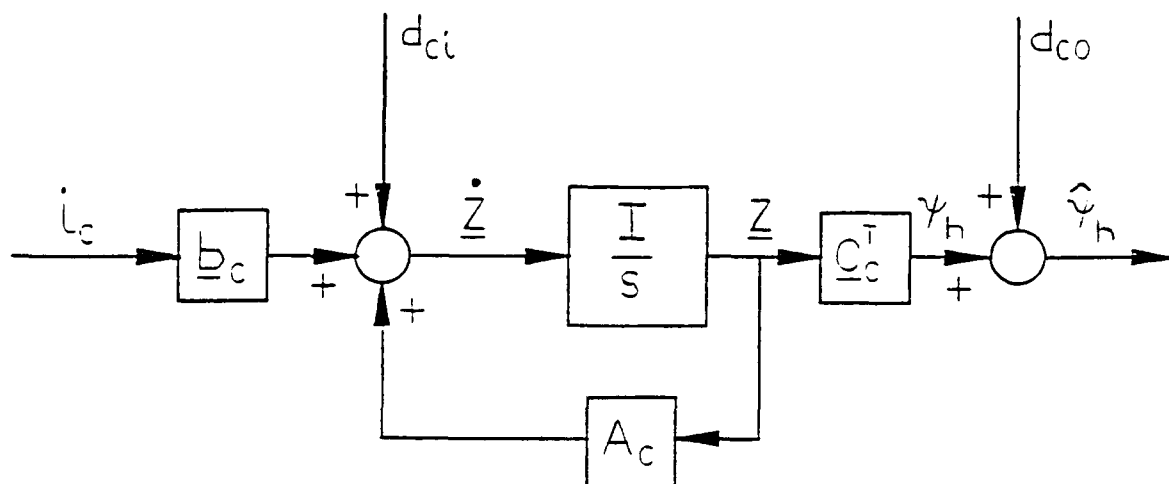
EQUATIONS OF MOTION

$$\dot{\underline{z}}(t) = A_c \underline{z}(t) + \underline{b}_c i_c(t)$$

$$\hat{\Psi}_h(t) = \underline{c}_c^T (sI - A)^{-1} \underline{b}_c i_c(t) + \underline{c}_c^T (sI - A)^{-1} \underline{d}_{ci}(t) + d_{co}(t)$$

$i_c(t)$ = Complex bearing control current

$\underline{d}_{ci}(t)$ = Complex vector of disturbance torques caused by spoke misalignment

$\underline{z}(t)$ = Complex system state

$\Psi_h(t)$ = System output, complex orientation of the hub axial principal axis of inertia

$\hat{\Psi}_h(t)$ = Measured complex hub orientation

$d_{co}(t)$ = Measurement error

Figure 16. Angular Model: Complex State Space Form

55

$$
A_C = \begin{bmatrix} 0 & 0 & 1 & 0 \\[1em] 0 & 0 & 0 & 1 \\[1em] \dfrac{-k_a + j\Omega c_a}{I_{fr}} & \dfrac{k_a - j\Omega c_a}{I_{fr}} & \dfrac{-c_a}{I_{fr}} & \dfrac{c_a + j\Omega I_{fz}}{I_{fr}} \\[1.5em] \dfrac{k_a - j\Omega c_a}{I_{hr}} & \dfrac{-k_a + j\Omega c_a}{I_{hr}} & \dfrac{c_a + j\Omega I_{hz}}{I_{hr}} & \dfrac{-c_a}{I_{hr}} \end{bmatrix}
$$

$$\tag{44}$$

$$
\underline{b}_C^T = \begin{bmatrix} 0 & 0 & 0 & \dfrac{k_{la}}{I_{hr}} \end{bmatrix} \tag{45}
$$

$$
\underline{c}_C = \begin{bmatrix} 0 & 1 & 0 & 0 \end{bmatrix} \tag{46}
$$

The output disturbance d_{co} is now a complex scalar given by

$$
d_{ci} = \xi_s e^{j(\Omega t + \beta_s)} \tag{47}
$$

The measurement of hub position available to the controller is now a complex scalar y_c that is the sum of the complex scalar disturbance d_{co} and the actual hub center of mass position, given by the complex scalar y_c.

This complex, time domain representation of Figure 16 is similar to the real formulation given in Figure 14, but the size of all vectors have been halved. As for the translational model, the two-vectors of the real formulation describing current $\underline{i}$,

output disturbance $\underline{d}_o$, hub position $\underline{y}$, measured hub position $\underline{y}$ have all become complex scalars when the complex representation is used.

This complex time domain representation has a frequency counterpart, given by the complex coefficient transfer function (CCTF), shown in Figure 17.

As for the translational model, these real and complex equations of motion for the angular dynamics of ACCESS provide models capable of predicting both the non-synchronous and synchronous response. With the input and output disturbances neglected, the above models are appropriate for the analysis of the homogeneous or non-synchronous response of the ACCESS angular dynamics, including the important consideration of stability. With the addition of the disturbances, these models are capable of predicting the forced, synchronous response caused by misalignments between the inertial, measurement, and elastic components.
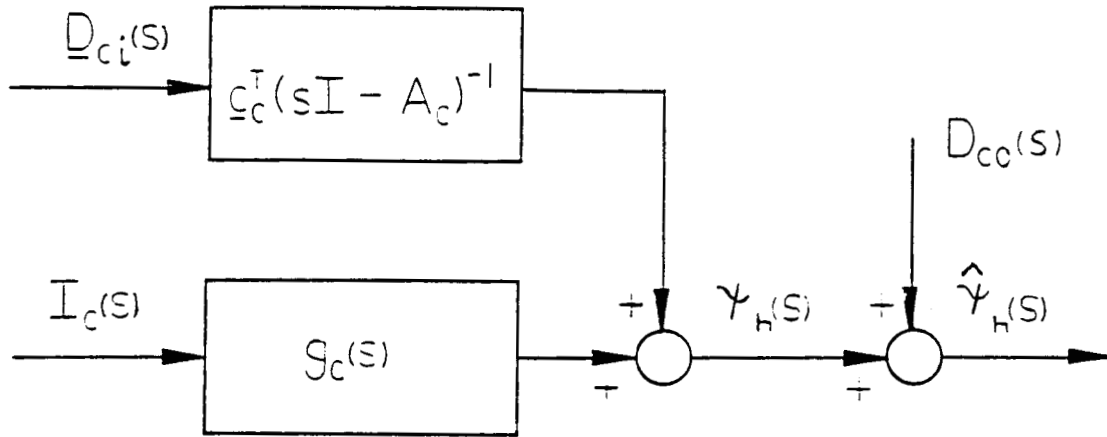
$I_c(s)$ = scalar Laplace transform of the complex input current $i_c(t)$

$\underline{D}_{ci}(s)$ = vector Laplace transform of the complex torque

disturbance $\underline{d}_{ci}(t)$

$\psi_h(s)$ = scalar Laplace transform of the complex scalar $\psi_h(t)$

describing the hub principal inertial axis orientation

$D_{co}(s)$ = scalar Laplace transform of the complex output

disturbance $d_{co}(t)$

$\hat{\psi}_h(s)$ = scalar Laplace transform of the measured hub orientation

$\hat{\psi}_h(t)$

$g_c(s) = c_c^T(sI - Ac)^{-1}\underline{b}_c$, the scalar (SISO) complex coefficient,

Figure 17. Angular Model: Complex Coefficient Transfer
Function Form

58

3. SYNCHRONOUS RESPONSE CONTROL OF RIGID ROTORS

This chapter introduces the four synchronous control approaches that were examined under this research program. These will be investigated for control of the translational dynamics of the ACCES system treated as a rigid-body. Control of a rigid-body rotor simplifies this introductory treatment and allows the important features of each approach to be easily identified.

The four controller design approaches that have been investigated are

1) Mimic conventional bearings with lead-lag compensators

2) Tracking notch filters

3) Tracking differential-notch filters

4) Model based compensators.

These approaches will be presented in the next four sections.

3.1 Lead-Lag Compensation

Lead-lag compensation of the rotor position measurement is the underlying controller for the notch filter compensators. The block diagram of the lead-lag compensator is shown in Figure 18. Shown is the complex single input, single output control loop which describes the dynamics of the two perpendicular, radial axes. For a detailed discussion of complex SISO systems, see Johnson [1987a] or Johnson [1987b]. Alternatively, this loop can be interpreted in a more conventional manner as a single axis of the two identical radial axes. The plant is shown as a simple

Commanded
Position
Input +

Lead-Lag
Compensator

Bearing
Force

$\dfrac{1}{ms^2}$

Plant

Center of
Mass
Position

+

+
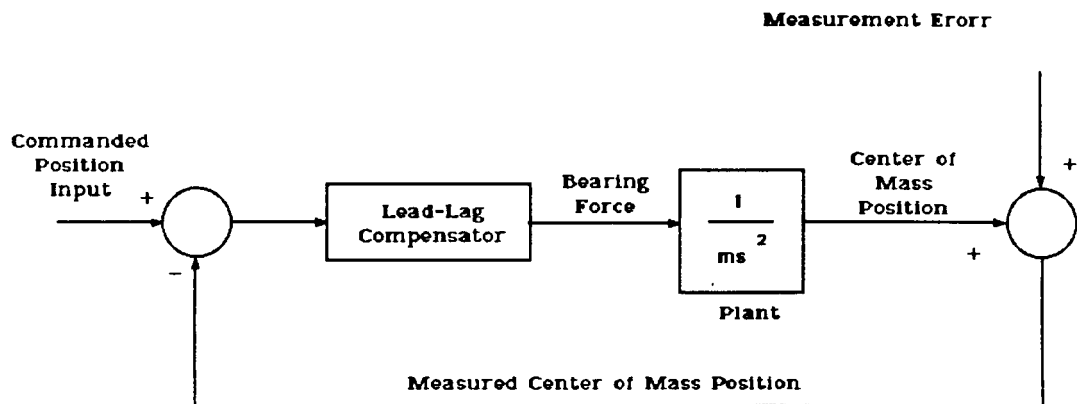
−

Measured Center of Mass Position

Figure 18. Lead-lag Block Diagram

rigid body, double integrator with the radial force as the input
and rotor center of mass position as the output. The measured
center of mass position is corrupted by the measurement error, as
was shown in Figure 5. The measurement error is an additive,
synchronous error at the rotational frequency (Ω). The measured
rotor position is subtracted from the commanded position and used
as input to the lead-lag compensator. Note that the measurement
error or "mass unbalance" manifests itself as an additive output
error.

Bode plots of the lead-lag compensator are shown in Figure
19 along with the transfer function gain of a similar spring-
damper bearing. Note that the lead-lag compensator models the
spring-damper bearing well except at high frequencies past where
the system is crossed over. The one decade of lead shown in
Figure 19 will be used for all the examples presented in this
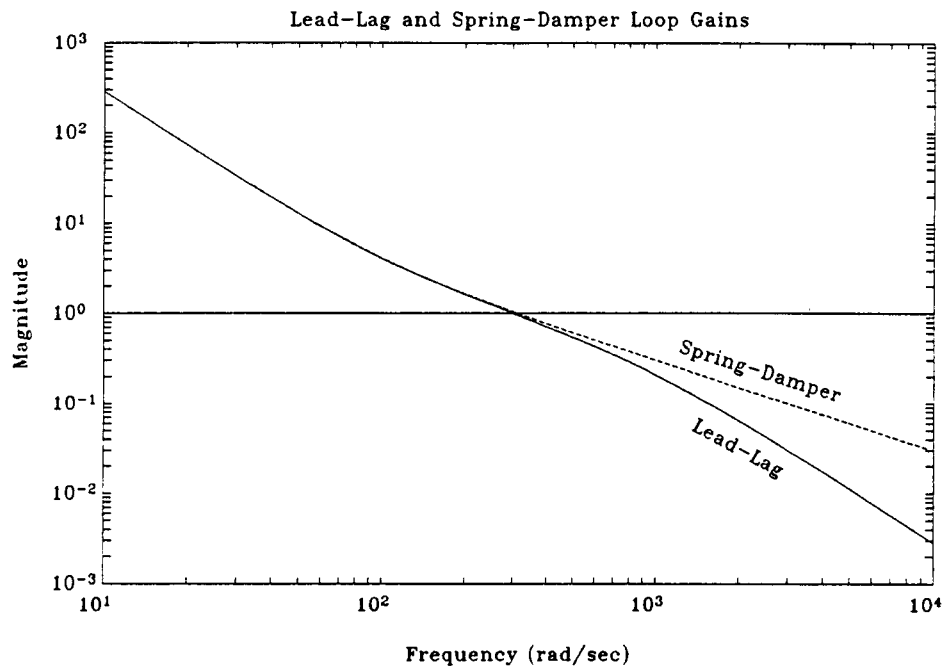report.

Lead-Lag and Spring-Damper Loop Gains

Lead-Lag and Spring-Damper Loop Phases
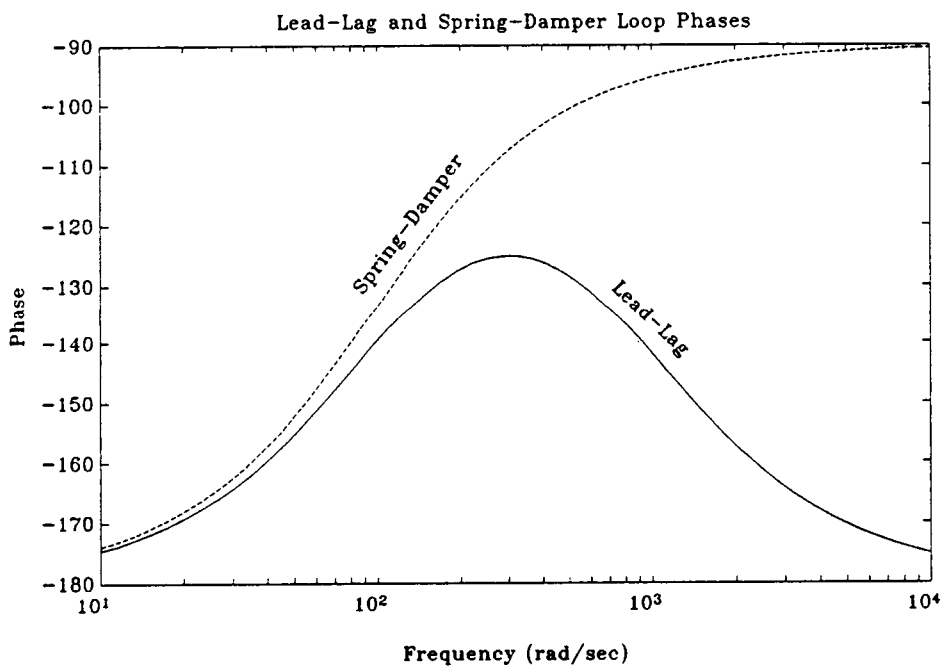
Figure 19.   Lead-lag and Spring-damper Compensator Gain

61

The loop gain of the lead-lag compensator and plant are shown in Figure 20. The rigid-body cross-over frequency is chosen to be 300 rad/sec. Until past cross-over frequencies, the lead-lag and spring-damper are the same, yielding the same closed-loop dynamics inside the closed-loop bandwidth. Because of this, the lead-lag compensator is often used to mimic the behavior of a conventional spring-damper bearing.

In all the results presented in this report, the decade of lead will be centered about the cross-over frequency, as shown in Figure 20. This gives about 60 degrees of phase margin at cross-over, resulting in well damped eigenvalues. Because of the good eigenvalue damping, the synchronous response of the system is well damped. This can be seen in Figure 21, a plot of the normalized center of mass amplitude versus normalized rotational speed. The center of mass amplitude has been normalized by the measurement error distance (ϵ_h), which in conventional rotor systems corresponds to the mass unbalance distance. The rotational speed has been normalized by the loop cross-over frequency (ω_c), which is approximately the critical frequency of the system.

At low subcritical speeds, the system spins about the measurement center S_h with the center of mass whirling about S_h with an amplitude equal to the measurement error distance ϵ_h (see Figures 4 and 5). As the system goes through the critical speed, the center of mass position shows only slight peaking because of the good damping. At higher supercritical speeds the system
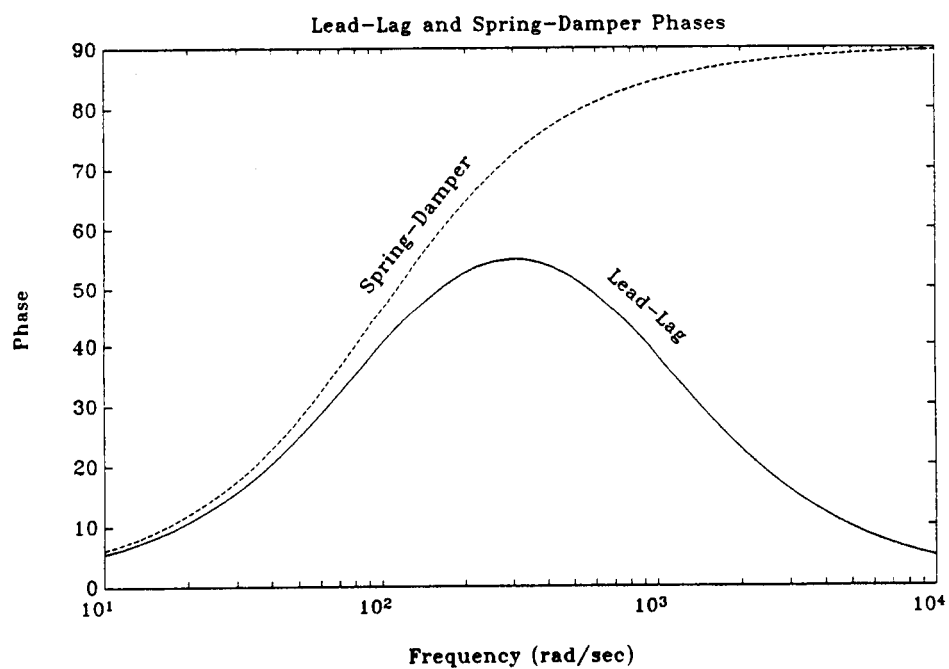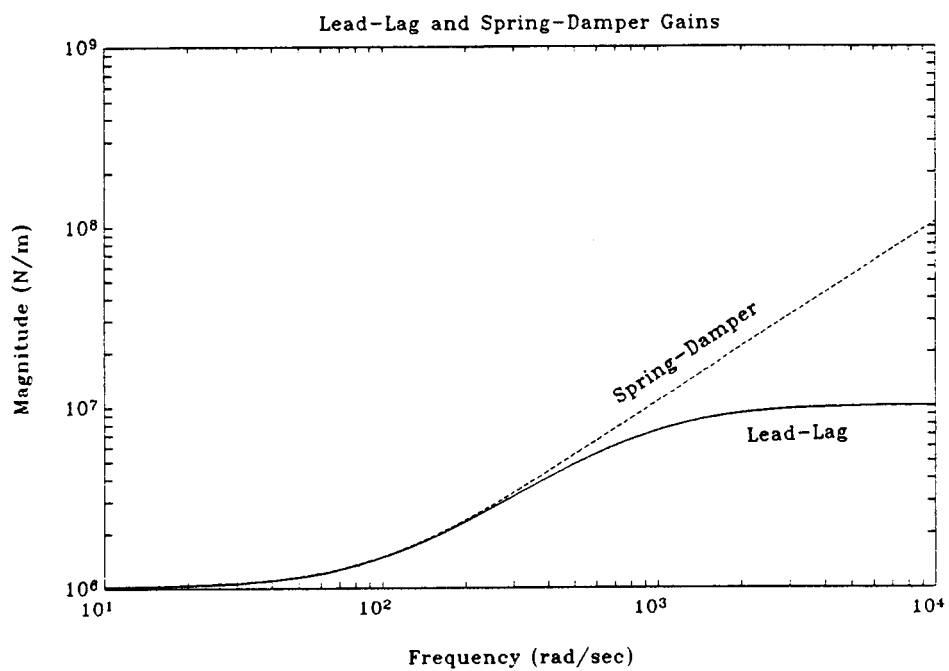
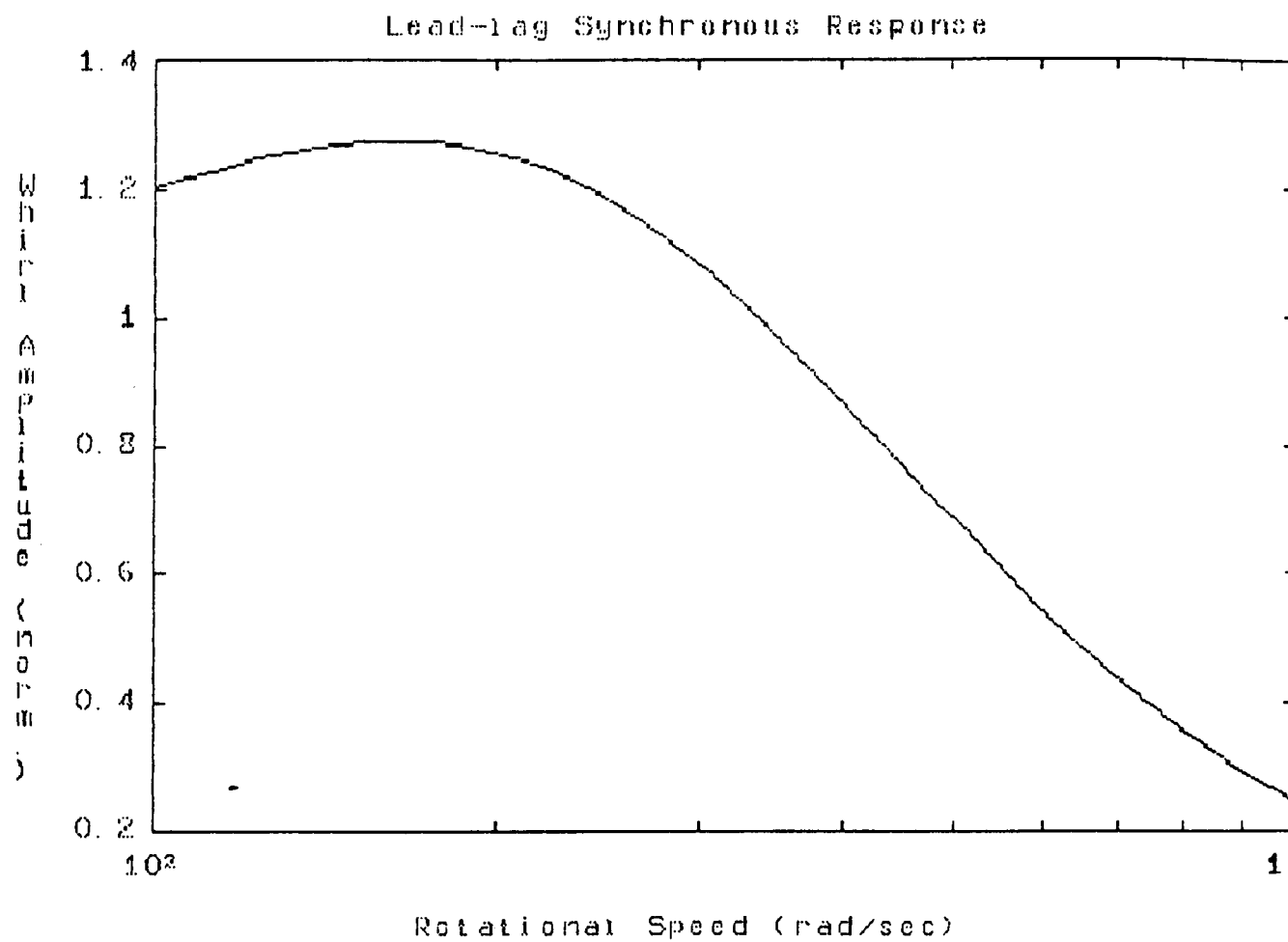Figure 20. Lead-lag and Spring-damper Loop Gain

Figure 21. Synchronous Response with Lead-lag Compensation

spins about the rotor center of mass.

3.2 Lead-Lag Compensator with Tracking Notch

This controller adds a notch filter at the synchronous frequency (rotational speed) into the feedback loop as shown in Figure 22. The notch frequency of this filter tracks the synchronous frequency (rotational speed), hence the name synchronous tracking filter. The tracking notch filter will eliminate all signals at the synchronous frequency from the control loop, including the measurement error ("mass unbalance"). In removing all signals at the synchronous frequency, however, closed-loop instability can result, limiting the usefulness of this approach.
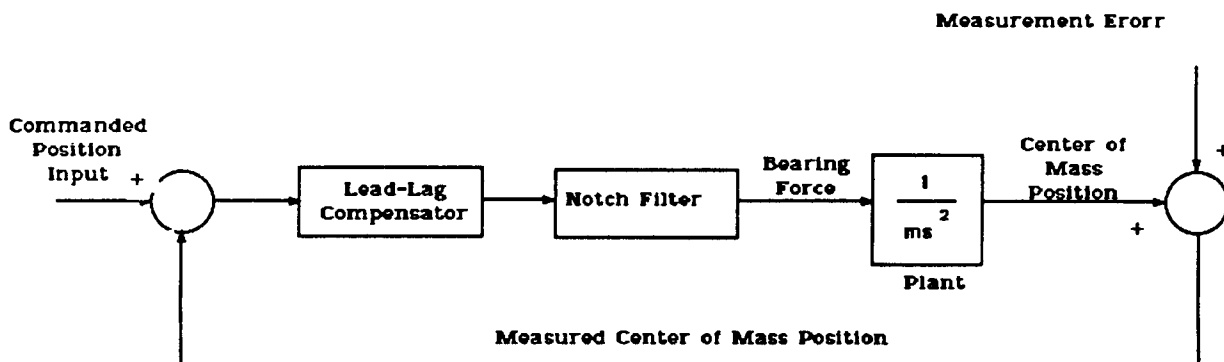
Figure 22. Notch Filter Block Diagram

65

The notch used in this investigation is a ideal two pole
transfer function with infinite notch depth. The notch transfer
function $N(s,\Omega)$ is a function of both frequency (Laplace variable
s) and rotational speed (Ω). It is given by

$$N(s,\Omega) \; = \; \frac{s^2 \; + \; \Omega^2}{s^2 \; + \; \Omega s/Q \; + \; \Omega^2} \qquad (48)$$

The steepness of the notch is determined by the parameter Q. A
larger Q makes a steeper notch[1].

Figure 23 is a Bode plot of the loop transfer function for a
subcritical rotational speed of 100 rad/sec and a notch Q of 10.
The dashed lines indicate zero gain and -180 degree phase. Note
that the phase of the loop transfer function is dramatically
different than without the notch. The negative phase that the
notch filter adds when the loop gain is greater than unity leads
to instability in this case. The Nyquist plot for this case is
shown in Figure 24. The complex coefficient transfer function[2]
encircles the -1 point twice, giving four closed-loop unstable
poles[3]. At higher rotational speeds, however, the phase loss

---

[1] The use of a more general finite depth notch filter has
been investigated by Beatty [1988].

[2] For a detailed development of the Nyquist criteria for
complex coefficient transfer functions (CCTF) see Johnson [1987a].

[3] The Nyquist plots shown in this report have been
modified for easier presentation. Outside of the unit circle,
which is shown by the dotted line, the log of the magnitude of
the transfer function has been added to one and used as the
magnitude on the Nyquist plots. This allows the large peaks to
be more clearly seen.

Loop Gain

(a)

Loop Phase
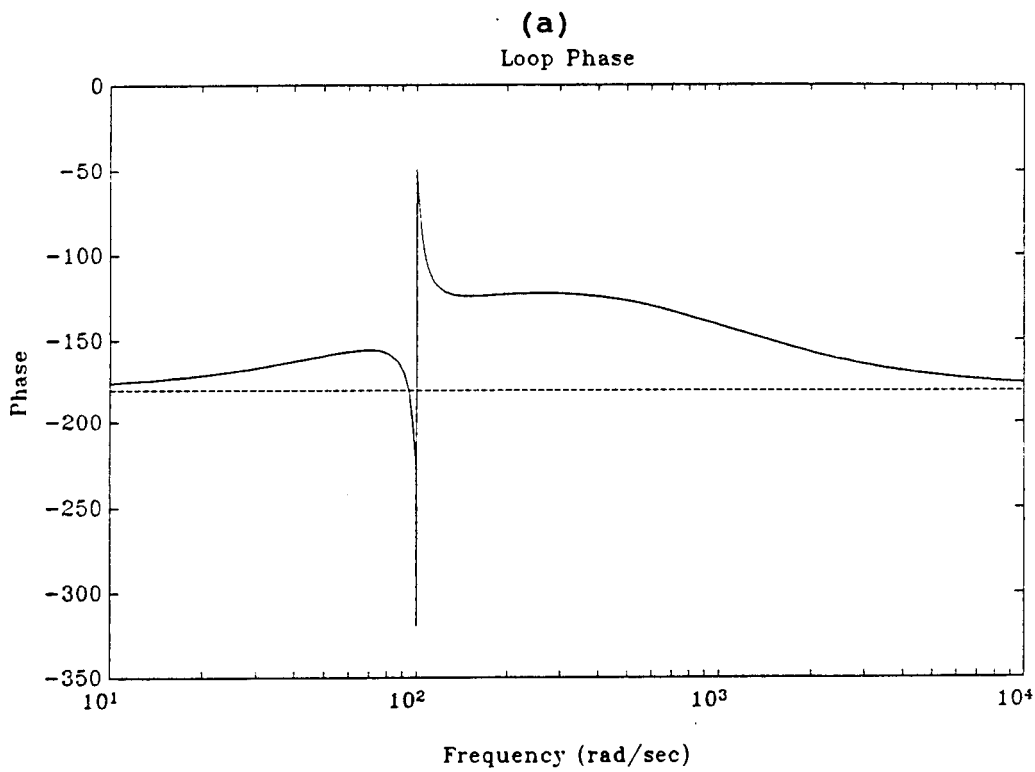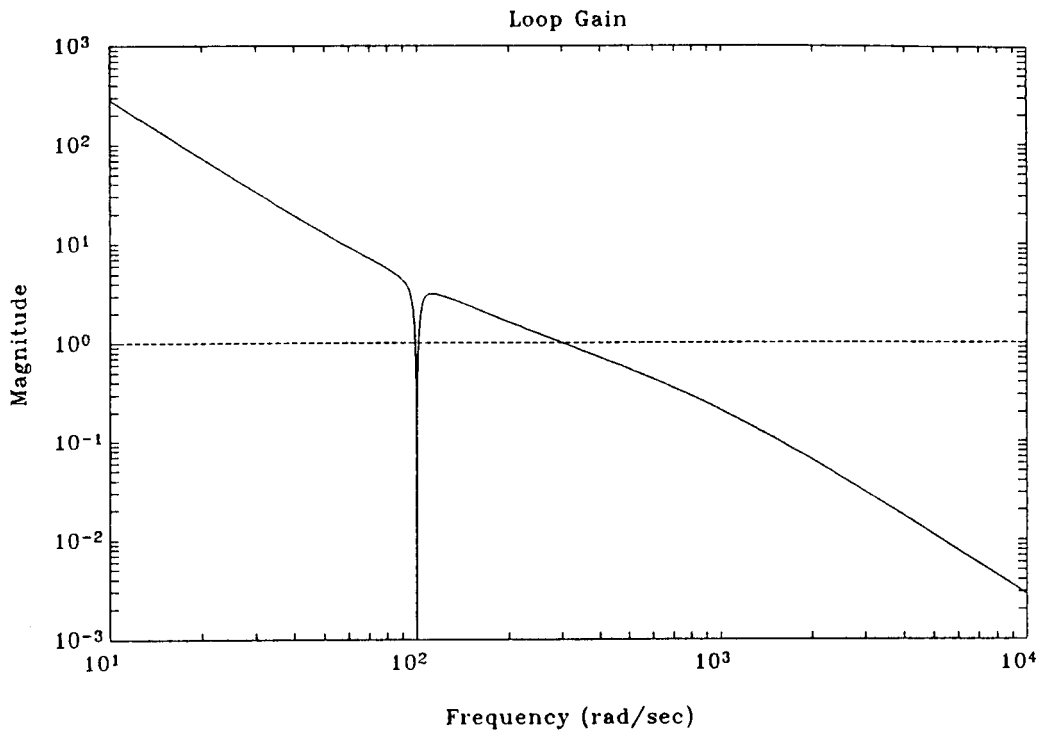
(b)

Figure 23. Notch Filter Loop Gain at Subcritical Speeds
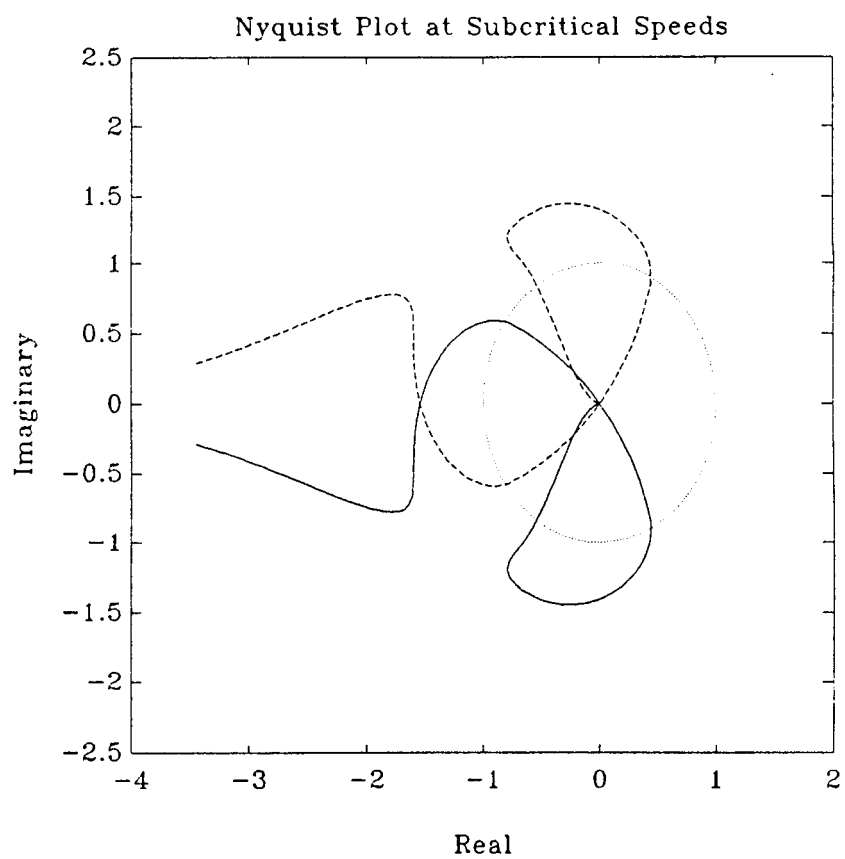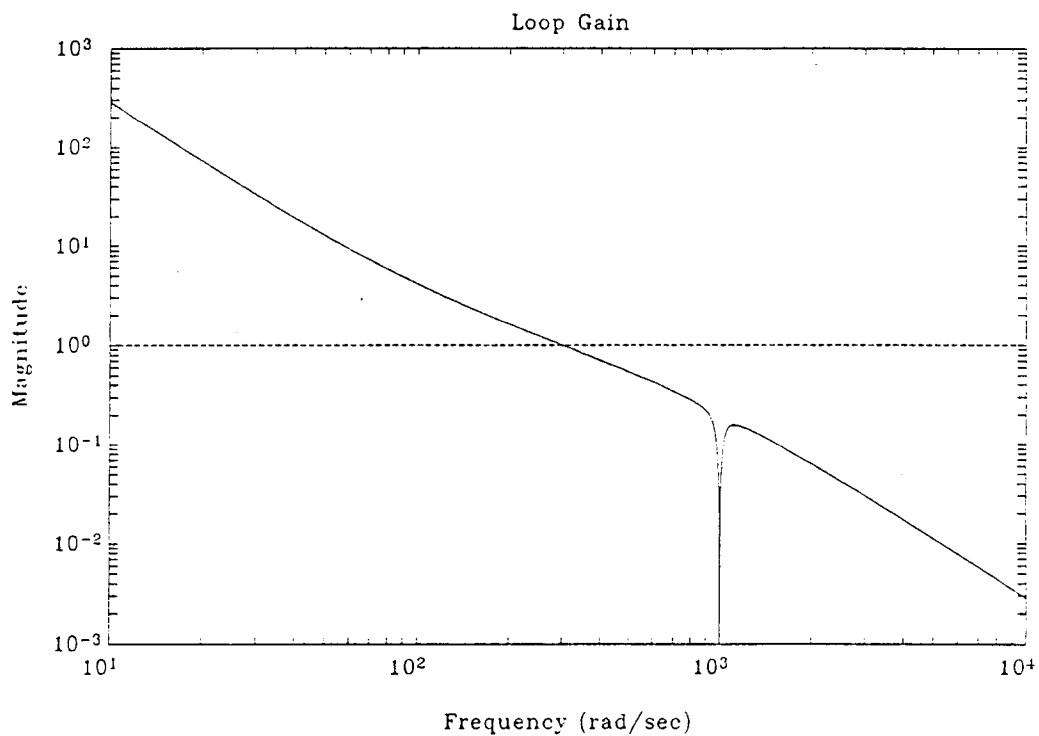
Nyquist Plot at Subcritical Speeds

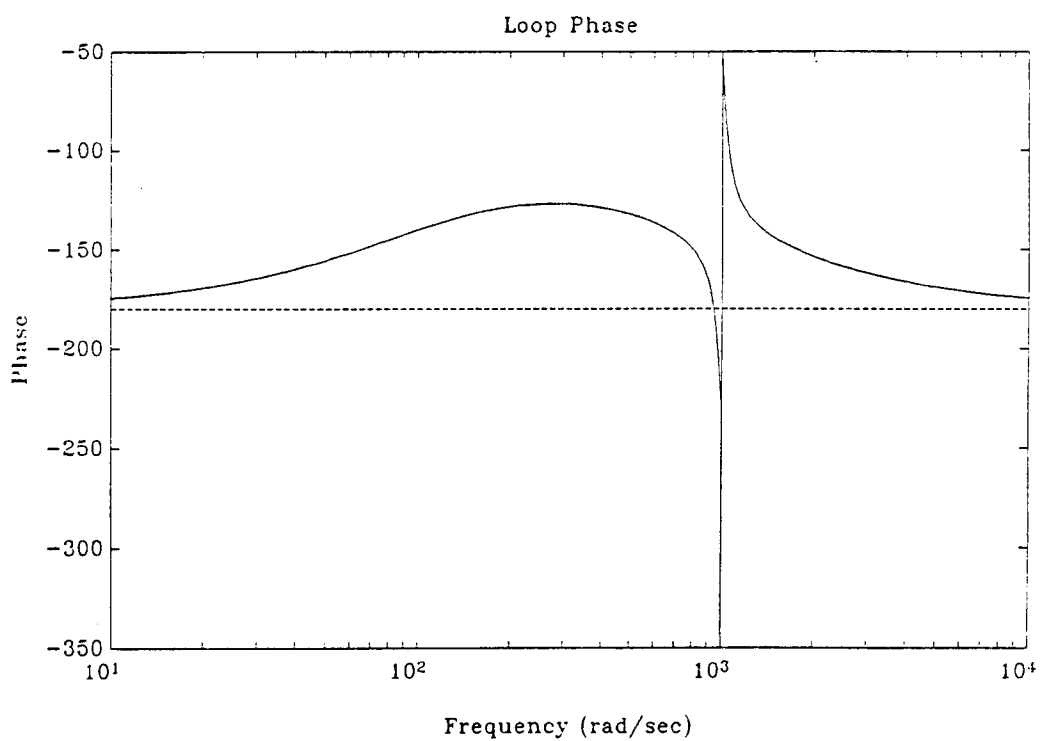**Figure 24. Notch Filter Nyquist Plot at Subcritical Speeds**

68

caused by the notch filter occurs at frequencies past cross-over and does not affect system stability. This can be seen in Figures 25 and 26, the Bode plot of the loop gain and the Nyquist plot. For these two graphs, the rotational speed is 1000 rad/sec, a supercritical speed, and the notch Q is 10 as before.

The stability results can be more easily seen in Figure 27. This is plot of closed-loop eigenvalue damping versus rotational speed for a notch Q of 10. The system is closed-loop unstable until a rotational speed of 150 rad/sec, approximately the cross-over frequency of the system. The effect of Q on stability can be seen in Figure 28, a plot of the rotational speed at zero closed-loop damping versus the Q of the notch. This rotational speed curve is a stability boundary, therefore, versus the notch Q. Note that the stability boundary is lowered for higher notch Q.

The performance results for the synchronous notch filter are summarized in Figure 29. Shown is the normalized attenuation of the measurement error at the synchronous frequency. This is analogous to the conventional synchronous response plots. The center of mass displacement is normalized by the measurement error distance ϵ_h (mass unbalance distance). The synchronous response of the tracking notch filter system is zero in its stable range of rotational speeds. For comparison, the synchronous response of the lead-lag compensator by itself is also shown. The important result is that the tracking notch filter can only be used at supercritical rotational speeds. In

69

Loop Gain

(a)

Loop Phase

(b)

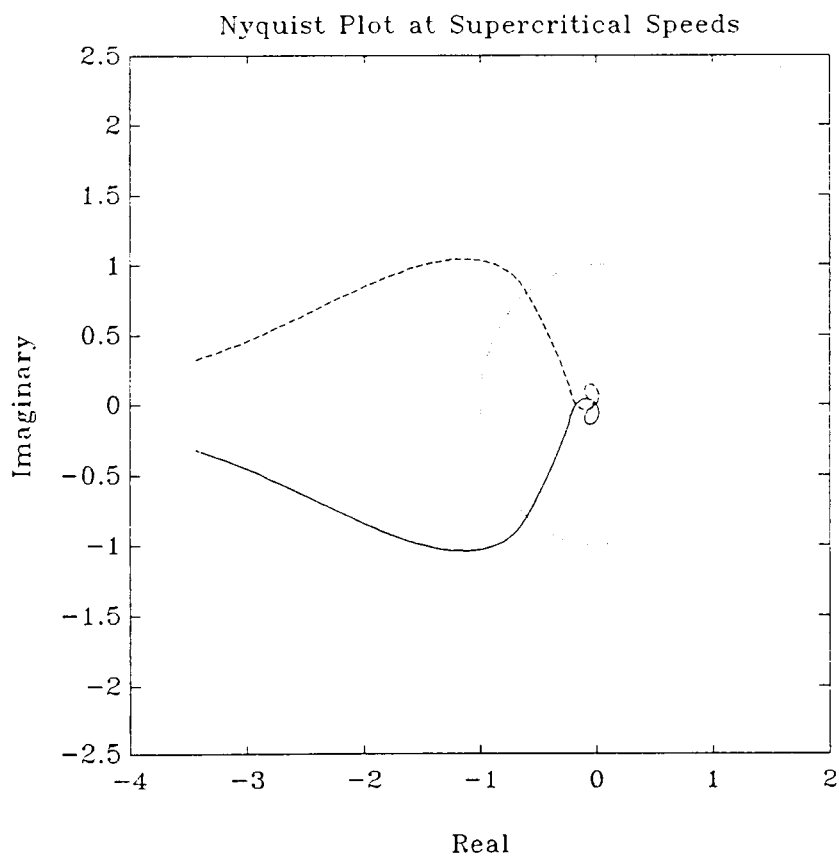**Figure 25.   Notch Filter Loop Gain at Supercritical Speeds**

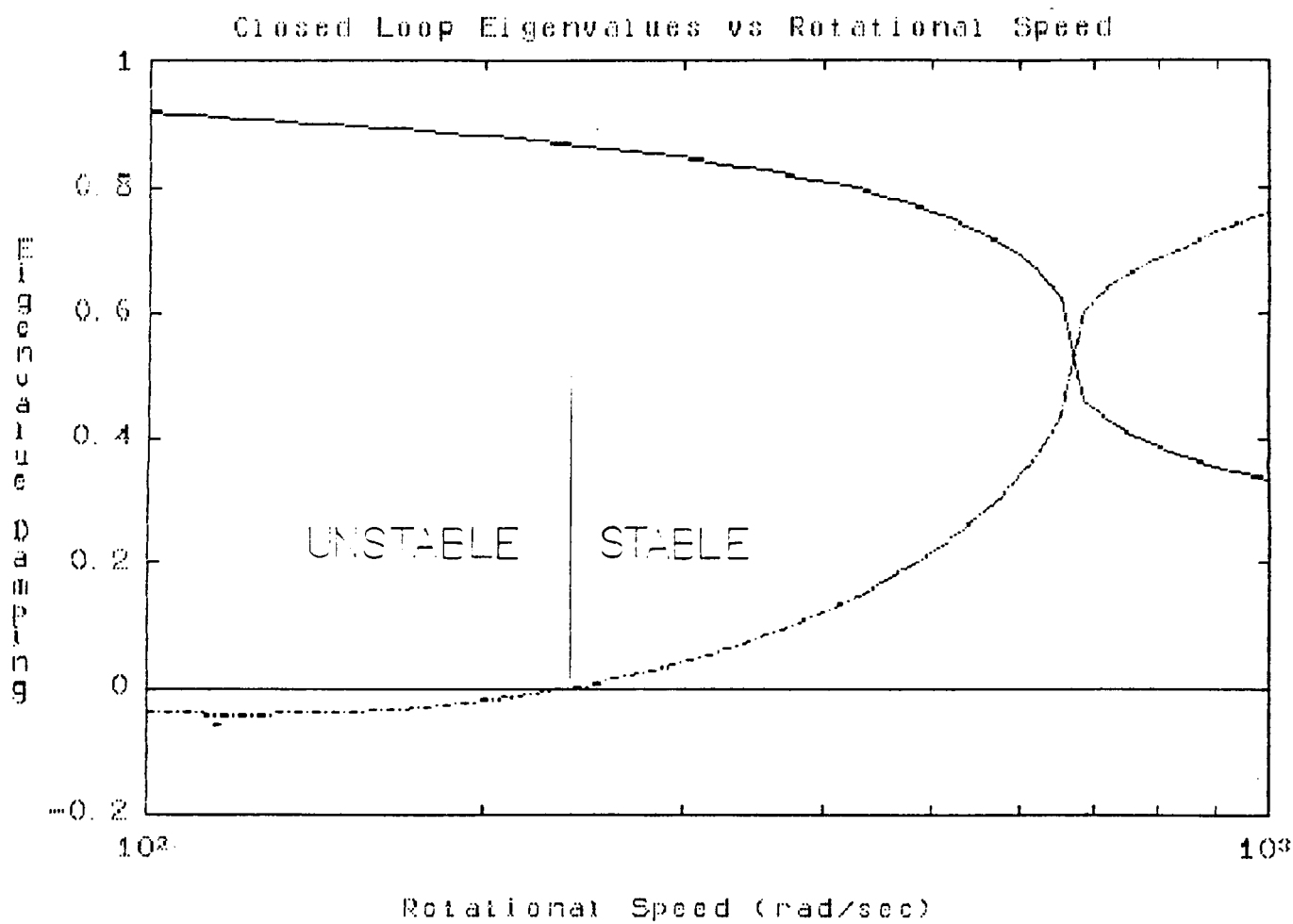Nyquist Plot at Supercritical Speeds

Figure 26. Notch Filter Nyquist Plot at Supercritical Speeds

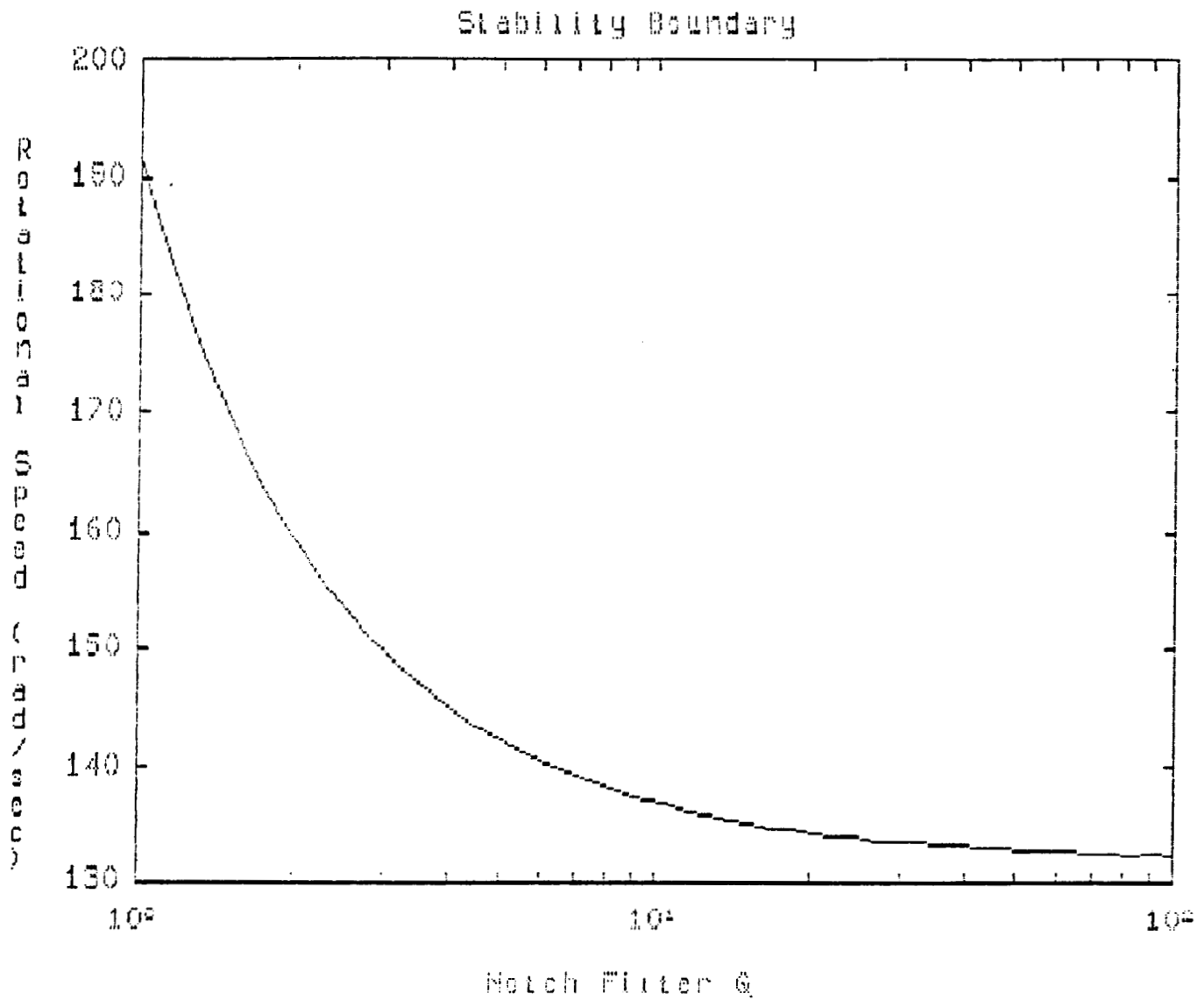Figure 27. Closed-loop Eigenvalue Damping versus
Rotational Speed

72

Figure 28. Rotational Speed at the Stability Boundary
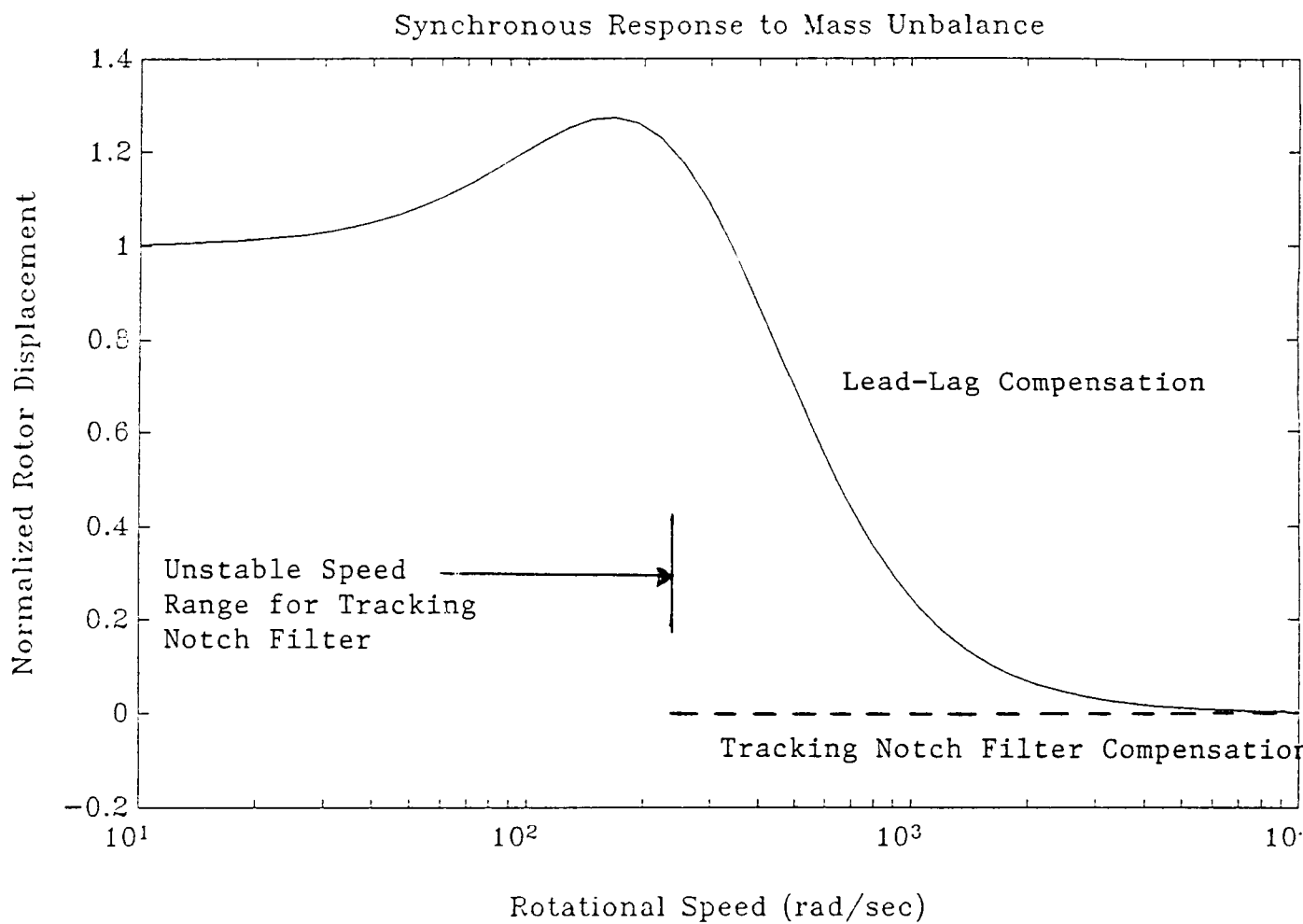versus Notch Q

Figure 29. Synchronous Performance versus Rotational Speed

this supercritical speed range the notch filter will perform better than the simple lead-lag compensator.

3.3 Lead-Lag Compensator with Tracking Differential-Notch Filter

As was shown in the last section, a tracking notch filter perfectly rejects the measurement error (mass unbalance) of a rigid-body rotor. It suffers, however, from a limited rotational speed range where it is stable. The tracking differential-notch filter developed under this contract retains the good synchronous response performance of the notch filter but with vastly improved stability properties.

The stability problems of the tracking notch filter arise because the notch filter, while eliminating the synchronous measurement error, eliminates any desirable control signals at the synchronous frequency. The tracking differential-notch filter alleviates this problem by re-injecting the desirable control signals into the feedback control loop. A block diagram of the system with the tracking differential-notch filter is shown in Figure 30. If the path through the plant model were eliminated, this system shown in Figure 30 would be the same as the tracking notch filter presented in the last section. Note, however, that the tracking notch filter has been implemented in a special way. The measured center of mass position of the rotor is notch filtered by subtracting from the signal a synchronous tracking bandpass filtered version of itself. This results in a synchronous tracking notch filter. The measurement error $\epsilon_h e^{j\Omega t}$ is therefore perfectly filtered from the feedback signal used to

75

ESTIMATED HUB CENTER OF MASS POSITION $\hat{Z}$
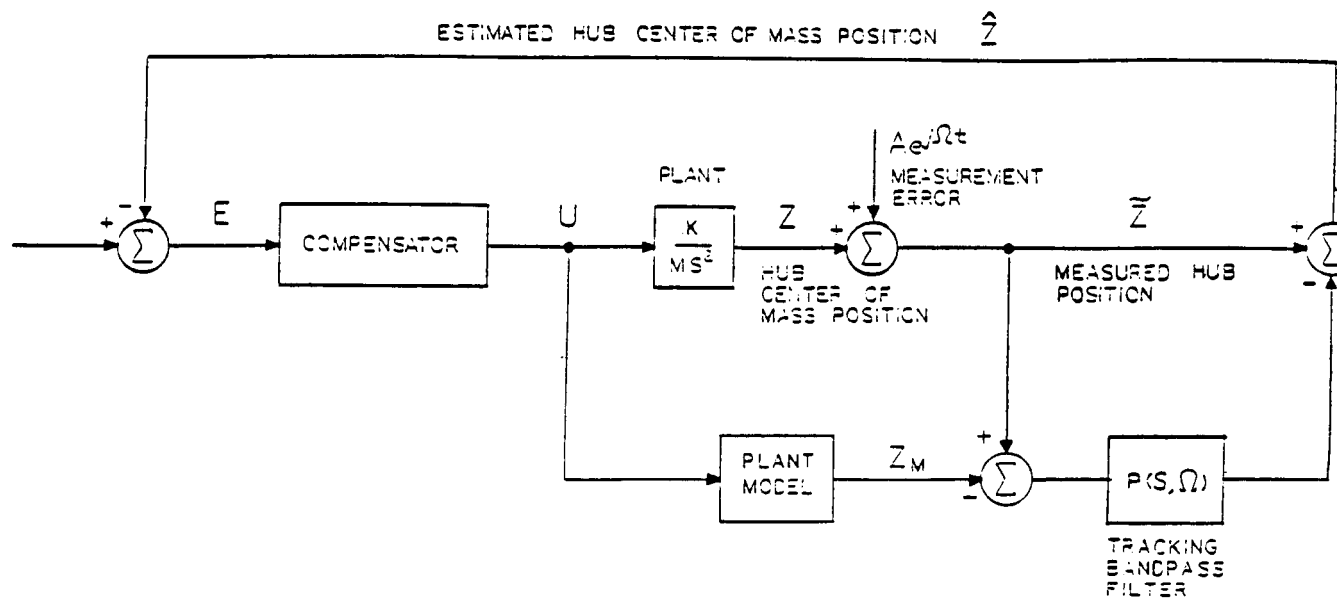
$$\hat{Z}(s) = Z(s) + (1 - P(s,\Omega))\cdot Ae^{j\Omega t} - P(s,\Omega)\cdot(Z(s) - Z_m(s))$$

$$\hat{Z}(s) = (1 - P(s,\Omega))\cdot Z(s) + P(s,\Omega)\cdot Z_m$$

NOTCHES THE MEASUREMENT ERROR (GOOD)

ALSO NOTCHES THE CENTER OF MASS POSITION Z(s)

ADD ESTIMATED CENTER OF MASS POSITION TO IMPROVE STABILITY

Figure 30. Tracking Differential-Notch Filter Block Diagram

drive the compensator. The output of the compensator, which is assumed to be a simple lead-lag as before, is used produce the input force driving the plant.

The difference between the tracking differential-notch filter of Figure 30 and the tracking notch filter of the previous section is the addition in Figure 30 of a feedforward path utilizing a model of the plant. The purpose of this loop is to re-inject the synchronous component of the plant input signal that is lost because of the notch filtering of the plant output. This component is formed by routing the input signal to the plant through the plant model followed by the synchronous bandbass filter. This route provides an estimate of the desirable synchronous component that has been eliminated by the notch filtering of the actual plant output.

The estimated hub center of mass position z(s) is given by

$$z(s) = z(s) + (1 - P(s,\Omega)) \cdot \epsilon_h e^{j\Omega t} - P(s,\Omega) \cdot (z(s) - z_m(s))$$

where   (49)

$z(s)$ = Estimated hub center of mass position

$z(s)$ = Hub center of mass position

$P(s,\Omega)$ = Tracking bandpass filter

ϵ_h = Measurement error distance (mass unbalance distance)

Ω = Rotational speed

$z_m(s)$ = Output of plant model (modelled hub center of mass position.

The bandpass filter $P(s,\Omega)$ is a function of the rotational speed Ω, with the passband tracking the rotational speed. The transfer

77

function of this synchronous tracking bandpass filter is

$$P(s, \Omega_f) = \frac{\dfrac{\Omega_f s}{Q}}{s^2 + \dfrac{\Omega_f s}{Q} + \Omega_f^2} \tag{50}$$

where, as before, Q is a parameter of the filter that determines the steepness of the passband. The parameter Ω_f is the center frequency of the passband. It is nominally set equal to the actual rotational speed Ω. Note that at the synchronous frequency Ω, the bandpass filter has unity gain if the synchronous frequency Ω is equal to the passband center frequency Ω_f.

The hub estimated center of mass position (Equation 49) can be rearranged to give

$$z(s) = (1 - P(s, \Omega)) \cdot z(s) + P(s, \Omega) \cdot z_m(s) \tag{51}$$

where the bandpass filter $P(s, \Omega)$ is assumed to have unity gain at the synchronous frequency Ω. The important result here is that the estimated hub center of mass position $z(s)$ is not a function of the measurement error. In other words, this system perfectly rejects the measurement error (mass unbalance). Furthermore, if the plant model perfectly models the plant, the estimated hub center of mass position is a perfect estimate of the actual hub center of mass position.

An obvious choice for the plant model is the same as the plant, with a transfer function

78

$$G(s) \quad \frac{1}{ms_2} \qquad\qquad (52)$$

This plant model, however, does not work because the resulting system is uncontrollable through the input u(s). This happens because the input u(s) sees two identical, parallel paths. Only one of these can be stabilized by the input. A relatively simple solution to this problem exists. The output of the plant model is only used at the synchronous frequency Ω. At lower frequencies, the plant model need not be an accurate representation of the plant. Therefore the plant model can be made open-loop stable with

$$G_m(s) \quad = \quad \frac{\frac{1}{m}}{s^2 + 2\varsigma\omega_0 s + \omega_0^2} \qquad\qquad (53)$$

where

$G_m(s)$ = plant model

m = plant mass

ω_0 = natural frequency of model

ς = model damping

The natural frequency of the model (ω_0) is chosen to be below the range for which synchronous response control is important. The model damping (ς) is chosen to give a well damped model. For the examples in this section, ω_0 is set to 5 rad/sec and ς to 0.707.

The Bode plot of the loop transfer function for this

79

controller, with the loop broken at the compensator input, is shown in Figure 31. For this case, the rotational speed Ω is 100 rad/sec, the filter Q is 10 and the crossover frequency (ω_c) of the system, as determined by the lead-lag compensator, is 300 rad/sec. Since the rotational speed is less than the crossover frequency, this is a subcritical speed. The loop transfer function for the tracking differential-notch filter (Figure 31) is essentially the same as for the simple lead-lag compensator (Figure 20). Importantly, the tracking differential-notch filter does not distort the loop gain as the simple notch filter does, as can be seen by comparing Figures 31 and 23.

The stability of the tracking differential-notch filter can be found from the Nyquist plot. Figure 32 is the Nyquist plot of the loop transfer function of Figure 31. The Nyquist plot does not encircle the minus one point and the system is stable, as expected. As can be seen in Figures 31 and 32, the tracking differential-notch filter retains the good stability properties of the simple lead-lag compensator on which it is based.

The tracking differential-notch filter, however, also has the good synchronous response characteristics of the tracking notch filter. This can be seen in Figure 32, a plot of closed-loop transfer function from measurement error to hub center of mass position for the same conditions as Figures 30 and 31. The important result is that the closed-loop gain at the synchronous frequency of 100 rad/sec is zero. This system, therefore, perfectly rejects the measurement error (mass unbalance). This
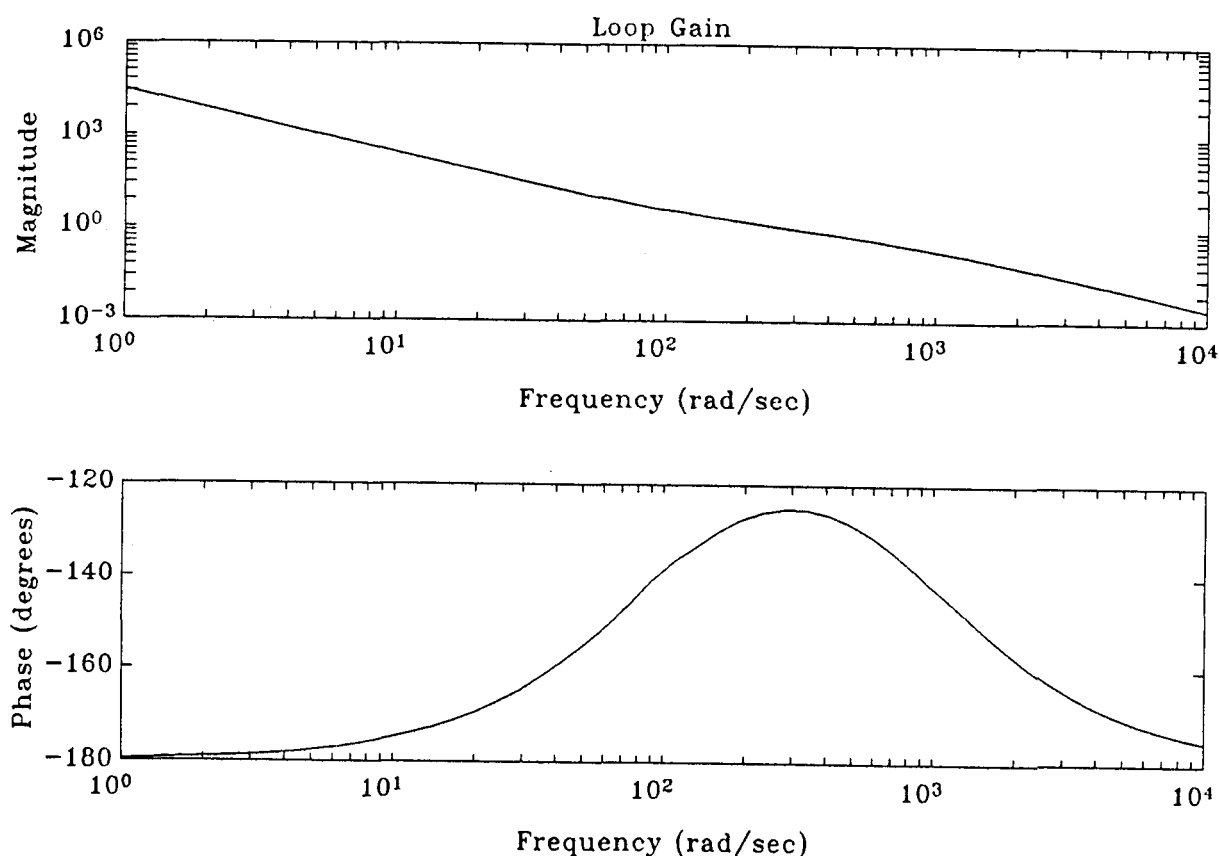
Figure 31. Tracking Differential-Notch Filter Loop Bode Plot

contrasts with the performance of the simple lead-lag compensator as can be seen in Figure 21.

The important result of this section is that the tracking differential-notch filter nominally provides perfect rejection of the measurement error (mass unbalance) with the good stability properties of the simple lead-lag compensator. Because the measurement error is rejected, the rotor spins about its center of mass at all speeds above the natural frequency of the plant model, which can be made arbitrarily small. Since the rotor

Stable Nyquist Plot (Rotational Speed = 100 rad/sec)
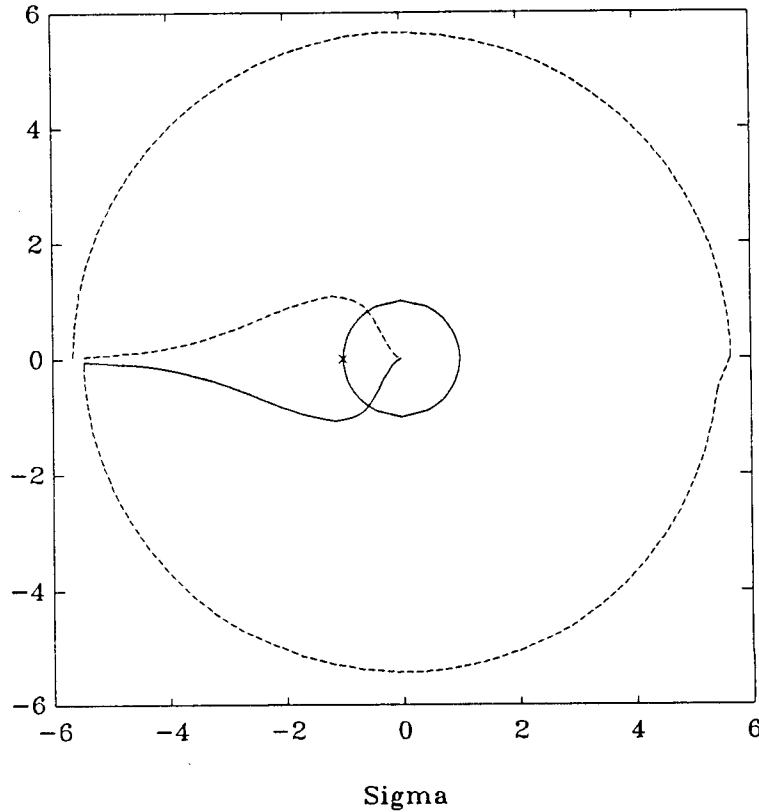
Figure 32. Nyquist Plot of the Tracking Differential-Notch
Filter

spins about its center of mass, no synchronous forces are
produced by the measurement error (mass unbalance). This means
that the rotor spins as if it were perfectly balanced, for
subcritical, critical, and supercritical speed ranges.

The remainder of this section will examine the performance
of the tracking differential-notch filter in the presence of
modelling and filtering errors as well as practical methods to
implement the proposed controller.

An important potential error source is mismatching of the
actual rotational speed from the bandpass center frequency. If

these frequencies are mismatched, the measurement error signal will not be totally notched out of the estimated hub center of mass position. Figure 33 is a plot of closed-loop synchronous response versus bandpass Q for various levels of frequency mismatching. Shown is the closed-loop synchronous response of the center of mass position normalized by the mass unbalance distance ϵ_h. The measurement error is perfectly rejected when the normalized center of mass position is zero. The curves, from top to bottom, are for frequency mismatches of 1%, 0.5%, 0.1%, and 0.05% between the passband center frequency Ω_f and the actual rotational speed Ω. The curves in Figure 33 are for the same parameter values ($\omega_0 = 5$ rad/sec, $\zeta - 0.707$, $\Omega = 100$ rad/sec) as in Figures 30 through 32. As can be seen in Figure 33, the synchronous response performance is more robust to frequency mismatching if the Q of the bandpass filter is lower. A lower Q results in a wider notch filter. On the other hand, decreasing the Q of the filter reduces the stability margin and command following performance of the system. This can be seen in Figure 34, a plot of phase margin versus modelling error for various values of Q. The vertical axis is the phase margin, and the horizontal axis is modelling error (error between mass used in model and actual rotor mass). As can be seen, low values of Q have smaller phase margins. There is a tradeoff, therefore, between robustness to frequency mismatching and robustness to modelling error.
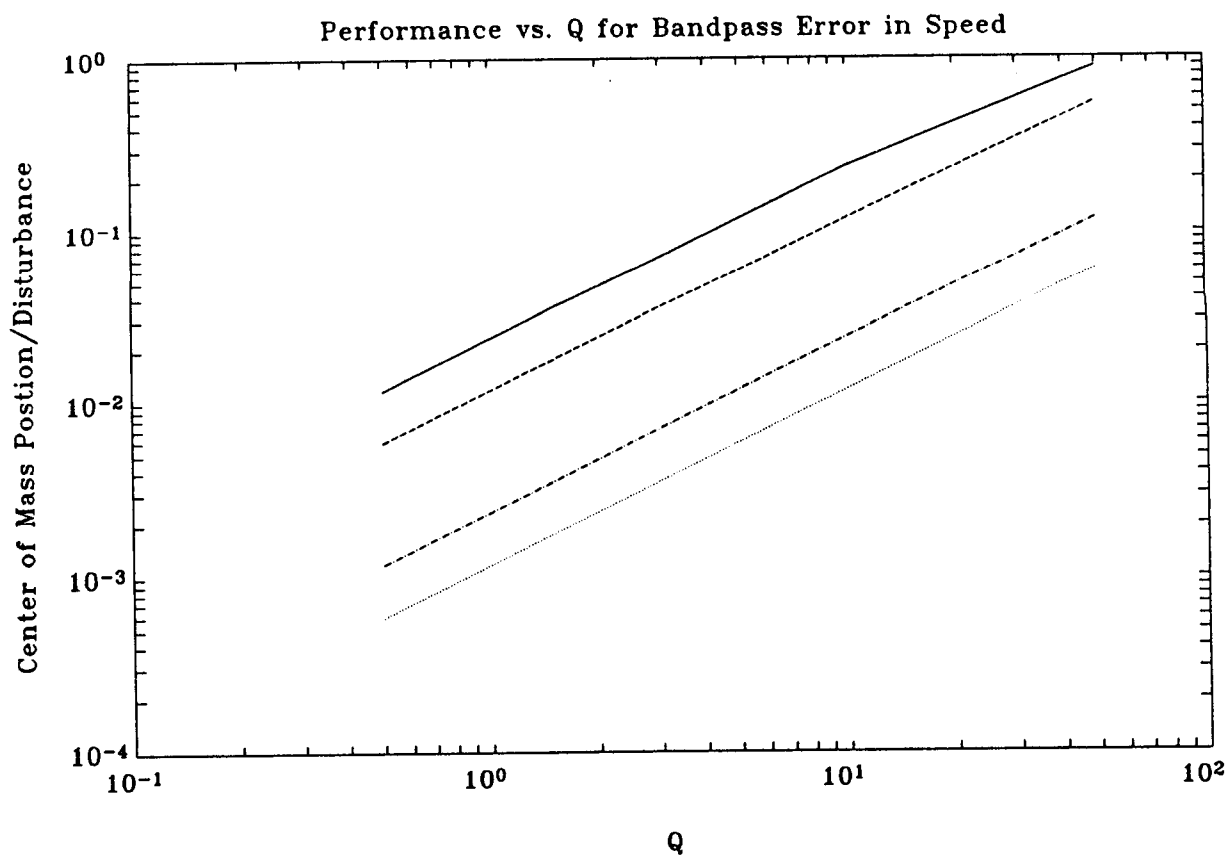
Performance vs. Q for Bandpass Error in Speed

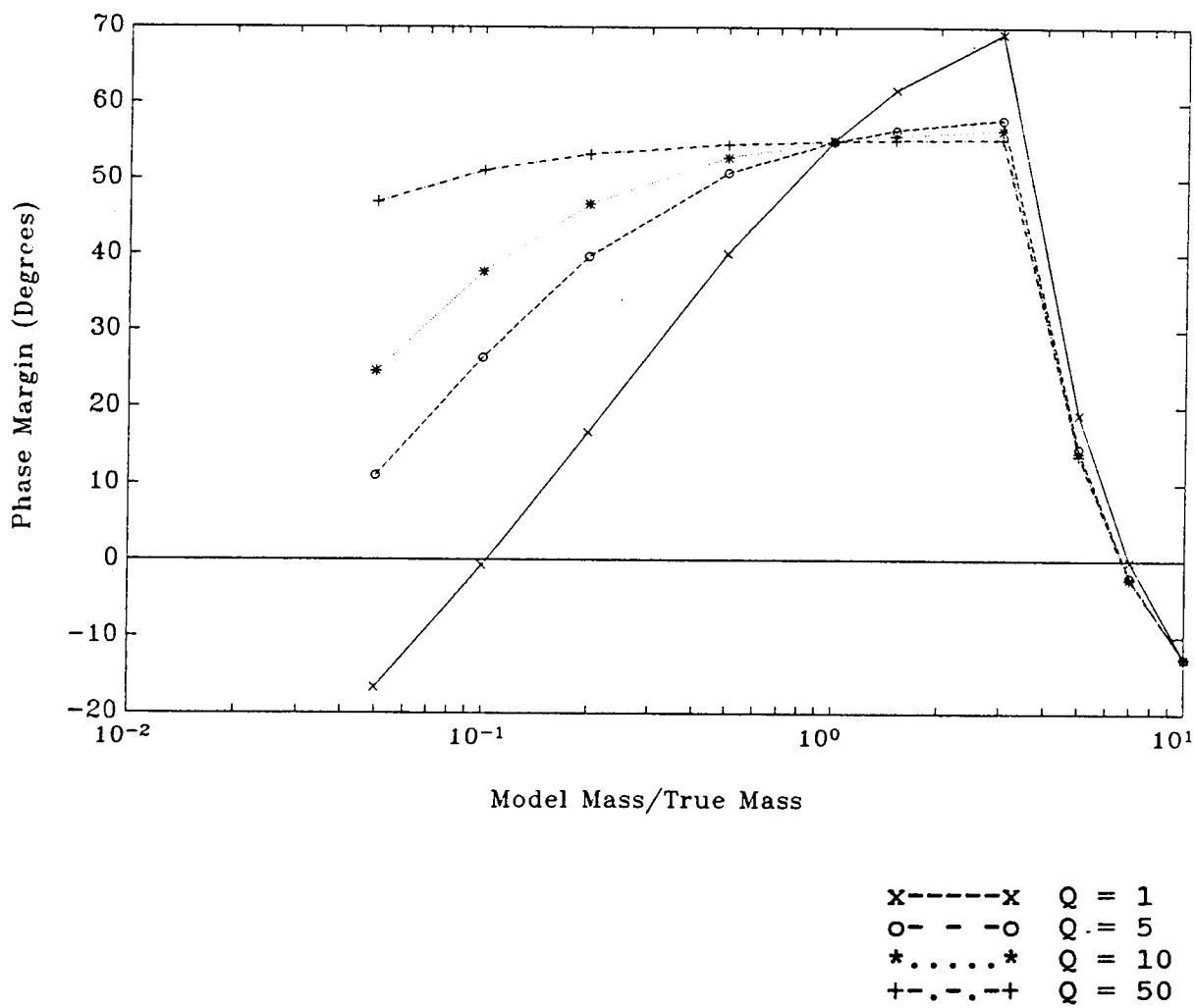Figure 33. Closed-loop Measurement Error Transfer Function

Figure 34.   Phase Margin versus Modelling Error

The remainder of this section will discuss implementation of the tracking differential-notch filter. A block diagram of the proposed implementation is shown in Figure 35. The top of the diagram contains the lead-lag compensator and the plant, which consists of the double integration of input force to hub center of mass position and the additive measurement error. The bottom part of the diagram shows the implementation of the plant model and tracking bandpass filter. There are three inputs to this part of the system; the output of the compensator, the measured hub position, and the output of a tachometer. The output is the estimated measurement error.

The tracking bandpass filter works by heterodyning the input signals by the synchronous frequency, reducing the synchronous frequency to baseband. This is done by the multipliers labelled A and B. These signals are then lowpass filtered ($L(s)$) to achieve a bandpass filter when the baseband signals are heterodyned back to synchronous frequency. This is done by the multiplier labelled C. The choice of cutoff frequency in the lowpass filter $L(s)$ determines the Q of the resulting notch filter. The synchronous frequency sinusoid ($\cos(\Omega t)$) used in the multipliers is supplied by a phase locked loop that has as its primary input the measured hub position. The output of a tachometer can also be used to help stabilize the phase locked loop.

The plant model is implemented as a scheduled gain in the baseband frequency. When heterodyned back to synchronous
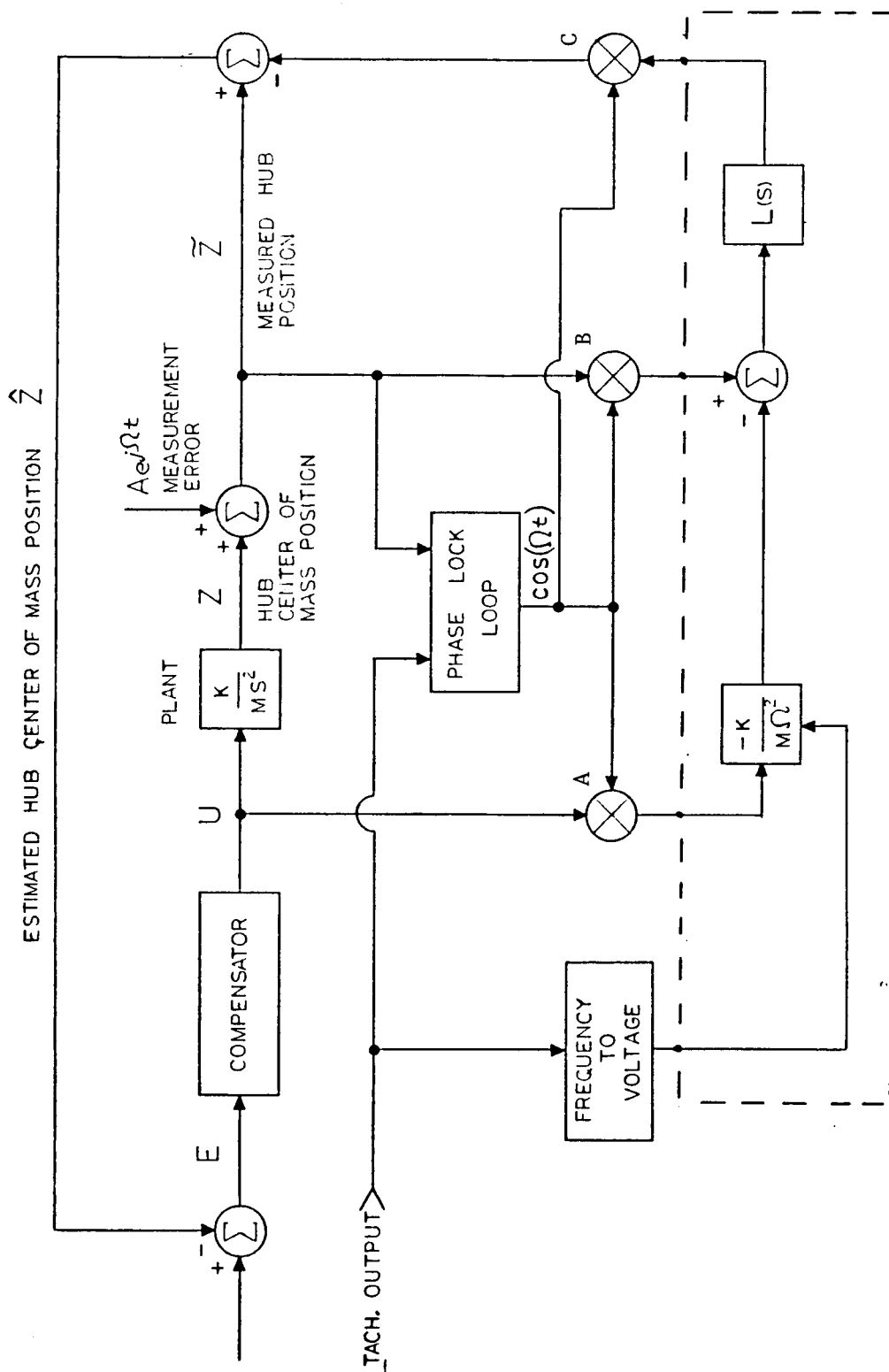
Figure 35 Scheduled Gain, Tracking Differential-Notch Filter

frequency, this yields the desired frequency domain plant model. The scheduled gain needed to model the plant is $m^{-1}\Omega^{-2}$, where Ω is the rotational speed. The rotational speed signal necessary to implement this is obtained from the tachometer through a frequency to voltage converter. The scheduled gain and the lowpass filter $L(s)$ can be implemented with low bandwidth digital hardware. This portion of the controller, labelled digital in Figure 35, requires only low bandwidth because the processing is being done at baseband frequencies.

Also shown in Figure 35 are three antialiasing filters $F_1(s)$, $F_2(s)$, and $F_3(s)$. These filters, as well as the three multipliers, would most likely be analog implementations. The two input filters $F_1(s)$ and $F_2(s)$ are highpass filters. The output filter $F_3(s)$ is a lowpass filter.

The performance of this system can be seen in Figures 36 and 37. These are frequency response plots of the plant, plant model, and tracking bandpass filter. Since this is a nonlinear system, these plots must be given careful interpretation. Shown is the normalized root mean square (rms) spectral response of the estimated hub center of mass position (the output z) to a white noise input (u) to the plant and tracking differential-notch filter. The response has been normalized by the rms magnitude of the white noise input and plotted in db. The abscissa is the frequency normalized by the rotational speed Ω. If this were a linear system, these plots would simply be the transfer function between input and output. The ideal plot is one with slope of -2

passing through the (0db, $\omega/\Omega = 1$) point.

Figures 36 and 37 both show four curves for different lowpass filter cutoff frequencies ω_n. These lowpass filter cutoff frequencies are normalized by the rotational speed such that $\omega_n = k \cdot \Omega$, where k = 10, 1, 0.1, and 0.01. Note that for high cutoff frequencies (k = 10 and 1) the response show significant aliasing at twice the synchronous frequency, as can be seen in Figure 36. From this figure the lowpass cutoff frequency $\omega_n = 0.01 \cdot \Omega$ is seen to give the best performance. Figure 37 shows the same curves in more detail near the synchronous frequency. Also shown is the heavy curve indicating the "ideal" response. Again, the k = 0.01 curve is seen to be the best. Note also that its maximum gain error is less 0.25 db.

In summary, the tracking differential notch filter (TDNF) developed in this section has been shown to provide the good stability of a simple lead-lag compensator combined with the good synchronous response performance gained by the addition of a notch filter. In addition, a relatively simple implementation has been developed comprised mainly of chip-level subcomponents and a low bandwidth digital section.

3.4 Model Based Compensators

The fourth class of control algorithms that was investigated under this program is the model based compensators (MBC). These output feedback compensators combine full-state-feedback, linear-quadratic regulators with state estimators. These MBCs were developed during the previous NASA sponsored research that
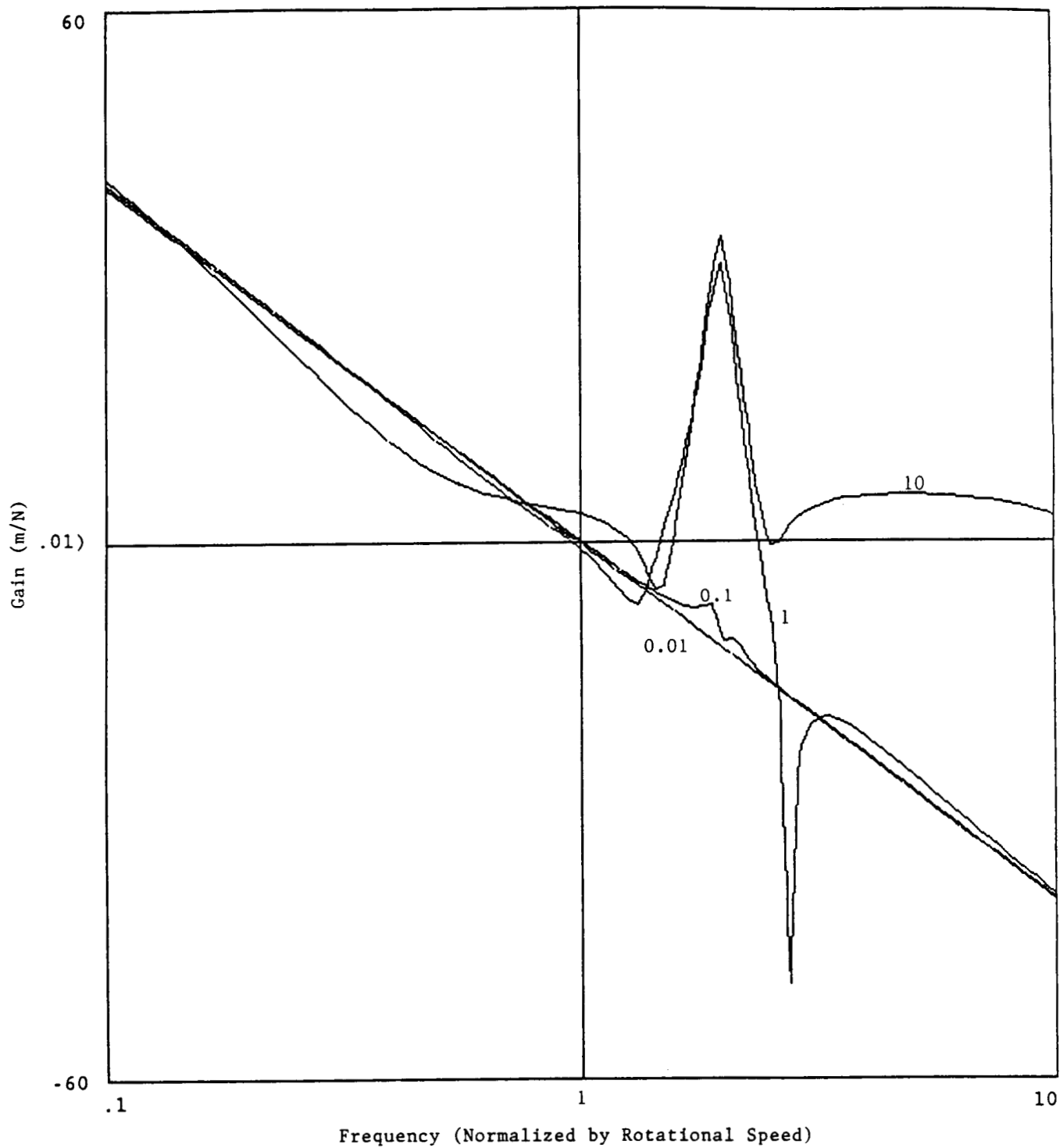
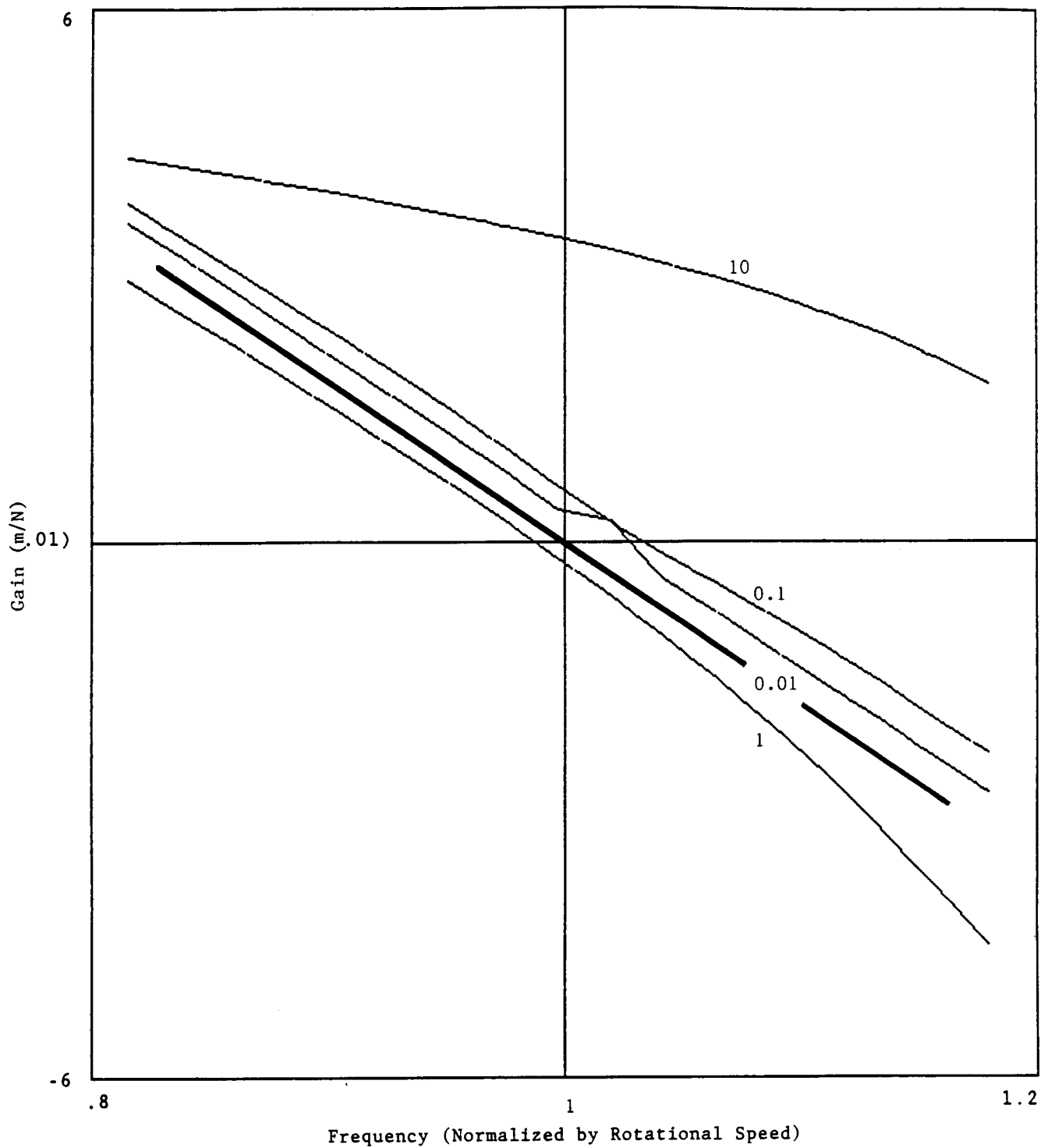**Figure 36. Frequency Response of TDNF Implementation**

Figure 37. Frequency Response of TDNF Implementation Near Synchronous Frequency

91

C-2

investigated stabilizing control algorithms for ACCESS. These compensators are designed using linear quadratic Gaussian synthesis with loop transfer recovery (LQG/LTR).

The MBC designed using the LQG/LTR procedure consists of a Kalman filter combined with a linear quadratic regulator. The Kalman filter is used as a full-state observer to estimate the state of the system. This estimated state is used by the LQR to produce the controller output. This configuration is shown in Figure 38. The transfer function of the model based compensator is given by $K_{mbc}(s)$ and of the plant by $G_p(s)$. The system output $\underline{Y}(s)$ is comprised of the plant output corrupted by the spoke disturbance $\underline{D}^i(s)$. For the rigid-body model under consideration in this chapter, the spoke disturbance $\underline{D}_i(s)$ is zero. The compensator has as its input the system output corrupted by the measurement error $\underline{D}_o(s)$.

The internal structure of the model based compensator and plant are shown in Figure 39. As can be seen in this figure, the compensator structure mimics the plant structure, hence the name "model based compensator." The **A**, **B**, and **C** matrices of the compensator are all determined by the plant model. The matrix K comes from the solution to the LQR problem. The Kalman filter matrix **H** formally comes from the solution of the steady state Kalman filter problem.
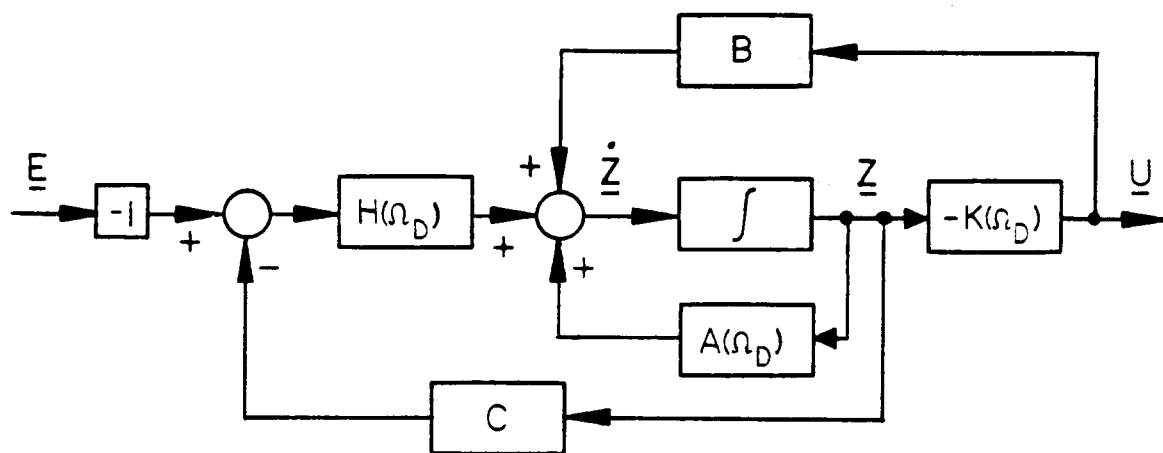
This control approach was developed in detail for this application during the previous NASA research program. Details of its derivation and rational can be found in Johnson [1987b].
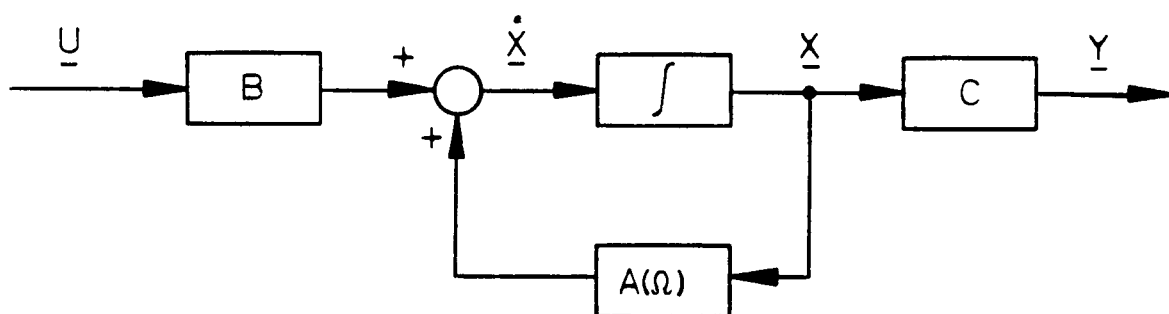
SPOKE
MISALIGNMENT
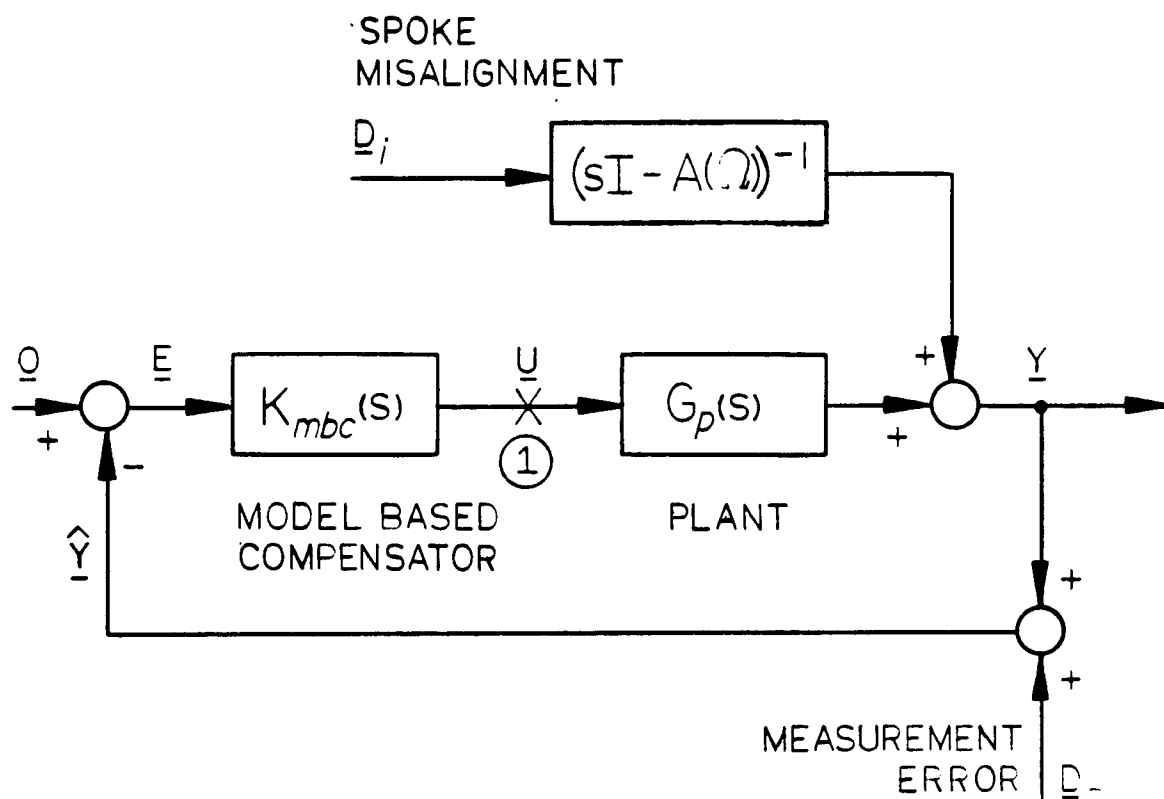
$$K_{mbc}(S) \text{ — A FUNCTION OF THE DESIGN ROTATIONAL SPEED } \Omega_D$$

$$G_p(S) \text{ — A FUNCTION OF THE ACTUAL ROTATIONAL SPEED } \Omega$$

Figure 38. Model Based Compensator Loop Configuration

93

a)   Model based compensator $K_{mbc}(s)$

b)   Plant

Figure 39.   Block Diagram of Model Based Compensator and Plant

For the rigid-body model under consideration in this chapter, the application of the LQG/LTR technique results in simple lead-lag compensator. The synchronous response of the MBC used to control the simple rigid-body model are the same, therefore, as the lead-lag results presented earlier in Section 3.1. For the flexible models used in the next chapter, however, the LQG/LTR approach will result in MBCs that are different from the lead-lag compensators.

4. SYNCHRONOUS RESPONSE CONTROL OF ACCESS

This chapter examines the performance of the four control approaches introduced in the last chapter used to control the flexible model of ACCESS. Again, the four approaches are:

(1) Mimic conventional bearings with lead-lag compensators

(2) Tracking notch filters

(3) Tracking differential-notch filters

(4) Model based compensators.

For the rigid-body rotor used in the last chapter, the synchronous response was caused by measurement error of the center of mass position. For the flexible rotor, a variety of synchronous response mechanisms are possible. In this chapter, the synchronous response of the closed-loop system will be illuminated by examining two specific misalignment configurations, one forcing the plant and the other forcing the controller.

Recalling the modelling presentation of Chapter 2, the synchronous disturbances are modelled as misalignments of the centers of mass, centers of spoke force, and center of measurement. The first specific disturbance that will be examined is caused by misalignment of the flywheel elastic center (center of spoke force) and flywheel mass center. As shown in Figure 40(a), the hub elastic, mass, and measurement centers are all assumed to coincide. The flywheel elastic center, however, is assumed offset from its mass center. This situation, which will be called "spoke misalignment" or "input error", could be achieved if an additional unbalance mass was added to the
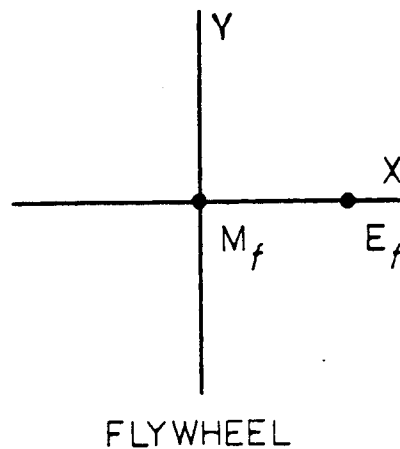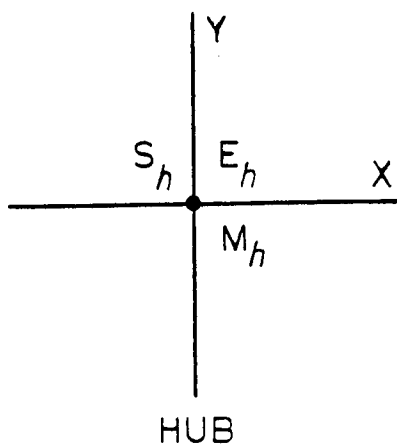
a) Spoke misalignment
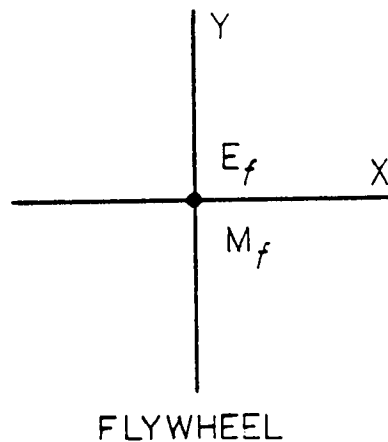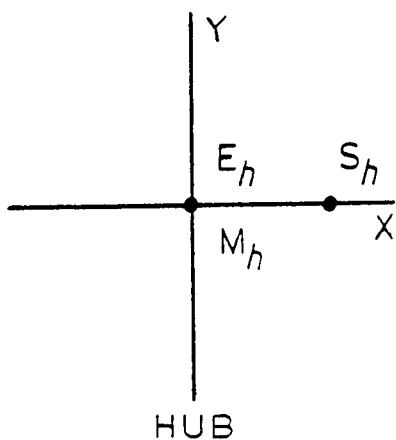
b) Measurement error

M_h -- Hub center of mass
E_h -- Hub elastic center
S_h -- Hub measurement center
M_f -- Flywheel center of mass
E_f -- Flywheel elastic center

Figure 40. Translational Misalignment (Disturbance) Configurations

flywheel of an otherwise geometrically perfect rotor. The geometrically perfect rotor consists of a perfectly balanced rotor (elastic and mass centers of the hub and flywheel coincide) with a perfect measurement system (measures perfectly the position of the center of mass of the hub).

The other specific disturbance that will be examined is an output disturbance caused by a misalignment of the hub measurement center and will be called "measurement error" or "output error". The rotor is otherwise perfectly balanced with coincident hub elastic and mass centers and coincident flywheel elastic and mass centers. This configuration is shown in Figure 40(b). This configuration would arise if the measurement system measured the position of some other point in the hub, besides the hub center of mass, of a perfectly balanced rotor.

The closed-loop synchronous response of the four control approaches to these two synchronous disturbances, spoke misalignment and measurement error, will be developed in the following sections.

4.1 Lead-Lag Compensation

Lead-Lag Synchronous Response to Measurement Error

The synchronous response to measurement error is shown in Figures 41 through 43. Figure 41 is a plot of the normalized hub center of mass (solid curve) and flywheel center of mass (dashed curve) synchronous whirl amplitudes (Figure 41(a)) and phases (Figure 41(b)). Two critical speeds can be seen. The critical speeds associated with the flexible-mode transmission zero at 497
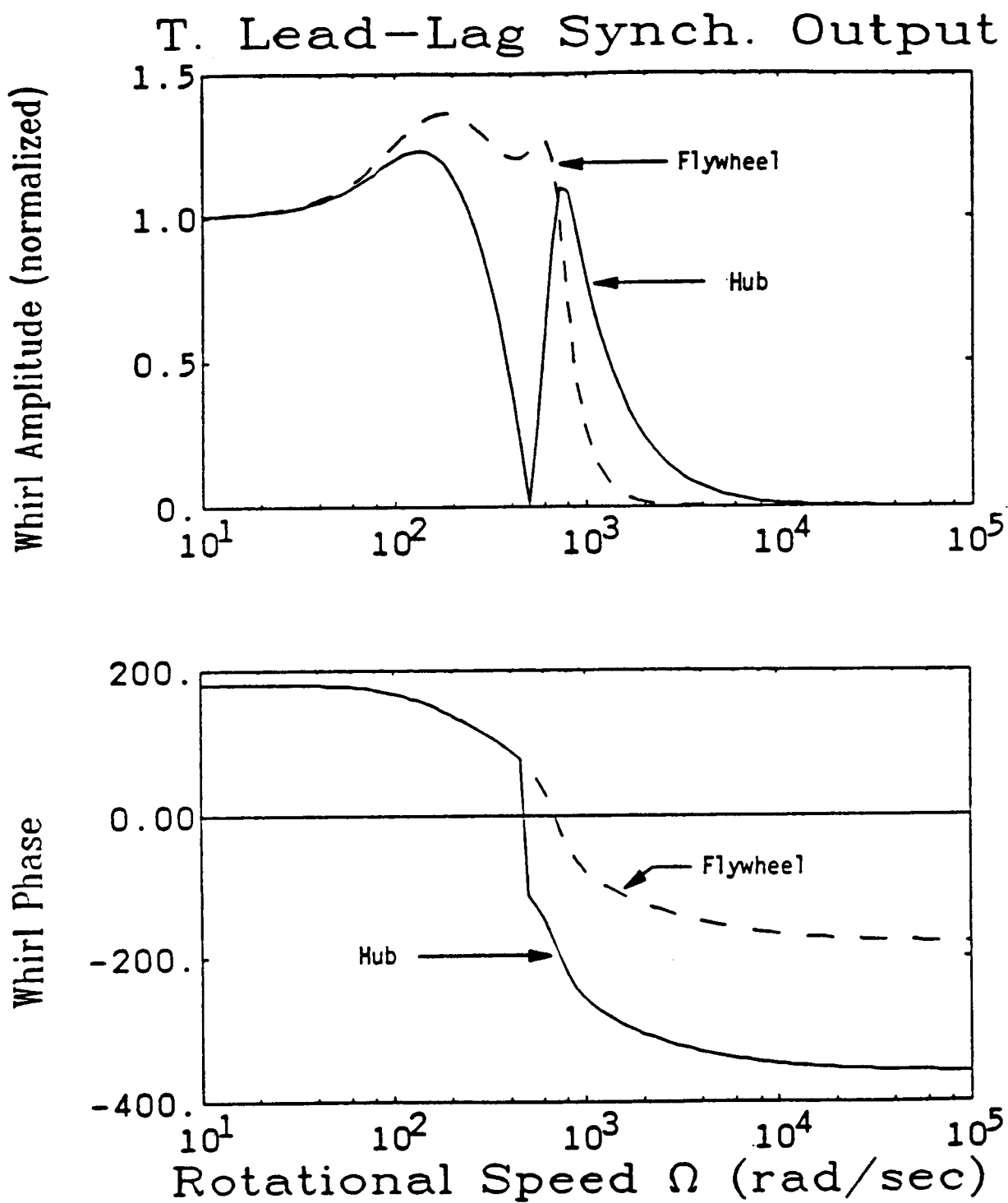
98

T. Lead-Lag Synch. Output

Figure 41. Synchronous Whirls caused by Measurement Error:
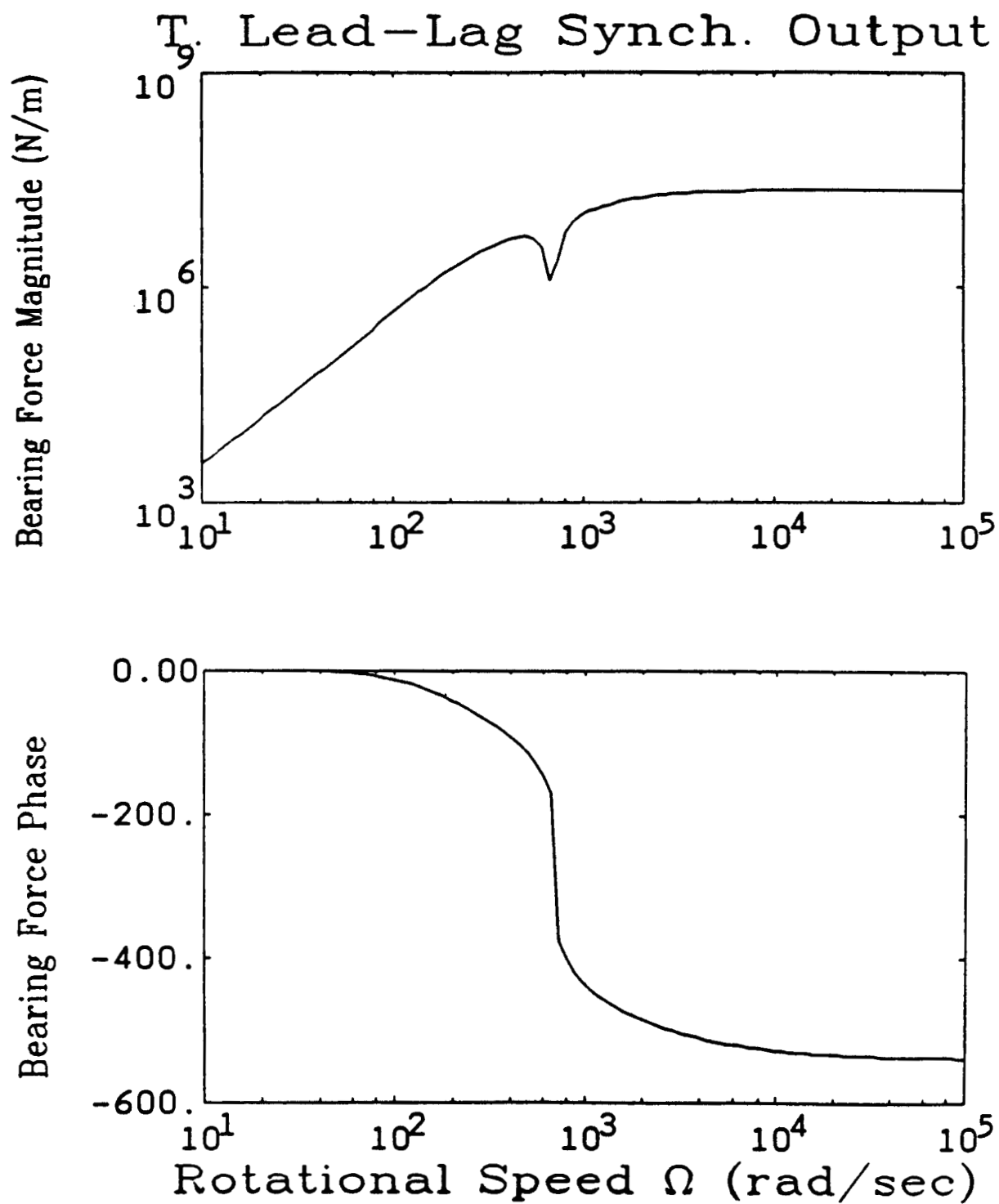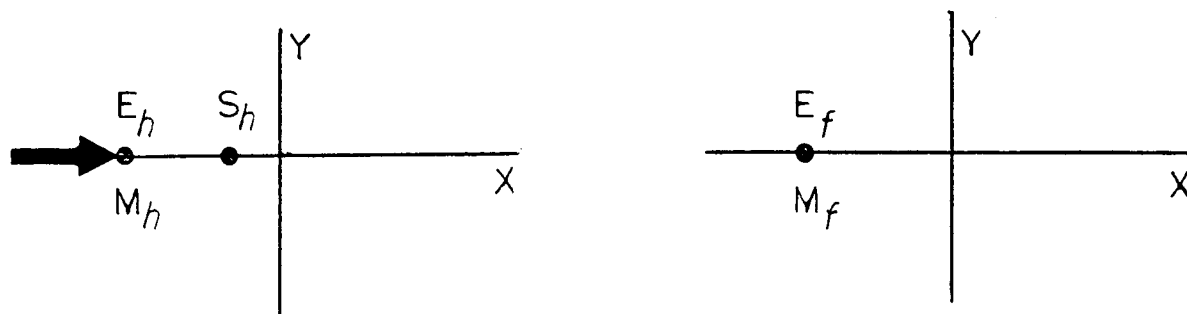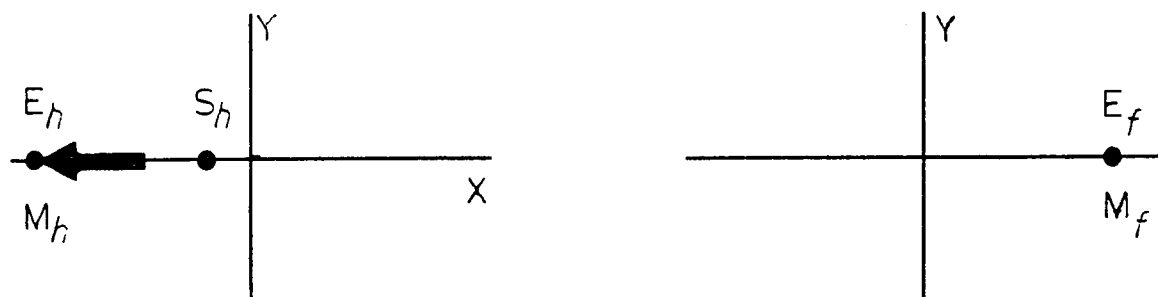Translational Medium-Bandwidth Lead-lag Compensator

Figure 42. Synchronous Bearing Force Caused by Measurement Error: Translational Medium-Bandwidth Lead-lag Compensator

a) Sub-critical

b) Critical

Hub   c) Super-critical   Flywheel

BEARING FORCE

Figure 43. Orientation of Flywheel and Hub during
            Synchronous Whirl caused by Measurement Error:
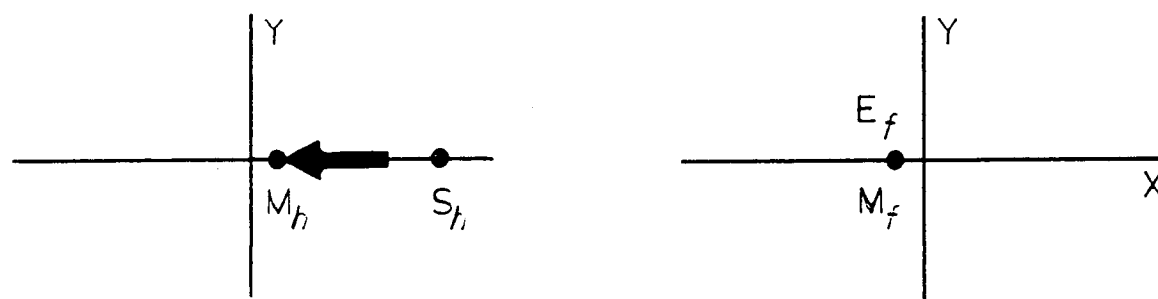   Translational Medium-Bandwidth Lead-lag
            Compensator

101

rad/sec and eigenvalue at 680 rad/sec are seen in this example to exhibit only moderate whirl amplitudes of the hub and flywheel centers of mass. The largest amplitude whirls are found near the cross-over frequency of the system, approximately 200 rad/sec. Even these maximum whirl amplitudes are small, however.

Figure 42 shows the synchronous bearing force caused by this measurement error. Figure 42(a) shows the magnitude of the bearing force and Figure 42(b) the direction at which the bearing force acts on the hub. The magnitude of the bearing force is normalized by the spoke misalignment distance and has units of Newtons per meter of spoke misalignment. The synchronous bearing force remains large at high speeds. This is due to the high-frequency roll-off of -2 for this lead-lag compensator. The high-frequency synchronous bearing force could be reduced by the addition of more poles in the compensator.

The orientations of the various hub centers, flywheel centers, and bearing force are given by the phase plots of Figure 41(b) and 42(b). These can be more easily interpreted by plotting in the radial plane the relative locations of the hub centers and flywheel centers and relative direction of the bearing force. This is done for sub-critical, critical, and super-critical rotational speeds in Figure 43. The locations of the hub and flywheel centers of mass are given by M_h and M_f and the locations of the elastic centers by E_h and E_f. The location of the hub center of measurement is given by S_h.

At sub-critical speeds, the rotor spins about the

measurement center S_h as shown in Figure 43(a). At these low speeds, both centers of mass exhibit normalized unit magnitude whirls. At the flexible-mode resonant frequency of 680 rad/sec, the hub and flywheel centers of mass both have approximately unity magnitude and are 180 degrees out of phase, as shown in Figure 43(b). At this critical speed the hub center of measurement is close to the origin, consistent with the small bearing forces that are generated. At super-critical speeds, the whirl magnitudes become small, indicating that both the hub and flywheel are spinning about their centers of mass, as indicated in Figure 43(c).

Lead-Lag Synchronous Response to Spoke Misalignment

The synchronous response to spoke misalignment is shown in Figures 44 through 46. Figure 44 shows the hub center of mass (solid curve) and flywheel center of mass (dashed curve) whirl amplitudes and phase. This synchronous response exhibits one major critical speed occurring at the flexible-mode resonant frequency of 680 rad/sec. The bearing force, Figure 45, also exhibits a single maximum at this rotational speed.

The relative orientation of the hub, flywheel, and bearing force are shown in Figure 46 for sub-critical, critical, and super-critical rotational speeds. At sub-critical speeds, Figure 46(a), the flywheel center of mass M_f is seen to whirl about the flywheel elastic center S_f. At the critical speed of 680 rad/sec, the flywheel center of mass leads the flywheel elastic center by 90° degrees, as shown in Figure 46(b). This is the classic
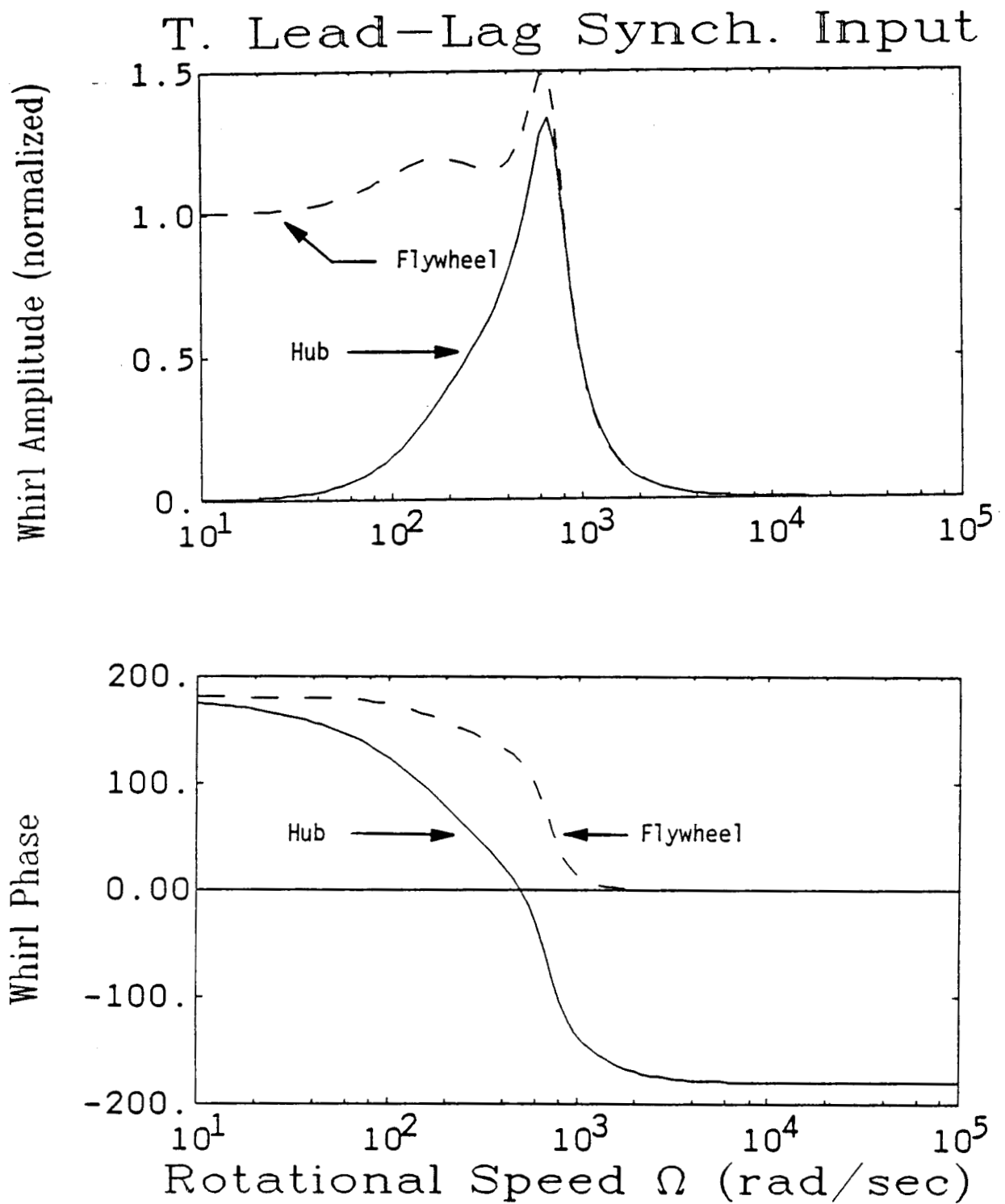
103

Figure 44. Synchronous Whirls caused by Spoke Misalignment:
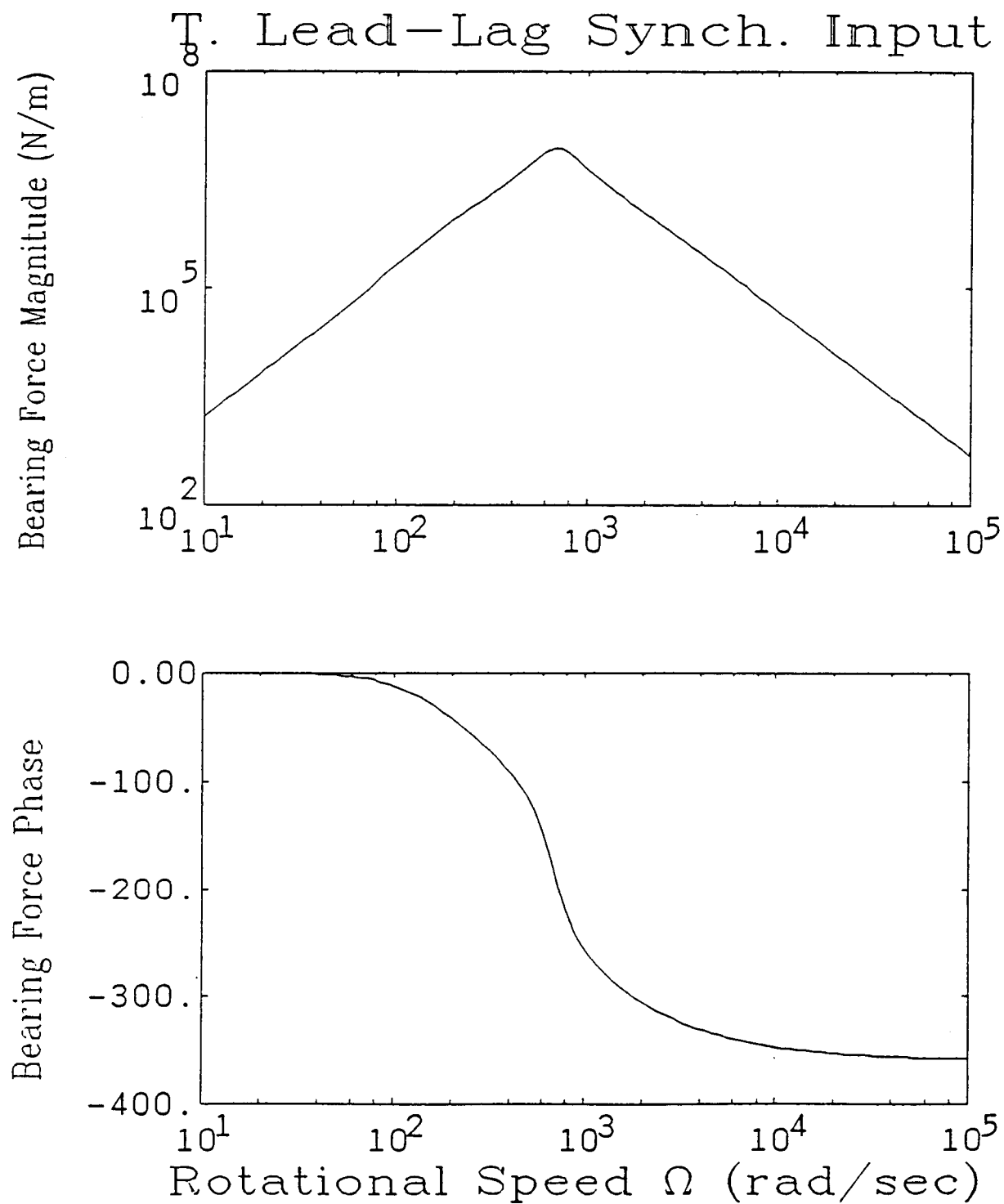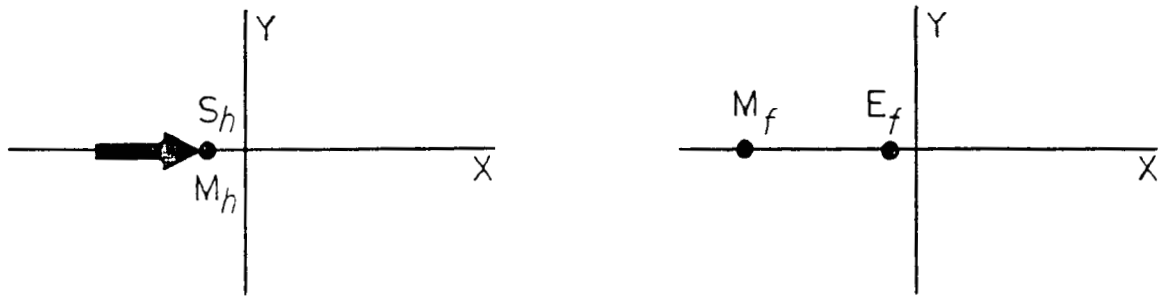Translational Medium-Bandwidth Lead-lag Compensator
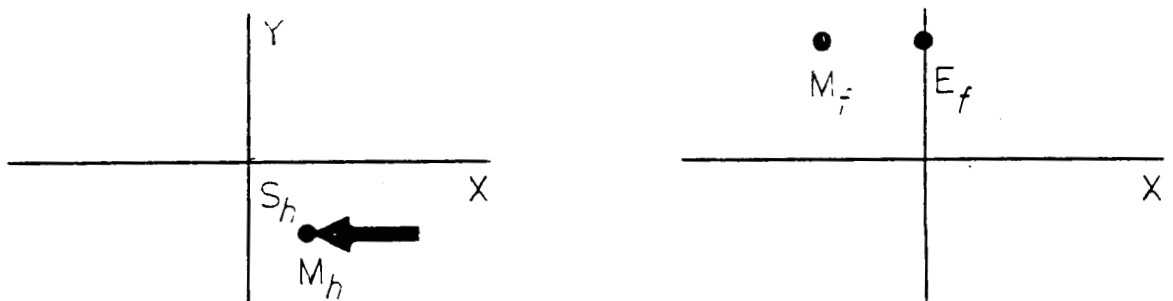
Figure 45.   Synchronous Bearing Force caused by Spoke Mis-
alignment: Translational Medium-Bandwidth Lead-lag
Compensator

105

Figure 46. Orientation of Flywheel and Hub during Synchronous Whirl caused by Spoke Misalignment: Translational Medium-Bandwidth Lead-lag Compensator
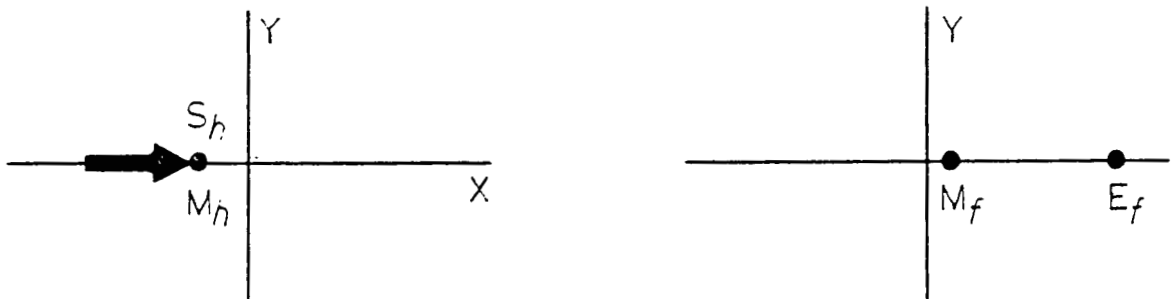
attribute of the critical speed of a single mass, flexible rotor [Johnson 1987a]. At this critical speed, the hub mass is also undergoing significant whirl. At super-critical rotational speeds, Figure 46(c), the hub and flywheel again spin about their centers of mass. Note that the bearing force caused by the spoke misalignment approaches zero at high speeds, in contrast to the synchronous response to the measurement error.

4.2 Lead-Lag Compensator with Tracking Notch Filter

Recall from the previous chapter that the stable operating speeds of the tracking notch filter were limited to speeds greater than the rigid-body cross-over. With the ACCESS flexible rotor, this remains true, as can be seen in Figures 47(a) and 47(b). Shown are closed-loop eigenvalue damping ratios of ACCESS under control of the tracking notch filter and lead-lag compensator. The rigid-body cross-over frequency is again chosen to be 300 rad/sec with the compensator lead and lag placed one-half decade below and above cross-over as before. The Q of the tracking notch filter is 10 as before. Figure 47(a) shows all the closed-loop eigenvalues plotted versus rotational speed. The eigenvalues are shown as crosses. The solid line indicates the stability boundary at zero damping ratio. Eigenvalues below this line are unstable.

Figure 47(b) shows the lightly damped eigenvalues more clearly. Note that as for the rigid-body rotor, the flexible ACCESS rotor is unstable at rotational speeds below approximately the rigid-body cross-over frequency at 300 rad/sec. The flexible
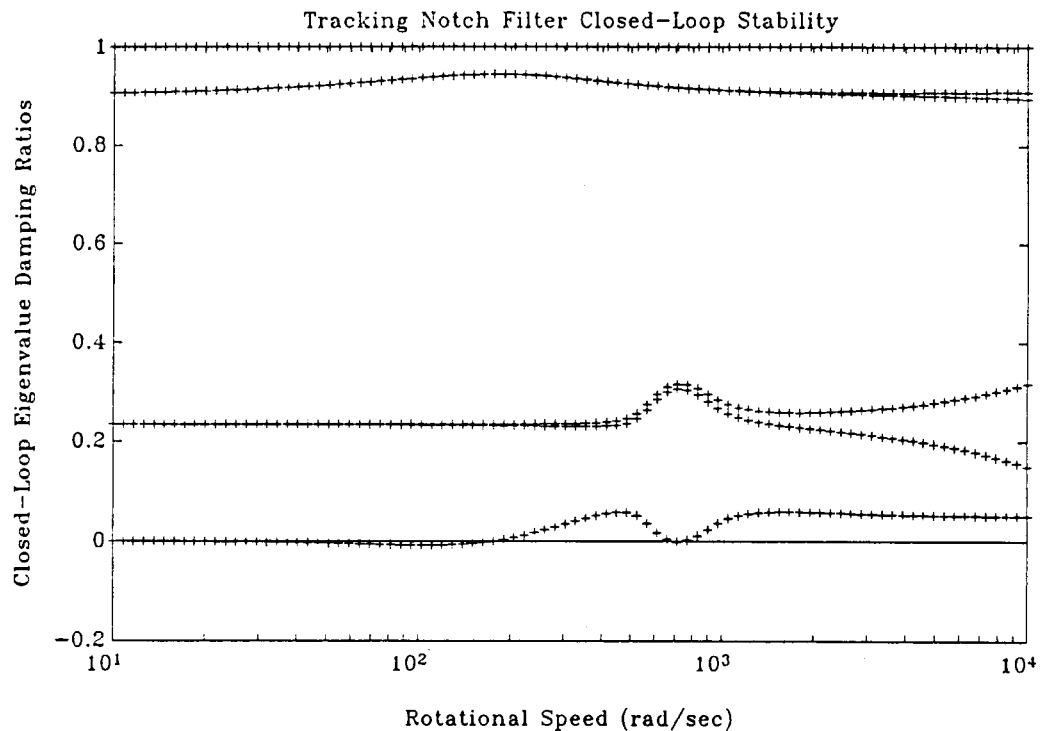
(a)
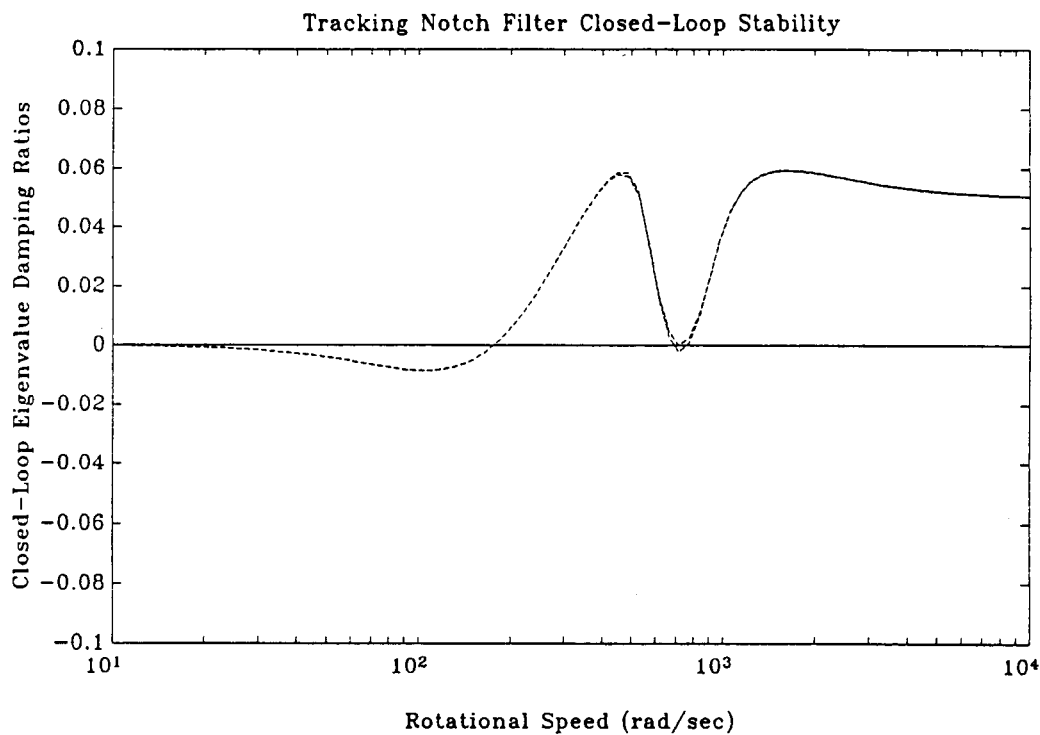
(b)

Figure 47. Tracking Notch Filter Closed-loop Stability

108

rotor system also becomes unstable at rotational speeds near the rotor natural frequency around 700 rad/sec. In these two speed ranges, therefore, the synchronous notch filter can not be used.

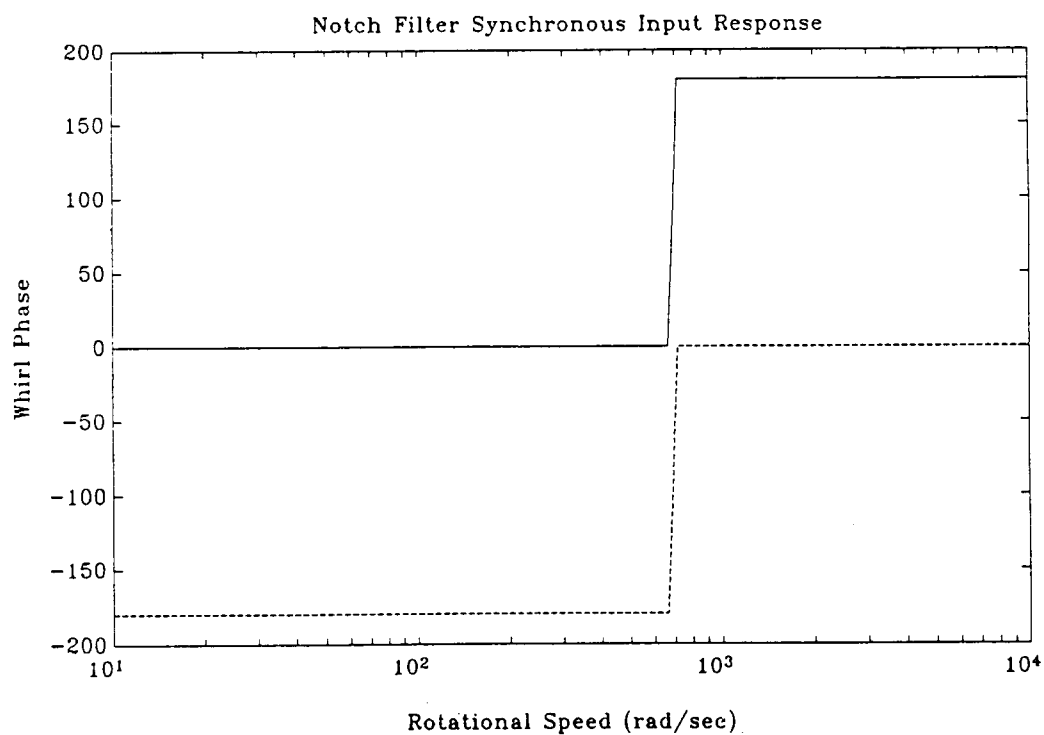## Tracking Notch Filter Synchronous Response

Recall that the tracking notch filter removes all synchronous signals from the feedback path. Because of this, no bearing force can be produced at the synchronous speed. In the stable operating speed ranges, therefore, the rotor spins about its center of mass and transmits no vibratory forces through the bearing. For the measurement or output error this system works perfectly - that is, both the flywheel and hub masses spin about their centers of mass - in its stable operating speed range.

The response to the spoke misalignment or input error is more complicated. Again, no bearing forces are produced at the synchronous speed and, therefore, no vibratory forces are produced by the bearing in its stable operating speed ranges. Since no synchronous forces are produced, the total center of mass of the combined hub and flywheel are stationary, as was true for the measurement or output error. The individual hub and flywheel masses do not spin about their centers of mass, however, as shown in Figure 48(a) and 48(b).

Shown are the whirl magnitudes and phases of the hub (solid line) and flywheel centers (dashed line) of mass versus rotational speed. As before, the hub and flywheel displacements are plotted normalized by the spoke misalignment distance. As shown in Figure 48(b), the hub and flywheel centers of mass are

109

Notch Filter Synchronous Input Response

(a)

Notch Filter Synchronous Input Response
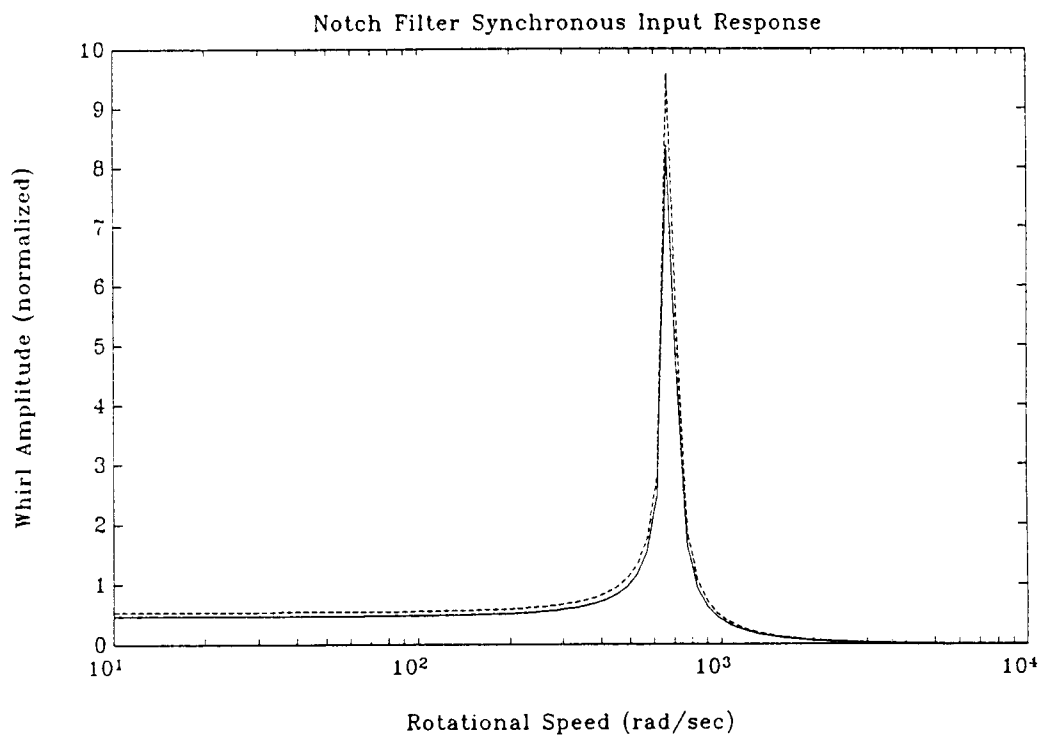
(b)

Figure 48. Synchronous Whirls caused by Spoke Misalignment: Tracking Notch Filter Compensator

always 180 degrees out of phase. The ratio of their whirl magnitudes is determined by the ratio of their masses such that the total center of mass of the combined hub and flywheel is stationary. Note that the magnitude of the whirls becomes large near the rotor natural frequency at about 700 rad/sec. Since no synchronous bearing forces are produced, the magnitude of these whirls is determined only by the internal damping in the rotor. Remember, of course, that the system is also unstable in this region.

4.3 Lead-Lag Compensator with Tracking Differential-Notch Filter

The closed-loop stability of the tracking differential notch filter (TDNF) used to control the ACCESS rotor is shown in Figures 49(a) and 49(b). Shown are the closed-loop damping ratios versus rotational speed. The lower figure, Figure 49(b), shows the behavior of the lightly damped poles more clearly. Again, the underlying lead-lag compensator crosses the rigid-body plant over at 300 rad/sec with the lead and lag centered on this frequency and separated by one decade in frequency. The Q of the TDNF is 10 as before.

As with the simple notch filter of the last section, the system effectively becomes unstable near the flexible rotational speed at about 700 rad/sec. Unlike the simple notch filter, however, the tracking differential-notch filter is stable at all other speeds. This result is consistent with the comparative stability of the two approaches used to control a rigid-body rotor, as presented in the last chapter.

111

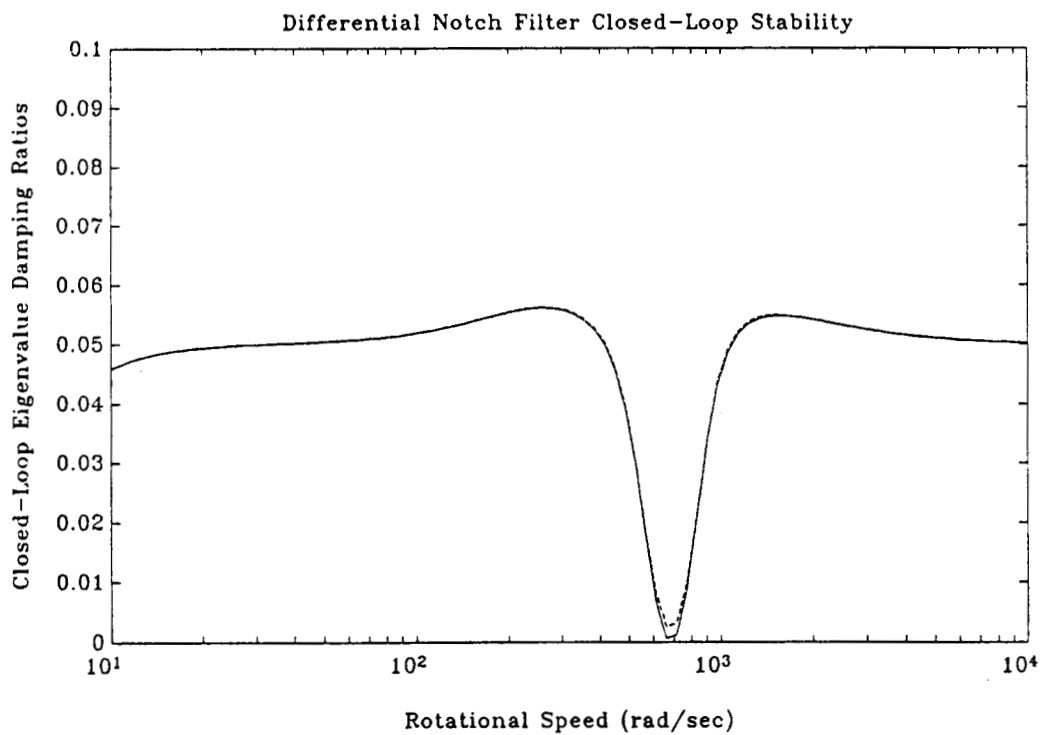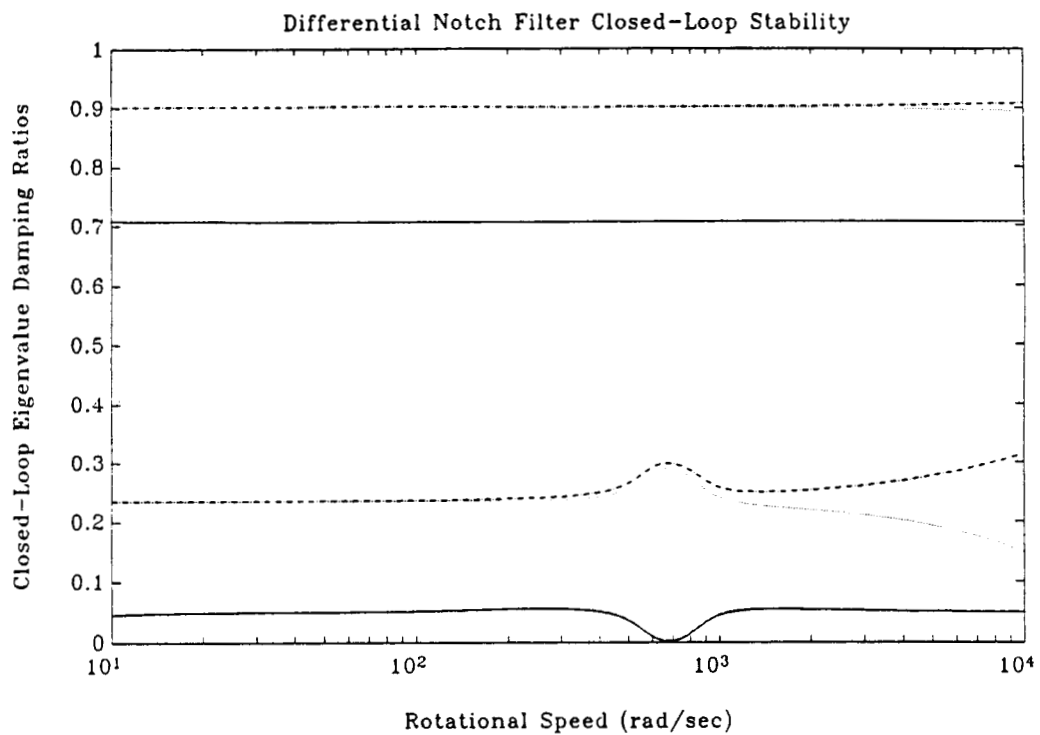**(a)**

(b)

Figure 49. Tracking Differential-Notch Filter Closed-loop
            Stability

This instability can be cured by using a hybrid controller that behaves as a lead-lag compensator near the flexible mode frequencies and as a tracking differential-notch filter at all other frequencies. This can be simply done by inserting a fixed frequency bandpass filter in parrallel with the tracking bandpass filter shown in Figure 30. The total bandpass filter shown in Figure 30 then has the form

$$P(s,\Omega_f) = \cfrac{\cfrac{\Omega_f s}{Q}}{s^2 + \cfrac{\Omega_f s}{Q} + \Omega_f^2} - \cfrac{\cfrac{\Omega_s s}{Q_s}}{s^2 + \cfrac{\Omega_s s}{Q_s} + \Omega_s^2} \qquad (54)$$

The first term is simply the tracking bandpass filter of Equation 50. The second term is a fixed frequency (stationary) bandpass filter with its bandpass frequency Ω_s nominally set to be equal to the flexible mode frequency of the system. The Q of this term (Q_s) is generally set to be low relative to the Q of the tracking term. Near the flexible mode frequency, these two terms cancel and the net compensation is essentially the lead-lag compensator. This can be seen in Figure 30 if the bandpass filter is set to zero.

Using this hybrid compensator, the system stability is vastly improved. This can be seen in Figure 50, a plot of the minimum closed-loop eigenvalue damping versus rotational speed for the tracking notch filter (solid line), differential tracking notch filter (dot-dashed line), and hybrid compensators (dashed line). Note that the hybrid compensator remains stable through
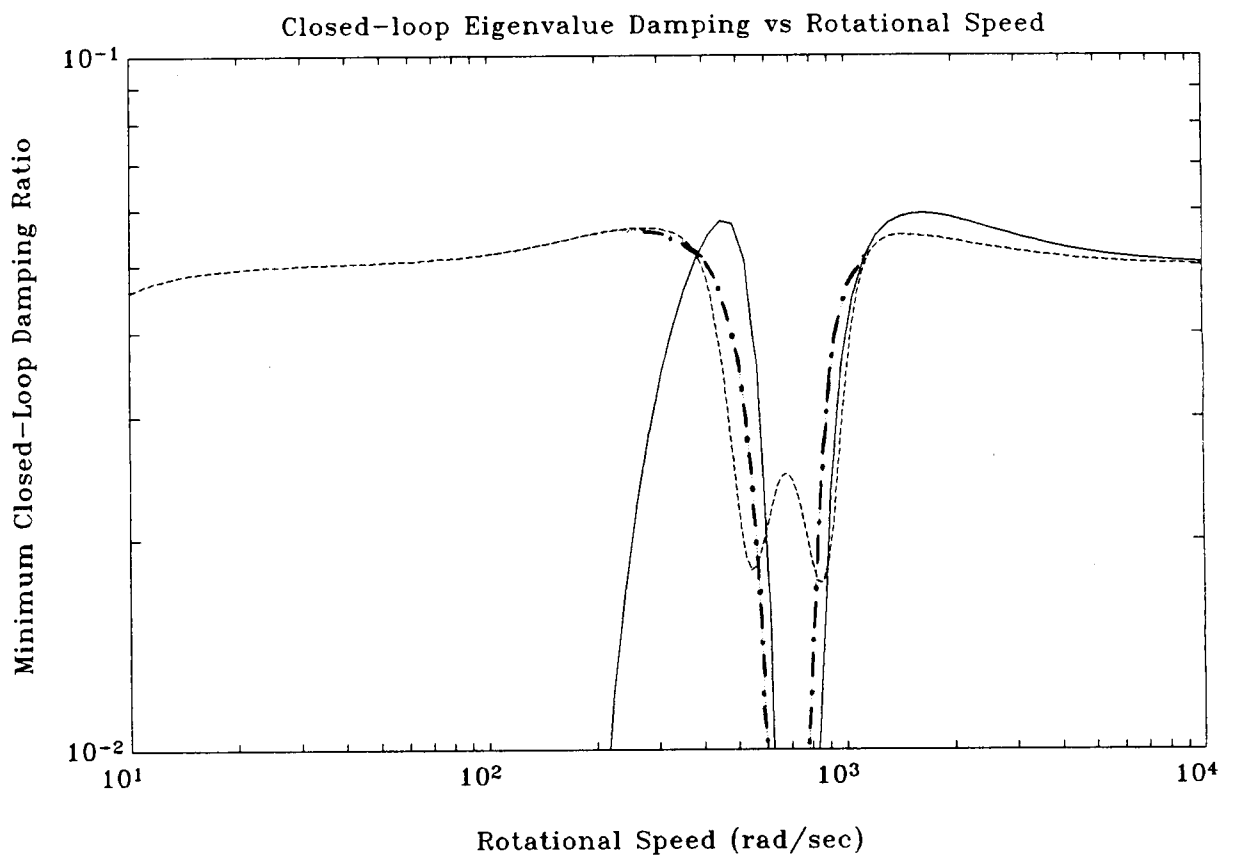
113

Figure 50. Hybrid Controller Closed-loop Stability

the flexible mode critical speed, unlike either the tracking notch filter or the tracking differential-notch filter.

Tracking Differential-Notch Filter Synchronous Response

In their stable operating speed ranges, the synchronous response results for the tracking differential-notch filter are the same as for the simple notch filter, which were presented in the last section. Both systems produce no synchronous forces in the bearings. As before, for the spoke misalignment or input error, this requires that the hub and flywheel centers of mass spin about each other, as shown in Figure 48. The advantage of the TDNF over the simpler tracking notch filter is its vastly increased range of stable operating speeds.

Because the hybrid compensator behaves as a lead-lag compensator near the flexible mode frequencies, it uses synchronous forces near these frequencies. Its response to measurement error, therefore, is not perfect as can be seen in Figure 51. Its response to spoke misalignment is also different from the simple tracking differential-notch filter, as can be seen in Figure 52.

4.4 Model Based Compensators

The synchronous response results for the medium-bandwidth, high-frequency loop recovery, 1000 rad/sec design rotational speed model based compensator will be presented in this section. For details of this compensators structure and stability results, see the earlier final report [Johnson 1987b].
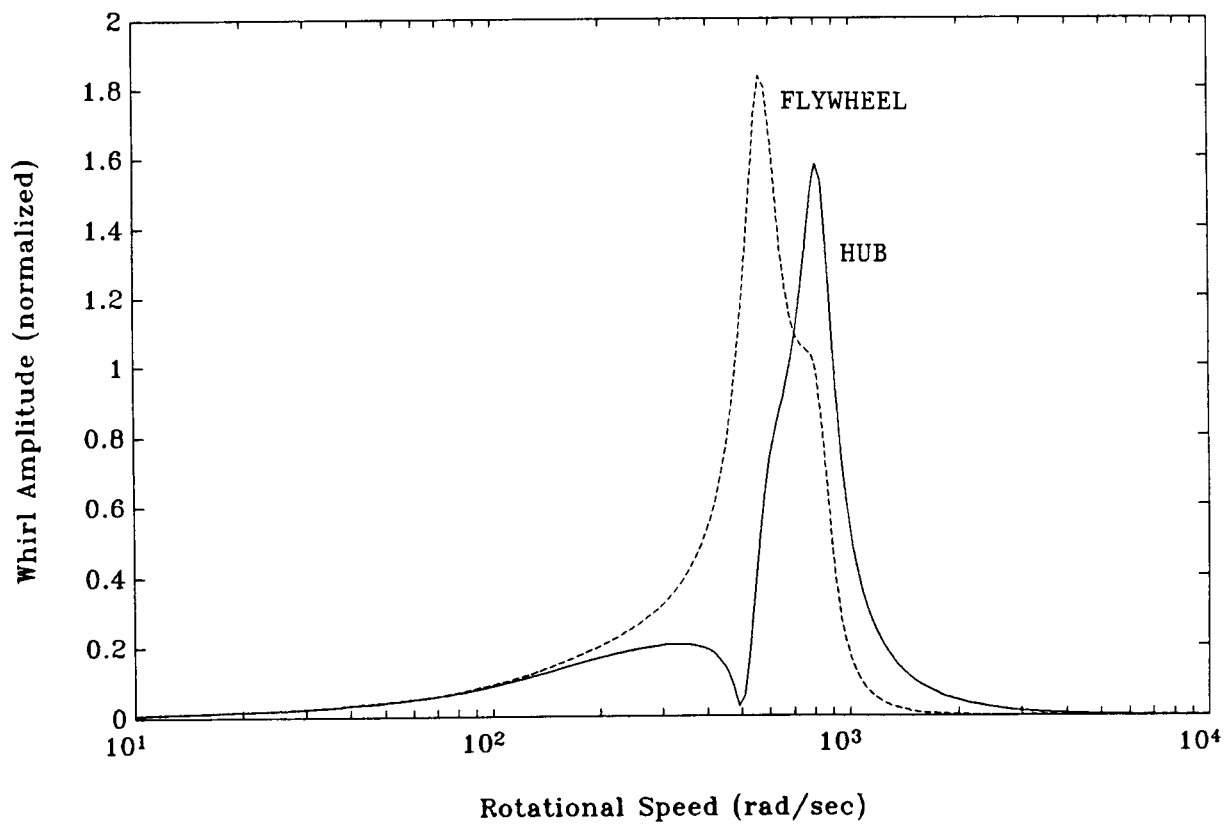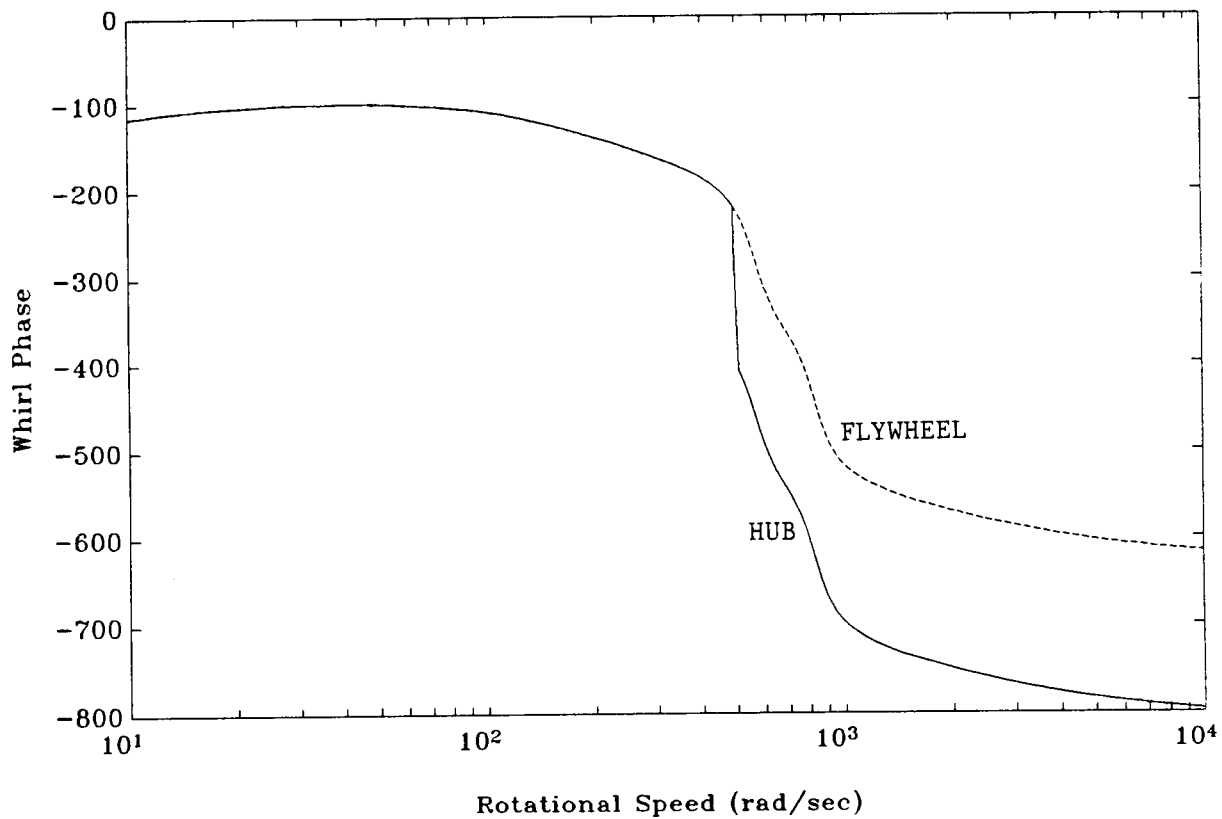
Figure 51. Synchronous Whirls caused by Measurement Error:
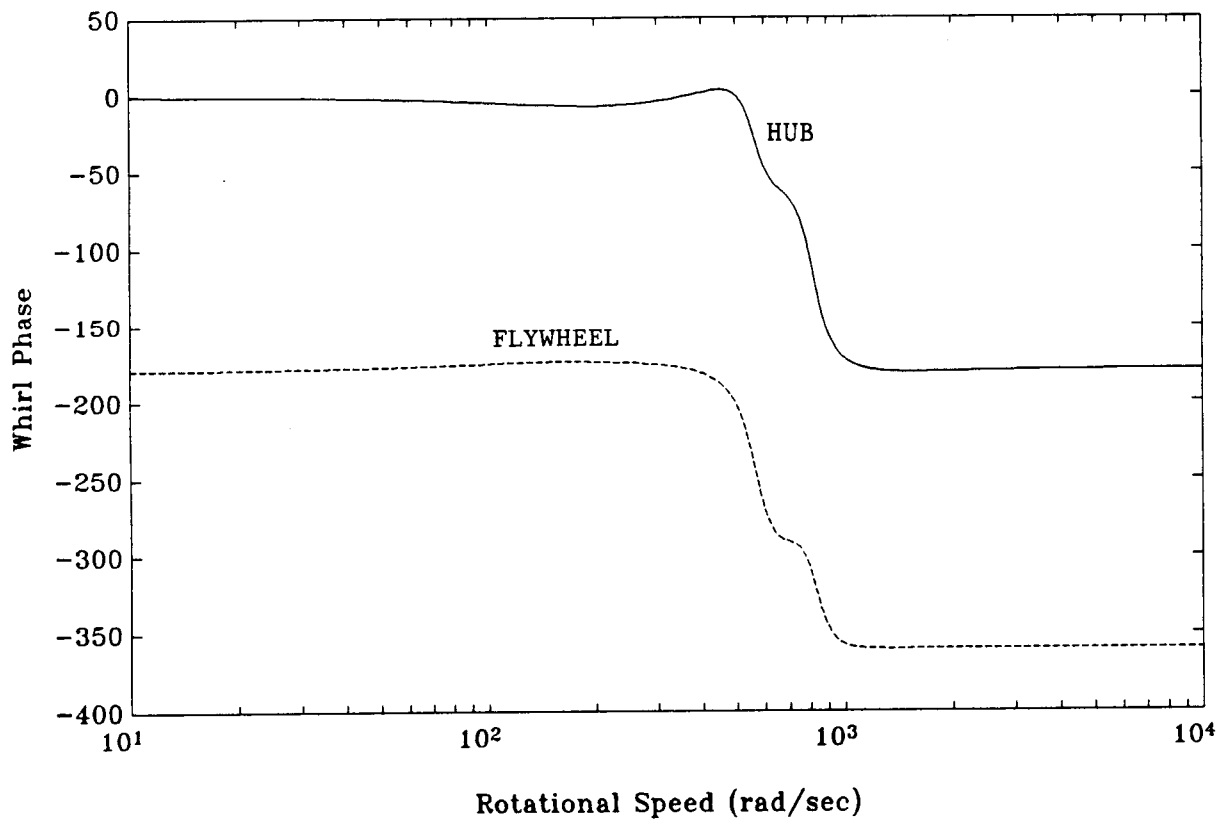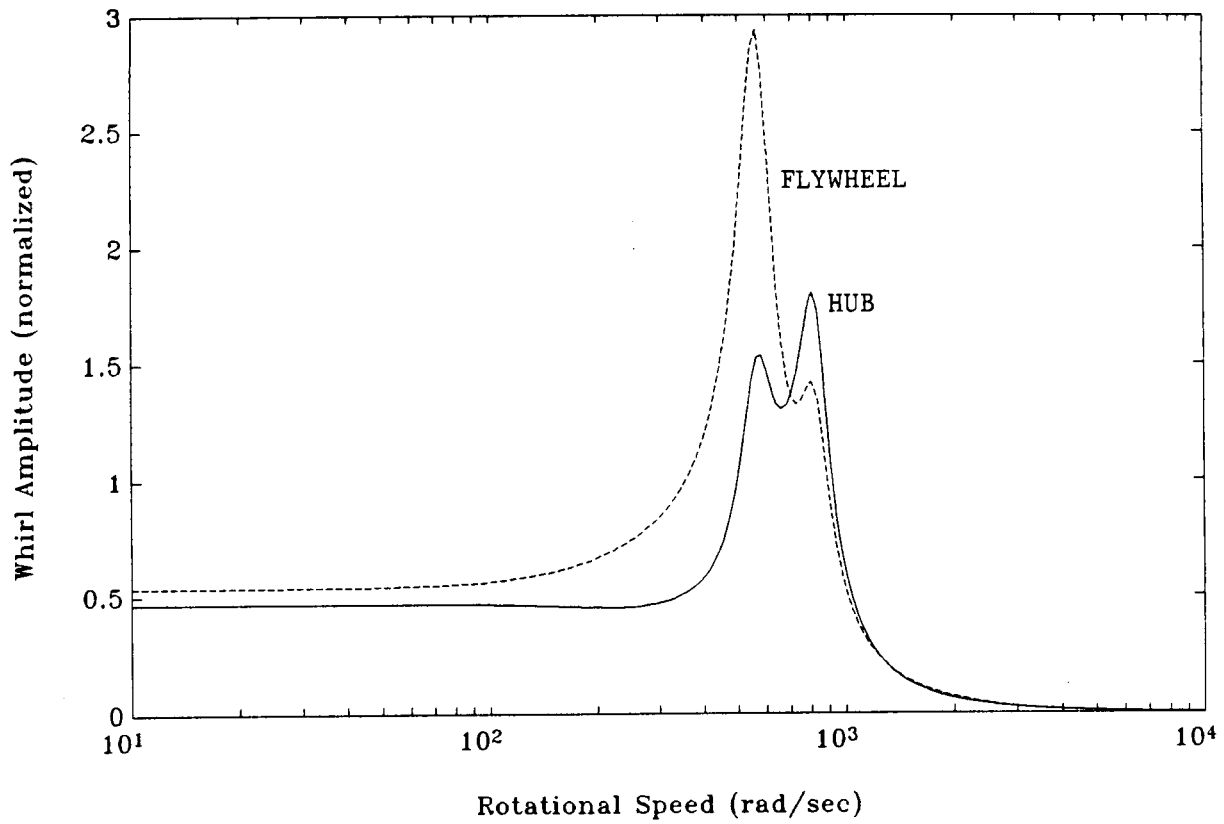Hybrid Compensator

Figure 52. Synchronous Whirls caused by Spoke Misalignment: Hybrid Compensator

117

Model Based Compensator Synchronous Response to Measurement Error

The synchronous response to measurement error is shown in Figures 53 through 55. Figure 53 is a plot of the normalized hub center of mass (solid curve) and flywheel center of mass (dashed curve) synchronous whirl amplitudes (Figure 53(a)) and phases (Figure 53(b)). Two critical speeds can be seen. The first critical speed, corresponding to the transmission zero frequency of 497 rad/sec, features large flywheel whirl amplitudes but negligible hub amplitudes. The second critical speed, at the flexible-mode resonant frequency of 680 rad/sec, involves only moderate amplitude whirls of both the hub and flywheel.

The synchronous bearing force caused by this measurement error is shown in Figure 54. Figure 54(a) shows the magnitude of the bearing force and Figure 54(b) the direction at which the bearing force acts on the hub. The magnitude of the bearing force is normalized by the spoke misalignment distance and has units of Newtons per meter of spoke misalignment. Note that the magnitude of the bearing force is a maximum at the first critical speed and a local minimum at the second critical speed.

The orientations of the various hub centers, flywheel centers, and bearing force are given by the phase plots of Figure 53(b) and 54(b). These can be more easily interpreted by plotting in the radial plane the relative locations of the hub centers and flywheel centers and relative direction of the bearing force. This is done for sub-critical, first critical, second critical, and super-critical rotational speeds in Figure

Figure 53. Synchronous Whirls caused by Measurement Error: Model Based Compensator

Figure 54.   Synchronous Bearing Force caused by Measurement
Error: Model Based Compensator

a) Sub-critical

b) First critical
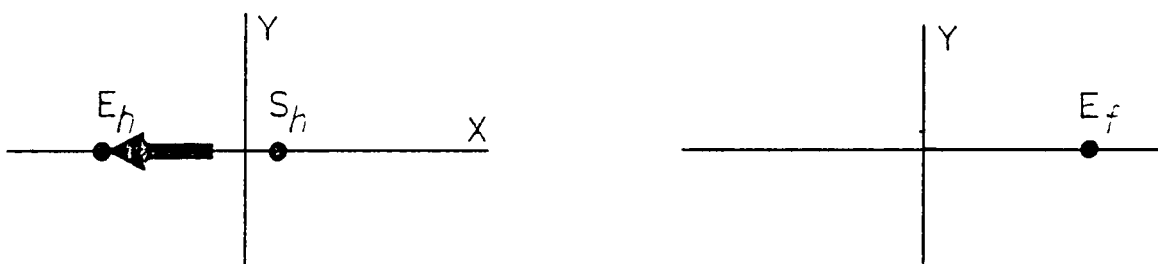
c) Second critical
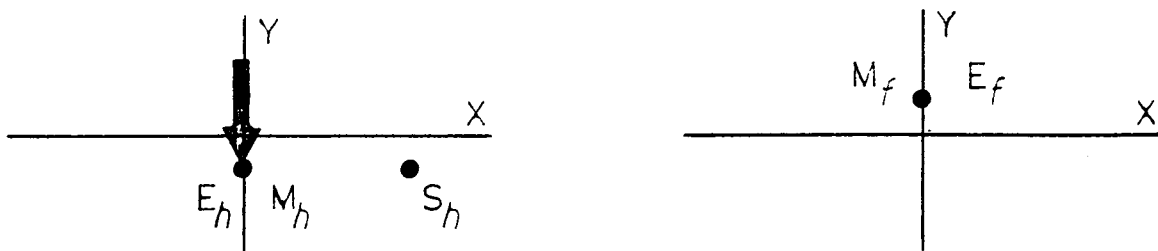
Hub   d) Super-critical   Flywheel

→ Bearing force

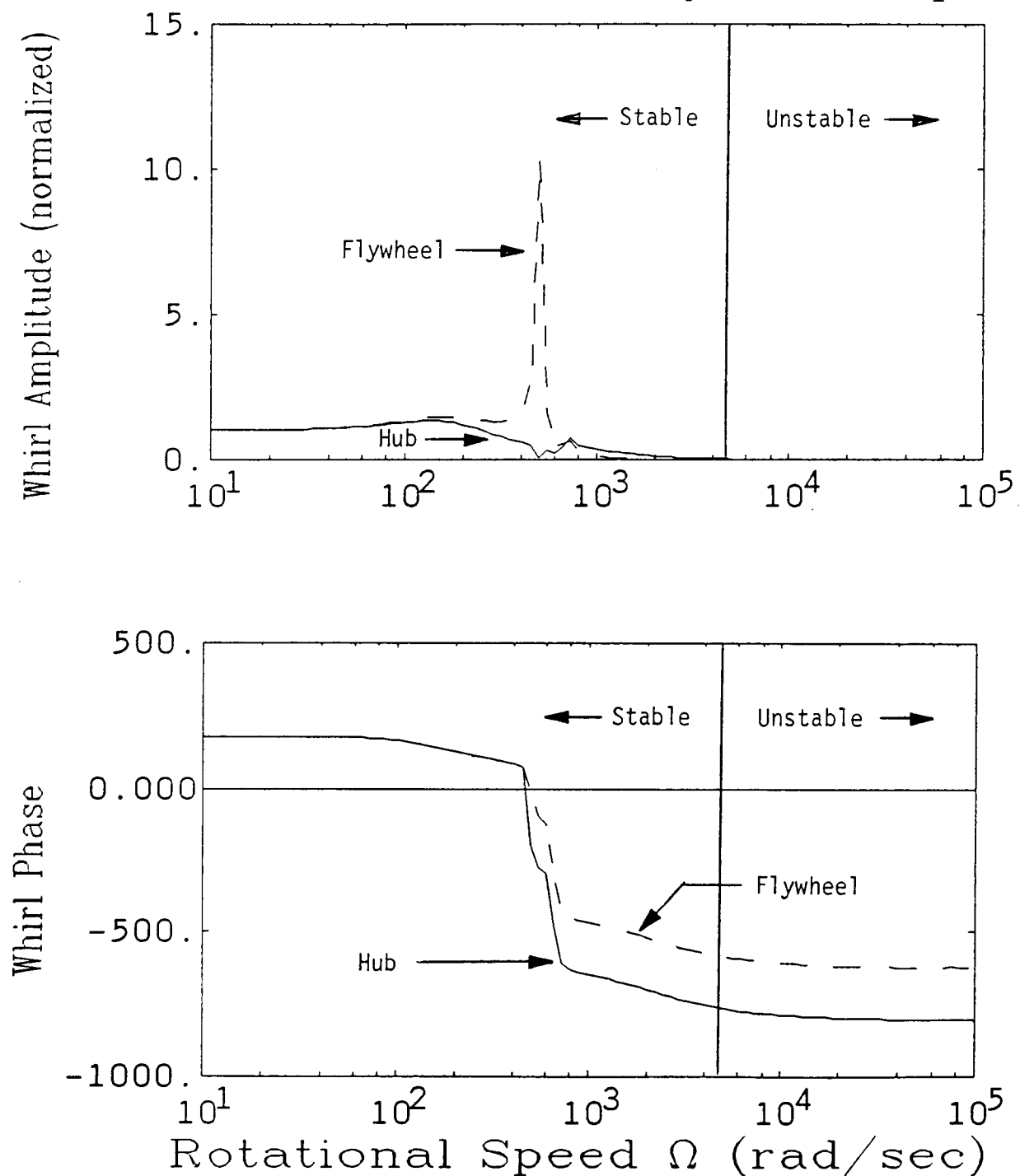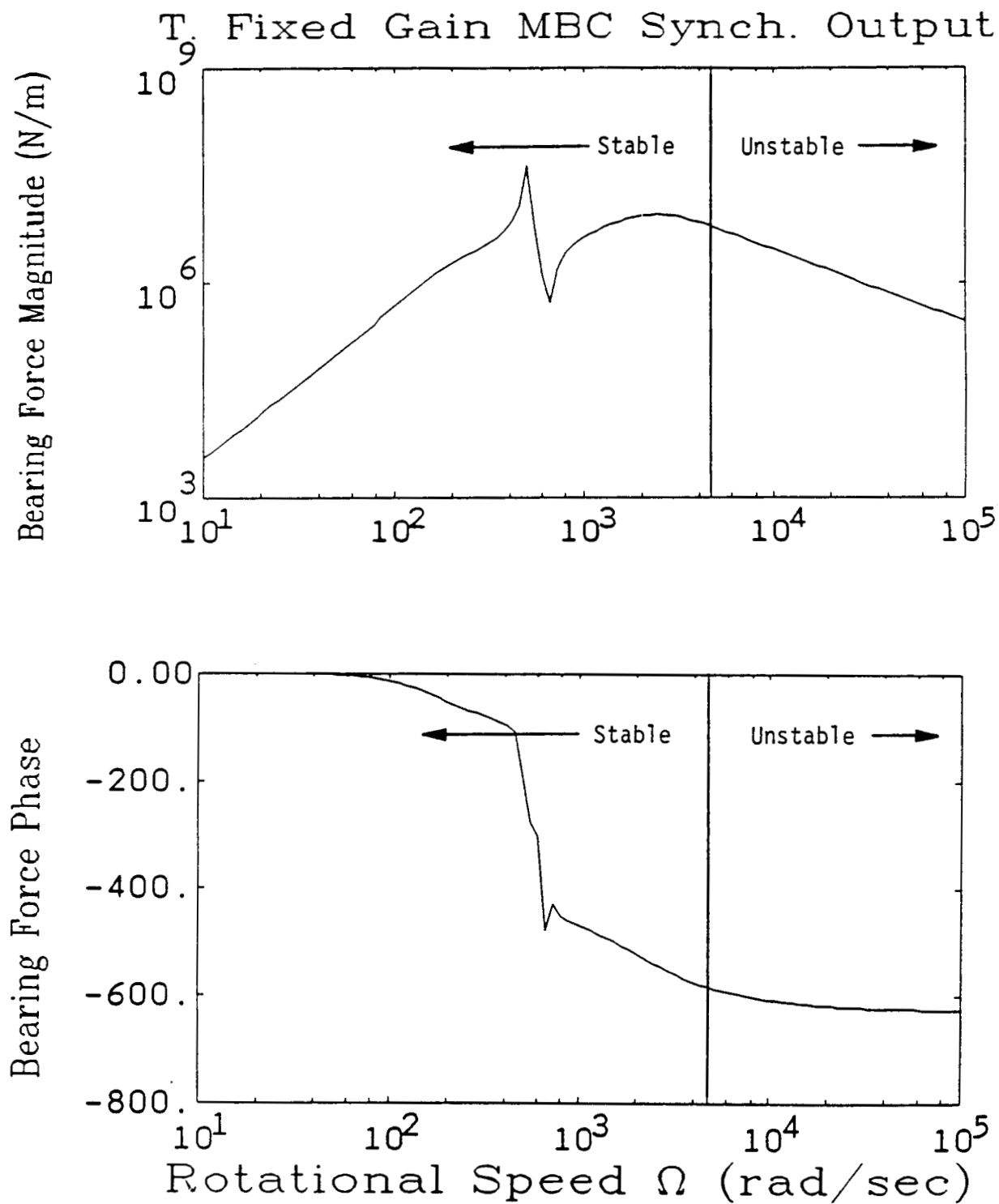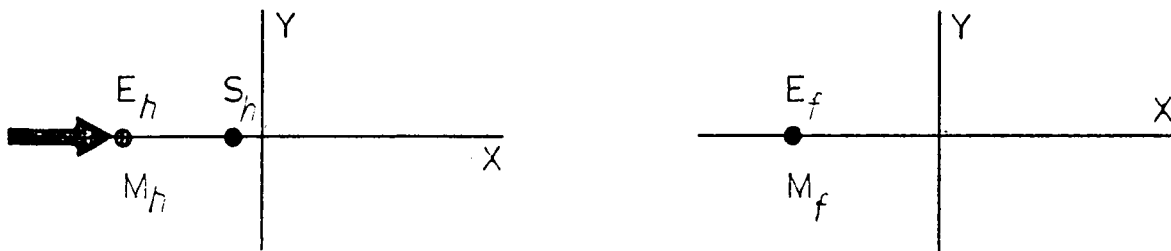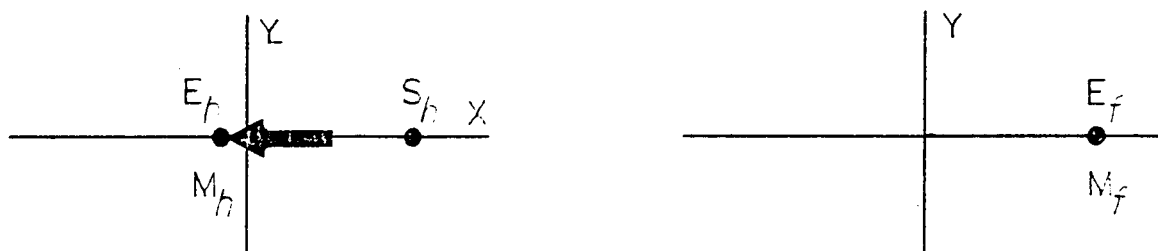Figure 55.   Orientation of Flywheel and Hub during Synchronous Whirl caused by Measurement Error: Model Based Compensator

55. The locations of the of hub and flywheel centers of mass are given by M_h and M_f and the locations of the elastic centers by E_h and E_f. The location of the hub center of measurement is given by S_h.

At sub-critical speeds, the rotor spins about the measurement center S_h as shown in Figure 55(a). At these low speeds, both centers of mass exhibit normalized unit magnitude whirls. At the first critical speed, which corresponds to the transmission zero frequency, the hub and flywheel centers of mass are 180 degrees out of phase, as shown in Figure 55(b). At this transmission zero frequency, the flywheel mass is acting as a dynamic vibration absorber [Harris 1976, p.6-1] leading to large flywheel whirl amplitudes. The amplitude of the hub whirl is negligible, however, as expected from viewing the phenomenon either as a dynamic vibration absorber or transmission zero. Although the hub center of mass is close to the origin, the hub center of measurement undergoes unity whirl, consistent with the large bearing forces seen at this first critical speed.

At the second critical speed, corresponding to the flexible-mode resonance, the hub and flywheel both have approximately unity magnitude and are still out of phase by 180 degrees, as shown in Figure 55(c). At this second critical speed, however, the hub center of measurement is close to the origin, consistent with the small bearing forces that are generated. At super-critical speeds, the whirl magnitudes become small, indicating that both the hub and flywheel are spinning

about their centers of mass (see Figure 55(d)).

The nature of this synchronous response to output disturbance results from the general characteristics of the systems controlled by linear quadratic regulators [Kwakernaak 1972, p.312] with loop transfer recovery (LQR/LTR) and the specific design choices made for this compensator. Four specific features of this controlled rotor system must be acknowledged when interpreting these general disturbance rejection properties of LQR/LTR systems to this rotor system. These four features are:

(1) The state weighting matrix used in the LQR design did not place any cost on flywheel states.

(2) The controller design is fixed and the plant is varying with rotational speed.

(3) The plant is non-minimum phase at high speeds.

(4) This is an output disturbance, not an input disturbance.

The following paragraphs discuss the ramifications of these four features.

Because no cost was placed on flywheel states in the LQR design, large amplitude whirls of the flywheel are acceptable, even desirable, if they help keep hub whirl amplitudes small. This is exactly what happens at the first critical speed, where the flywheel whirl amplitude is large and the hub amplitude small. If the amplitudes of flywheel synchronous whirls are important, they can be reduced by appropriately choosing the

123

state weighting matrix in the LQR design procedure.

The synchronous response of this rotor system cannot be cast exactly into the mold of a LQR/LTR system because the plant varies with rotational speed. When looked at as a LQR/LTR disturbance rejection problem, the plant varies with frequency, invalidating the fixed plant assumptions implicit in LQR/LTR properties. The synchronous response of the controlled rotor system, however, does closely approximate the disturbance rejection properties of the system at fixed speed. Because of these similar responses, the amplitude of the synchronous response of the hub to measurement error, Figure 56, is very nearly the same as the disturbance rejection properties of the underlying LQR at fixed speed, which is shown in Figure 7.1.6a of [Johnson 1987a].

The good properties of the LQR, including disturbance rejection, can only be recovered if the system is non-minimum phase [Kwakernaak 1972, p.423; Stein 1987]. At sub-flexible rotational speeds, the system is minimum phase. At rotational speeds up to the second critical speed, therefore, good recovery of the underlying LQR disturbance rejection properties is expected. This speed range is where the disturbance rejection properties are important, because of the flexible dynamics. At higher rotational speeds, past the flexible resonance and where the system is non-minimum phase, the disturbance rejection problem is less difficult.

For a multi-input, multi-output system the loop transfer function matrix depends on whether the loop is broken at the

input to the plant or the output from the plant. The input and output disturbance rejection properties of the closed-loop system are not, therefore, identical. For the LQR/LTR the good properties of the underlying LQR will be reflected in input disturbance rejection properties. For two-input, two-output, block-symmetric systems such as the CARES translational model, however, the loop transfer function broken at the input to the plant is the same as the loop transfer function broken at the output to the plant. In Section 6.2 of Johnson [1987a] this result is derived and discussed. The good input disturbance rejection properties of the LQR loop also exist for output disturbances for this system, as was seen in the hub response to measurement error presented above.

Because of the good disturbance rejection properties of the LQR/LTR method and the special properties of this system, the synchronous response to measurement error is good. The maximum hub whirl amplitude, normalized by the measurement error distance ϵ_s, is less than 1.2. The maximum flywheel amplitude is much greater, approximately 10, because no costs were placed on flywheel states in the LQR design.

Synchronous Response to Spoke Misalignment

The synchronous response to the spoke misalignment is shown in Figures 56 through 58. Figure 56 is a plot of hub (solid curve) and flywheel (dashed curve) synchronous whirl amplitudes and phase. The whirl amplitudes plotted in Figure 56 are normalized by the spoke misalignment distance and are again,

125

T. Fixed Gain MBC Synch. Input

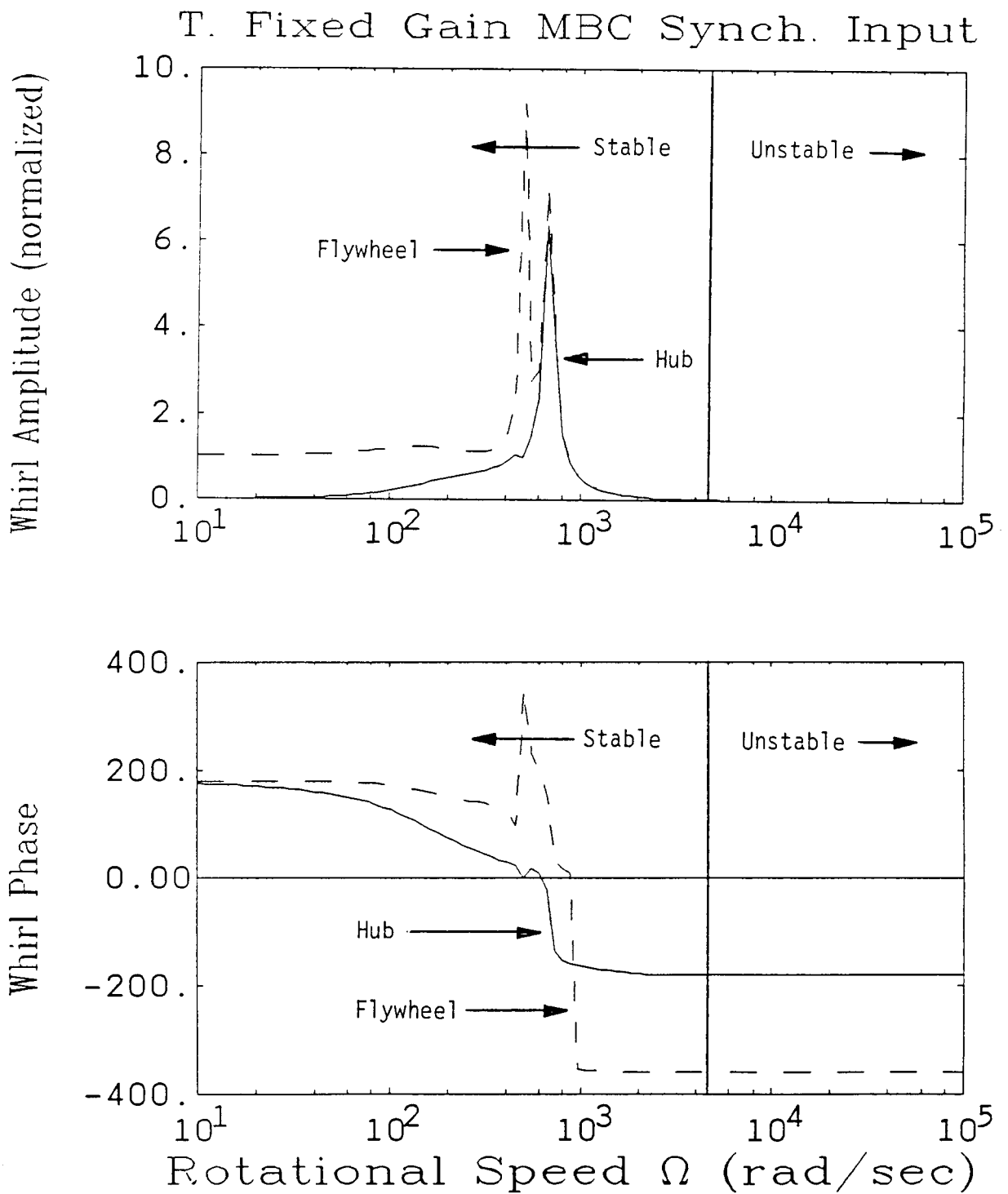Figure 56. Synchronous Whirls caused by Spoke Misalignment: Model Based Compensator
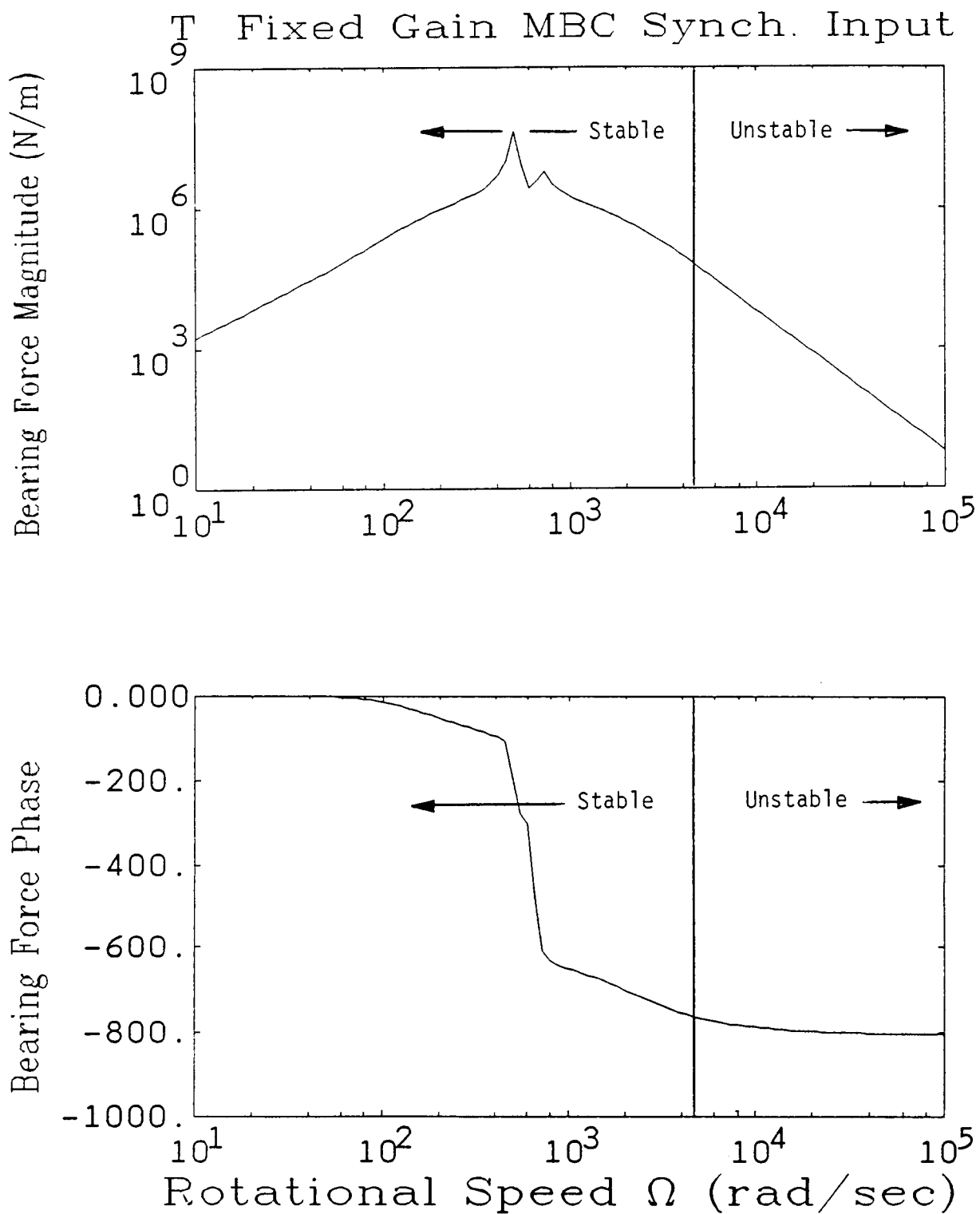
Figure 57.   Synchronous Bearing Force caused by Spoke
Misalignment: Model Based Compensator

a) Sub-critical

b) First critical

c) Second critical

Hub   d) Super-critical   Flywheel

Bearing force
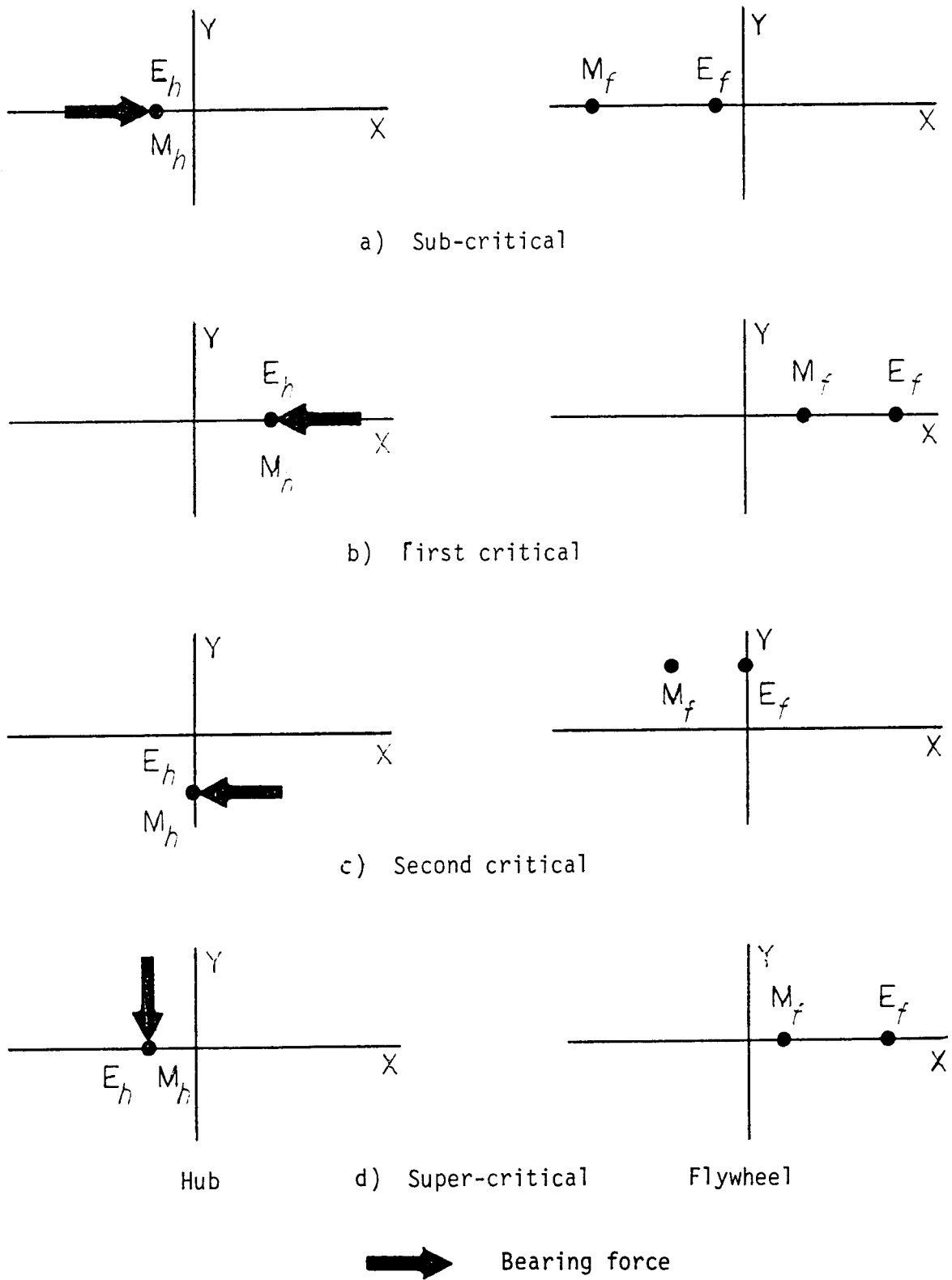
Figure 58.   Orientation of Flywheel and Hub during Synchronous Whirl caused by Spoke Misalignment: Model Based Compensator

therefore, non-dimensional. There are two critical speeds where large hub and/or flywheel whirl amplitudes are found. The first again corresponds to the system transmission zero frequency of approximately 497 rad/sec and the second again corresponds to the flexible-mode eigenvalue frequency of approximately 680 rad/sec. The synchronous bearing force that results from the spoke misalignment is shown in Figure 57. Again, the bearing magnitude is normalized by the measurement error distance.

Again, the results can be best interpreted by examining the relative orientation in the radial plane of the hub, flywheel, and bearing force. These orientations are shown in Figure 58 for sub-critical, first critical, second critical, and super-critical speeds where the notation from Figure 55 is used. For this spoke misalignment, the hub measurement center S_h is not explicitly shown since it is assumed coincident with the hub mass center M_h.

At sub-critical rotational speeds the rotor spins about its elastic axis and only small bearing forces are used. The center of mass of the flywheel is then whirling about the its elastic center, as shown in Figure 58(a). The first critical speed, at a frequency of 497 rad/sec, corresponds to the transmission zero of the system. Again, at this first critical speed the hub whirl amplitude is relatively small compared to the flywheel whirl amplitude. Note that the bearing force is essentially conservative for this whirl.

The second critical speed, at a frequency of 680 rad/sec, corresponds to the flexible-mode resonant frequency. At this

rotational speed both the hub and flywheel experience large amplitude whirls. The hub and flywheel are out of phase by 180 degrees, as can be seen in Figure 58(c). The flywheel center of mass leads the flywheel elastic center by 90 degrees, similar to the synchronous response of a single mass rotor at its critical speed [Gunter 1966, p.12]. Note that the bearing force is removing energy from this whirl. At super-critical speeds, both rotor masses, hub, and flywheel spin about their mass centers as shown in Figure 58(d). The synchronous bearing forces drop continuously in this super-critical speed range.

The synchronous response to the spoke misalignment, just presented, is much worse than the synchronous response to the measurement error. The maximum flywheel and hub normalized whirl amplitudes are both approximately equal to 10. The reason for this poor result is that the synchronous response to spoke misalignment is not the beneficiary of the good disturbance rejection properties of the LQR/LTR method. The spoke misalignment forces the plant directly, with disturbance forces acting on both the flywheel and hub. These disturbances cannot be reflected as input disturbances because the plant input is the bearing force, which acts only on the hub. The effect of the spoke misalignment therefore cannot be modelled as a simple additive disturbance to the loop, as was done for the measurement error to the system output. Even if cost were placed on the flywheel state in the LQR design, the resulting LQR/LTR loop would not necessarily adequately reject the disturbance caused by spoke misalignment.

5. SUMMARY AND CONCLUSIONS

This report has presented the results of an investigation into the control of an advanced Annular Momentum Control Device (AMCD), the AMCD Combined Control Energy Storage System (ACCESS). This system, which consists of high-speed, magnetically suspended flywheels, presents a variety of control problems because of the open-loop unstable nature of its operation at high rotational speeds and the variation of its dynamics as the rotational speed is changed. This synchronous response research is an extension of an earlier NASA sponsored SatCon research program (NASA contract NAS1-17560) that developed stabilizing control algorithms for the ACCESS. This synchronous response phase of the research has included the development of a dynamic model of the system capable of modelling its synchronous response to geometric imperfections ("mass unbalances") and the design of innovative controllers that minimize the synchronous vibrations.

This research effort required the development of synchronous response models of the ACCESS. These models, presented and developed in Chapter 2, are capable of predicting the response of the system to both errors in measurement of the center of mass and misalignments between the hub and flywheel masses. The measurement error corresponds to the rigid-body mass unbalance problem of conventional rotor dynamics. This error mechanism can be modelled as an additive, synchronous output disturbance. The spoke misalignment error is unique to flexible rotors and corresponds to the individual mass unbalances in a conventional

131

multi-mass, flexible rotor system. The spoke misalignment error cannot be modelled as either a simple input or output additive, synchronous disturbance.

After development of the synchronous models, four different control algorithms were examined. These were lead-lag compensators that mimic conventional bearing dynamics, tracking notch filters used in the feedback loop, tracking differential-notch filters, and model based compensators. The first two approaches, lead-lag and tracking notch filters, are the conventional approaches for magnetic bearing applications. They suffer from a number of disadvantages, however, including either poor synchronous performance or poor stability. The third approach, tracking differential-notch filters, was developed under this program. These controllers combine the best features of both the lead-lag and tracking notch filters. The fourth approach investigated the use of model based compensators, as developed under the previous NASA contract.

For use in rigid-body control, the tracking differential-notch filter (TDNF) developed under this contract was the best. It eliminated synchronous vibrations produced by measurement error and was stable over the entire speed range. The simple notch filter had equally good synchronous response performance but was stable only at speeds greater than the cross-over frequency (super-critical speeds). In contrast, the lead-lag compensator was stable at all speeds, including sub-critical, but had relatively poor synchronous response at sub-critical speeds.

For the rigid-body rotor, the model-based compensator algorithm produces a simple lead-lag compensator.

Hardware implementation schemes for the tracking differential notch filter (TDNF) were investigated. A simple design was developed that can be implemented with analog multipliers and low-bandwidth digital hardware. An additional advantage of this design is that it can be made into an adaptive controller with relatively simple modifications in the low-bandwidth, digital section of the control hardware.

For the flexible rotor of the ACCESS, the advantage of the TDNF approach over the simple tracking notch filter was the same as for the rigid-body rotor. Both had good synchronous response performance in their stable operating ranges. Again, the tracking notch filter was unstable at sub-critical rotational speeds, whereas the TDNF was stable in this range. Both notch filter approaches had stability problems near the flexible mode critical speed, however. The lead-lag compensator again had poorer synchronous response, but was stable over the whole speed range. A trade-off between the good synchronous response of the tracking differential-notch filter and the good stability response of the lead-lag compensator was acheived with the hybrid compensator that behaves as a lead-lag compensator near the flexible mode frequency and behaves as a TDNF at all other frequencies. This hybrid compensator is also easily implemented.

Both the tracking notch and tracking differential-notch filter approaches eliminate all feedback from the plant at the

synchronous frequency, thus eliminating all bearing forces caused by measurement errors or spoke misalignments. These filtering approaches, therefore, work well at eliminating any synchronous vibrations produced by the bearing, but suffer from stability and synchronous displacement problems. The synchronous feedback signal is needed for stability in many speed ranges. The TDNF adds back into the feedback loop a synchronous component based on a model of the plant. This greatly improves its stable speed ranges compared to a simple notch filter. The hybrid compensator additionally adds the lead-lag compenstor forces near the flexible mode frequency to further improve stability.

In addition, synchronous bearing forces may also be desired to limit the synchronous whirl amplitudes of the rotor. This is a problem only for the flexible rotor where the two individual masses can exhibit large whirl amplitudes while their combined center of mass does not move. If these large amplitude whirls cause problems, such as clearance or rotor strain, the use of synchronous bearing forces to control them may be desirable. The use of these forces, of course, will cause synchronous vibrations to be passed to the spacecraft.

Based on this research, the best synchronous response approach now available is to use the tracking differential-notch filter except near the critical speed where the underlying lead-lag compensators should be used, as in the hybrid compensator. This can be simply implemented based on the hardware design developed under this contract.

BIBLIOGRAPHY

Anderson, W.W. [1973] and C. Keckler. An Integrated Power/Attitude Control System (IPACS) for Space Vehicle Application. Presented at the Fifth IFAC Symposium on Automatic Control in Space, Genoa, Italy.

Anderson, W.W. [1975] and N.J. Groom. The Annular Momentum Control Device (AMCD) and Potential Applications. NASA TN D-7866.

Anderson, W.W. [1979], N.J. Groom, and C.T. Woolley. Annular Suspension and Pointing System. AIAA Journal of Guidance and Control 2, No. 5 (Sept-Oct 1979): pp. 367-373.

Beatty, Reinhard [1988]. Notch Filter Control of Magnetic Bearings to Improve Rotor Synchronous Response. Masters Thesis, Massachusetts Institute of Technology.

Bleuler, H [1984]. Decentralized Control of Magnetic Rotor Bearing Systems. Doctor of Technical Sciences Dissertation, Swiss Federal Institute of Technology, Zurich.

Downer, J.R. [1980]. Analysis of a Single Axis Magnetic Suspension System. S.M. Thesis, Massachusetts Institute of Technology, Cambridge, Massachusetts.

Eisenhaure, D.B. [1977], G. Oberbeck, and J.R. Downer. Development of a Low-loss Flywheel Magnetic Bearing. 14th Intersociety Energy Conversion Engineering Conference Proceedings, American Chemical Society, 1: pp. 357-362.

Eisenhaure, D.B. [1984a], J.R. Downer, T. Bliamptis, and S. Hendrie. A Combined Attitude, Reference, and Energy Storage System for Satellite Applications. Presented at AIAA 22nd Aerospace Sciences Meeting, Reno, Nevada.

Eisenhaure, D.B. [1984b], J.R. Downer, R.L. Hockney, and S.R. O'Dea. Multivariable Function Utilization of Inertial Energy Storage Wheels in Spacecraft Applications. In AIAA Guidance and Control Conference Proceedings, Seattle, Washington: pp. 44-54.

Groom, N.J. [1978] and D.E. Terray. Evaluation of a Laboratory Test Model Annular Momentum Control Device. NASA TP-1142.

Groom, N.J. [1981] and J.B. Miller. A Microprocessor-Based Table Lookup Approach for Magnetic Bearing Linearization. NASA TP-1838.

Groom, N.J. [1984]. **Overview of Magnetic Bearing Control and Linearization Approaches for Annular Magnetically Suspended Devices.** An Assessment of Integrated Flywheel System Technology, Conference Proceedings, Huntsville, Alabama: pp. 297-306. NASA Conference Publication 2346.

Gunter, E.J. [1966]. **Dynamic Stability of Rotor-Bearing Systems.** NASA, Washington, D.C.

Harris, C.R. and C.E. Crede [1976]. **Shock and Vibration Handbook.** 2nd Ed. New York: McGraw Hill.

Hubbard, M. and P. McDonald [1980]. **Feedback Control Systems for Flywheel Radial Instabilities.** 1980 Flywheel Technology Symposium Proceedings, Scottsdale, Arizona: pp. 209-217.

Johnson, B.G. [1987a]. **Active Control of a Flexible, Two-Mass Rotor: The Use of Complex Notation.** Doctor of Science Thesis, Massachusetts Institute of Technology.

Johnson, B.G. [1987b]. **Advanced Actuators for the Control of Large Space Structures.** Phase I SBIR Final Report, SatCon Report R07-87.

Kaya, F. and J.B. Roberts [1984]. **Optimum Vibration Control of Flexible Transmission Shafts.** Proceedings of the Third International Conference on Vibrations in Rotating Machinery, University of York, England: pp. 525-534.

Keckler, C. and K. Jacobs [1974]. **A Spacecraft Integrated Power/Attitude Control System.** Proceedings of the Ninth Intersociety Energy Conversion Engineering Conference, San Francisco, California.

Kennel, H. [1970]. **A Control Law for Double-Gimballed Control Moment Gyros Used for Space Vehicle Attitude Control.** NASA TM-X-64536.

Kwakernaak, H. and R. Sivan [1972]. **Linear Optimal Control Systems.** New York: J. Wiley & Sons.

McDonald, P. and M. Hubbard [1985]. **An Actively Controlled Pendulous Flywheel with Magnetic Bearings.** Proceedings of the 20th Intersociety Energy Conversion Engineering Conference. Miami Beach, Florida: pp. 2.525-2.530.

Muramaki, C. [1982]. **Development Activities on Magnetic Bearings for Space Use in National Aerospace Laboratory of Japan.** Proceedings of the Sixth International Workshop on Rare Earth Cobalt Permanent Magnets, Technical University of Vienna.

Nikolajsen, J.L. [1979], R.L. Holmes, and V. Gondhalekar. Investigation of an Electromagnetic Damper for Vibration Control of a Transmission Shaft. Proceedings of the Institution of Mechanical Engineers. 193: pp. 331-336.

Notti, J.E. [1974], A. Cormack III, and W.C. Schmill. Integrated Power/Attitude Control System (IPACS) Study. NASA CR-2383.

O'Dea, S.R. [1985], P. Burdick, J.R. Downer, and D.B. Eisenhaure. Design and Development of a High Efficiency Effector for the Control of Attitude and Power in Space Systems. Proceedings of the 20th Intersociety Energy Conversion Engineering Conference, Miami Beach, Florida: pp. 2.353-2.360.

Oglevie, R.E. [1985] and D.B. Eisenhaure. Advanced Integrated Power and Attitude Control System (IPACS) Study. NASA CR-3912.

Roberson, R. [1958]. Principles of Inertial Control of Satellite Attitude. Proceedings of the 9th International Congress of Aeronautics, Amsterdam, Holland.

Robinson, A. [1984]. European Development Experience on Energy Storage Wheels for Space. An Assessment of Integrated Flywheel System Technology. NASA CP-2346: pp. 65-73.

Sabnis, A.J. [1975], J. Dendy, and F. Schmidt. A Magnetically Suspended Large Momentum Wheel. Journal of Spacecraft and Rockets, 12: pp. 420-427.

Salm, J. [1984] and G. Schweitzer. Modelling and Control of a Flexible Rotor with Magnetic Bearings. Proceedings of the Third International Conference on Vibrations in Rotating Machinery, University of York, England: p. 553.

Schweitzer, G. [1974]. Stabilization of Self-Excited Rotor Vibrations by an Active Damper. In Dynamics of Rotors, edited by F.I. Niordson, Springer-Verlag, New York.

Stanway, R. [1984] and J. O'Reilly. State-Variable Feedback Control of Rotor-Bearing Suspension Systems. Proceedings of the Third International Conference on Vibrations in Rotating Machinery, University of York, England.

Stein, G. [1987] and M. Athans. The LQG/LTR Procedure for Multivariable Feedback Control Design. IEEE Transactions on Automatic Control. Vol. 32, No. 2.

Stocking, G. [1984]. Magnetically Suspended Reaction Wheel Assembly. An Assessment of Integrated Flywheel System Technology, NASA CP-2346, pp. 265-279.

Ulbrich, H. [1984] and E. Anton. **Theory** and **Application of Magnetic Bearings with Integrated Displacement and Velocity Sensors.** Proceedings of the Third International Conference on Vibrations in Rotating Machinery, University of York, England: pp. 543-551.

Weinberg, M. [1982]. **Momentum Exchange Effectors for Space Applications.** P-1532, The Charles Stark Draper Laboratory, Inc., Cambridge, Massachusetts.

Wertz, J. [1978]. **Spacecraft Attitude Determination and Control,** R. Reidel Publishing Co.

1. Report No. NASA CR-4166	2. Government Accession No.	3. Recipient's Catalog No.
4. Title and Subtitle Synchronous Response Modelling and Control of an Annular Momentum Control Device		**5. Report Date** August 1988
		6. Performing Organization Code
7. Author(s) Richard Hockney, Bruce G. Johnson, and Kathleen Misovec		**8. Performing Organization Report No.**
		10. Work Unit No. 585-01-21-06
9. Performing Organization Name and Address SatCon Technology Corporation 71 Rogers St. Cambridge, MA 02139		**11. Contract or Grant No.** NAS1-18322
		13. Type of Report and Period Covered Contractor Report
12. Sponsoring Agency Name and Address National Aeronautics and Space Administration Langley Research Center Hampton, VA 23665-5225		**14. Sponsoring Agency Code**

15. Supplementary Notes

Langley Technical Monitor: Claude R. Keckler
Final Report

16. Abstract

This report documents research into the synchronous response modelling and control of an advanced Annular Momentum Control Device (AMCD) used to control the attitude of spacecraft.

For the flexible rotor AMCD, two sources of synchronous vibrations were identified. One source, which corresponds to the mass unbalance problem of rigid rotors suspended in conventional bearings, is caused by measurement errors of the rotor center of mass position. The other source of synchronous vibrations is misalignments between the hub and flywheel masses of the AMCD.

Four different control algorithms were examined. These were lead-lag compensators that mimic conventional bearing dynamics, tracking notch filters used in the feedback loop, tracking differential-notch filters, and model-based compensators.

The tracking differential-notch filters developed under this contract were shown to have a number of advantages over more conventional approaches for both rigid-body rotor applications and flexible rotor applications such as the AMCD. Hardware implementation schemes for the tracking differential-notch filter were investigated. A simple design was developed that can be implemented with analog multipliers and low bandwidth, digital hardware.

17. Key Words (Suggested by Author(s)) Modelling and Control Annular Momentum Control Device Magnetic Bearing		18. Distribution Statement Unclassified-Unlimited Subject Category 31	
19. Security Classif. (of this report) Unclassified	20. Security Classif. (of this page) Unclassified	21. No. of pages 152	22. Price A07